Transmon-based Quantum Processing Units: Design, Control and Implementations

Candidate: Hervè Atsè Corti
Supervisors: Prof. Alessandro Cidronali, Prof. Leonardo Banchi

31 January 2024

Contents

Chapter 1

Introduction

Despite coming from a foundation in electrical engineering, my academic journey has been consistently marked by a profound fascination with quantum mechanics. The discovery of quantum information and computation has further captivated my interest, intertwining the abstract beauty of quantum theories with practical applications. This thesis, shaped with an engineer's pragmatism, seeks to underscore the engineering side of quantum computing. My aim is to spark the curiosity among engineers, especially those in the field of radio frequency, whose skill set is crucial to the advancement of quantum computing research.

The ambition of this thesis is to forge a link between the theoretical underpinnings of physics and the tangible world of engineering practice, providing readers with guide to acquiring the expertise needed to embark on research in this vibrant field. I am proud to note that the research conducted during my PhD not only culminated in this thesis but also led to contributions in scientific literature. These include a paper on optimal qubit control [1], as well as works on superconducting hardware qubit design [2, 3].

1.1 Structure of the Thesis

This thesis is structured to provide a comprehensive exploration of today snapshot of quantum computing field, with a focus on the development and operation of Transmon Quantum Processing Units (QPUs). Each chapter is designed to build upon the previous one, gradually deepening the reader's understanding of the subject. The following is an overview of the structure and content of each chapter:

Chapter 1: Introduction - This initial chapter sets the stage for the thesis, introducing the field of quantum information science and the focus on Quantum Processing Units. It outlines the background, objectives, and the structure of the thesis, providing a clear context and motivation for the research.

Chapter 2: Theoretical Foundations of Quantum Information - Here, the fundamental concepts of quantum information theory are presented. This includes a detailed discussion on the principles and advantages of quantum computing. This chapter lays the theoretical groundwork essential for understanding the subsequent chapters on hardware and QPU design.

Chapter 3: Superconducting Quantum Hardware Building Blocks - This chapter delves into the practical aspects of quantum computing, focusing on the development and intricacies of superconducting quantum hardware building blocks. Topics covered include superconductivity, linear resonator, Josephson Junction and DC-SQUID.

Chapter 4: Quantum Processing Units Architecture and Design - Dedicated to Quantum Processing Units, this chapter explores their architecture and design principles. It includes a detailed examination of the Transmon qubit, Transmon QPU architectures and a case study on the Transmon QPU that I contribute to develop for the INFN QubIT project.

Chapter 5: Controlling the Quantum Processing Unit - This chapter addresses the crucial aspects of QPU control, covering the fundamentals of qubit control, gate implementation, and advances in optimal control techniques. It also includes a case study on the qubit control strategies that I researched during my research stays at Chalmers University of Technology.

Chapter 6: Measuring the Quantum Processing Unit - Focusing on measurement techniques, this chapter discusses the challenges and methods of qubit readout, the design principles of the Josephson Parametric Amplifier (JPA), and a case study on the JPAs that I contribute to develop in the INFN QubIT project.

Chapter 7: Conclusion - The final chapter summarizes the findings of the thesis, reflecting on the contributions made to the field of quantum computing and suggesting future research directions. This chapter also includes acknowledgements, paying tribute to those who have supported and contributed to the research.

Embarking on this journey, the thesis aspires to enhance the reader's understanding and appreciation of this dynamic field, as well as ignite their curiosity, potentially leading to future explorations and discoveries.

1.2 Background

Quantum computing, a concept that originated from the foundational works of physicists like Richard Feynman [4] and David Deutsch, has grown from a theoretical curiosity to a practical pursuit. The idea of leveraging quantum mechanical phenomena such as superposition and entanglement to perform computation has opened new horizons in the field of information technology. This journey from theory to potential real-world applications marks a significant paradigm shift in computational sciences.

The significance of quantum computing lies in its fundamental difference from classical computing. While classical computers process information in binary bits, quantum computers use quantum bits (qubits), which are mathematical objects that access a more powerful computational framework [5]. This allows quantum computers to potentially solve certain classes of problems much more efficiently than their classical counterparts. Quantum algorithms like Shor's algorithm for factoring large numbers and Grover's algorithm for database search operations are prime examples of this potential, with profound implications for fields such as cryptography, optimization, and drug discovery.

However, the path to realizing practical quantum computing is filled with challenges, many of which stem from the intricacies of the technologies involved. Through this thesis we will focus on superconducting quantum computing (SQC) [6, 7], a technology that has been widely adopted by research groups and companies investing in this sector. Superconducting quantum computing, while promising due to its relatively advanced stage of development, still faces significant hurdles that impede its scalability and practical application.

Firstly, scalability issues present a substantial challenge. SQC requires complex and sophisticated setups both at the chip level and in the experimental apparatus. As the number of qubits (more on this topic in the following chapters) on a chip increases, maintaining coherence and managing interactions among them becomes increasingly difficult. This complexity exacerbates when considering the interconnects and control electronics necessary for a larger system, often leading to a convoluted and hard to manage architecture.

Figure 1.1: This image depicts an IBM laboratory, illustrating the complexity inherent in a superconducting quantum computing experimental apparatus. *Source: IBM*

Secondly, the operational challenges associated with SQC are non-trivial. These quantum devices operate at extremely low temperatures, in the order of tens of mK, necessitating elaborate cryogenic systems called *dilution refrigerators*. Maintaining such conditions is not only energy-intensive but also poses significant technical and engineering challenges, especially as systems scale up in size. The cryogenic environment adds to the complexity and cost of quantum computing systems, making them less accessible and more challenging to deploy in various settings.

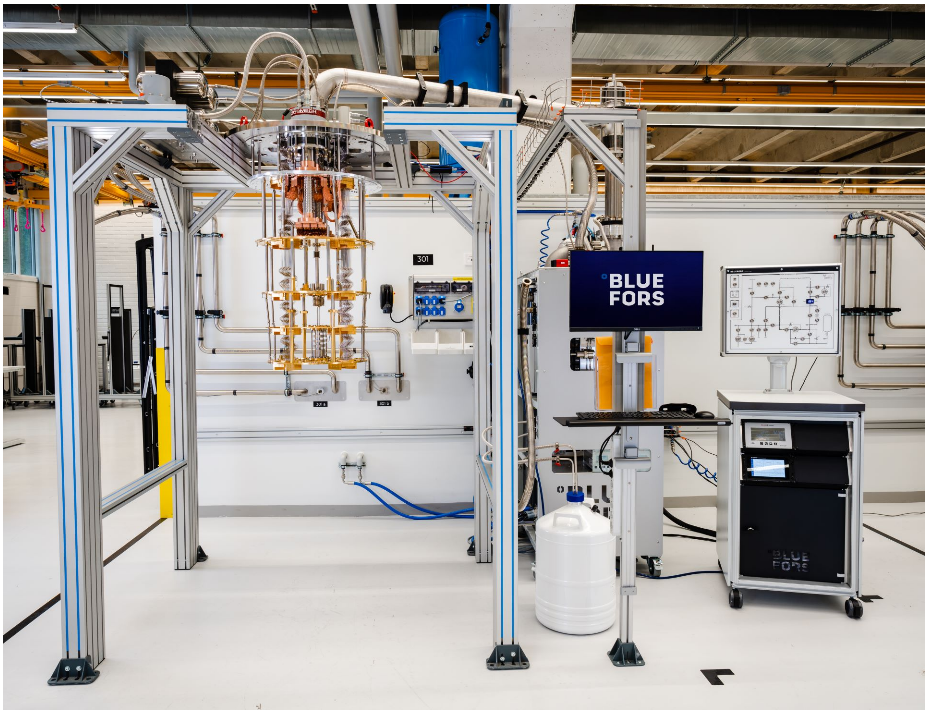

Figure 1.2: The image shows a dilution refrigerator produced by Bluefors. The depicted refrigerator is unshielded, revealing its internal structure. *Source: Bluefors.*

Furthermore, issues such as qubit decoherence, error rates, and the need for effective quantum error correction mechanisms continue to be significant obstacles. While SQC devices have shown improved coherence times [8], they are still prone to errors caused by environmental noise and quantum state leakage [9]. Developing robust error correction techniques that do not overwhelmingly increase the resource overhead is a critical area of ongoing research.

Other challenges include the crosstalk between qubits [10], especially in densely packed architectures, and the reliability of quantum gates. As systems become more complex, ensuring that quantum operations are executed accurately and consistently becomes more challenging, necessitating continual advancements in qubit design and control techniques.

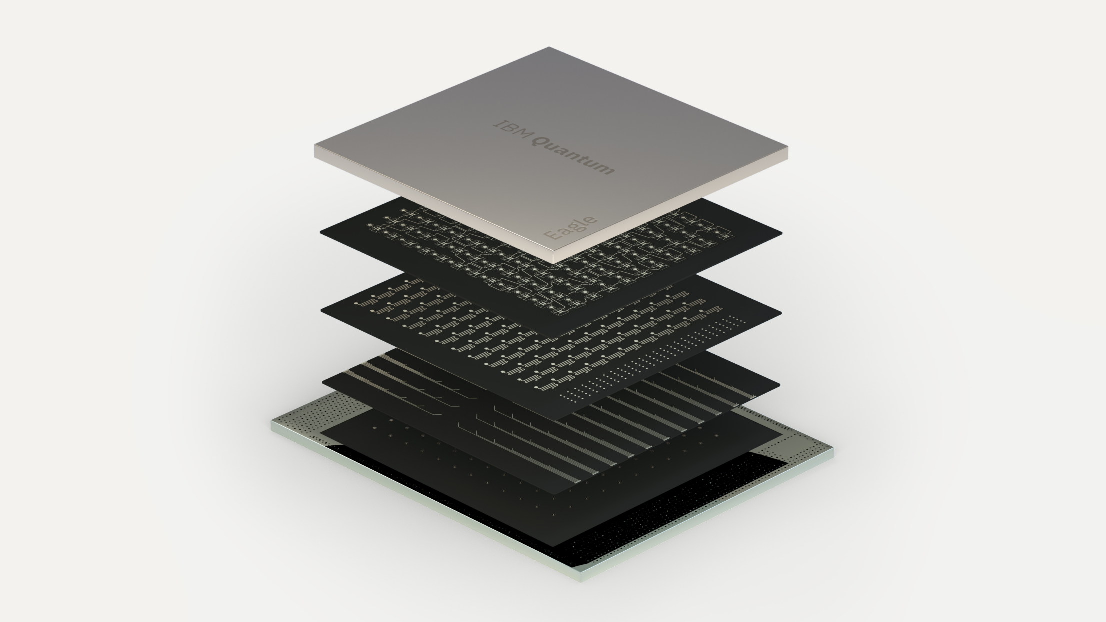

Figure 1.3: This image displays the layout of a 127-qubit chip produced by IBM. It illustrates the dense packing of the qubits and all the auxiliary structures. *Source: IBM.*

Globally, research and development in quantum computing are marked by extensive collaborations and investments, reflecting its importance as a field with far-reaching implications. Beyond technical advancements, quantum computing also presents ethical and societal considerations. Issues like data privacy in a post-quantum cryptography era and the equitable distribution of such powerful technology are increasingly relevant discussions.

This thesis guides the reader through the heart of this revolutionary field, reporting on my research during my PhD. It focuses on two main areas: the design of Transmon qubits and Josephson parametric amplifiers (JPAs) for the INFN QubIT Project, contributing to Italy's growing efforts in the global landscape of superconducting quantum technologies; and the application of optimal control theory to the Transmon-based quantum processing unit (QPU) designed at Chalmers University of Technology, demonstrating a scalable and easily implementable optimization algorithm for fast and accurate quantum gates.

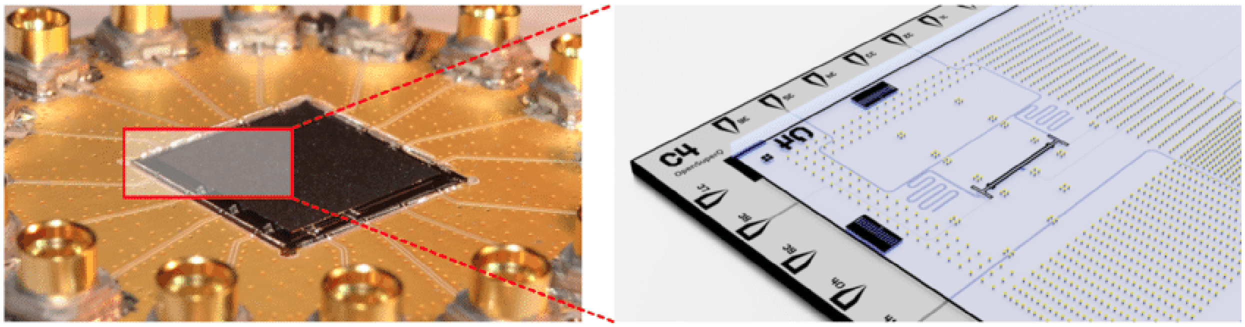

Figure 1.4: The image shows a Transmon QPU realized by the Quantum Nanoelectronics Laboratory at Chalmers University of Technology. *Source: Chalmers University of Technology.*

1.3 INFN QubIT Project

The INFN QubIT project, headed by the Istituto Nazionale di Fisica Nucleare (INFN), represents one of Italy's most significant progresses in the realms of quantum computing and fundamental physics. This project unites the efforts of the INFN sections from Ferrara, Florence, Frascati, Milan, Milan Bicocca, Pisa, Salerno, TIFPA, as well as partners like Istituto di Fotonica e Nanotecnologie (CNR-INF) and Fondazione Bruno Kessler (FBK).

QubIT intertwines the development of advanced quantum hardware, particularly superconducting devices like Transmon qubits, with the pursuit to build an itinerant-photon detector for axion experiments [11, 12]. Axions, as hypothesized particles, hold the potential to unravel mysteries surrounding dark matter, a pivotal element in our understanding of the universe. Detecting these elusive particles would not only be a landmark achievement in particle physics, but also significantly bolster our understanding of cosmological phenomena.

My involvement with the INFN QubIT project has been a cornerstone of my PhD journey. It provided the perfect opportunity to apply my research in a practical setting, significantly enriching my theoretical knowledge and practical skills in quantum hardware development. This collaboration has been mutually enriching, contributing substantially to ambitious goals of the project while profoundly enhancing my own research and insights into quantum technologies.

This synergy not only underscores the interdisciplinary nature of modern scientific research but also highlights the potential of quantum technologies to make groundbreaking contributions in both computational sciences and fundamental physics.

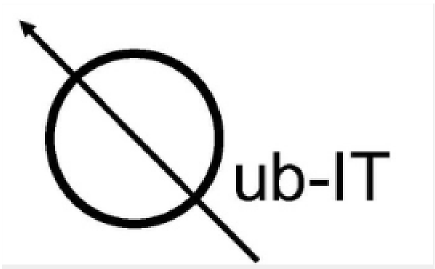

Figure 1.5: The image shows the project logo. *Source: INFN.*

Chapter 2

Theoretical Foundations of Quantum Information

Quantum information theory represents a groundbreaking shift in our understanding of information processing, computation, and the fundamental principles of quantum mechanics [5]. This chapter serves as a critical foundation for the rest of the thesis. It provides the essential theoretical background required to appreciate the complexities and potential of quantum computing and sets the stage for a deeper exploration of the technological advancements and challenges in the field of quantum hardware. The understanding gained here is not just academic; it is fundamental to appreciating the broader implications and potential applications of quantum computing in various scientific and technological domains.

2.1 Quantum Mechanics Axioms

The theory of quantum mechanics admits numerous equivalent formulations. In this text, we will report on the *axiomatic formulation based on the Copenhagen interpretation*, universally recognized and considered a standard. The axioms illustrated below are confirmed by the fact that experimental physics is able to verify many of the predictions of quantum mechanics with extraordinary accuracy. Throughout this text, *Dirac notation* will be adopted, which uses the symbolism $|\psi\rangle$ to indicate vectors belonging to Hilbert spaces and $\langle\psi|$ to indicate their complex conjugate transposes. The following are the axioms of quantum mechanics.

1. Pure State *To every physical system S, a Hilbert space H_s is associated. Each vector $|\psi\rangle \in H_s$, with $\langle\psi|\psi\rangle = 1$, represents a pure physical state of the system S.*

A pure state is understood as a perfectly determined state of the system. The state of a closed system is always pure, but a pure state does not necessarily correspond to a closed system. It is important to clarify that in the discussion of the topics addressed in this thesis, physical systems are always associated with finite-dimensional Hilbert spaces.

1.1 Mixed State *To every physical system S in a mixed state is associated a linear operator $\hat{\rho}$ called the density operator, acting in H_s and representing the physical state of the system,* *such that:*

- $\hat{\rho}$ *is Hermitian*
- $\hat{\rho}$ *is positively defined*
- $\hat{\rho}$ *has a unitary trace*

Consider $\{|\psi_i\rangle, p_i\}$ as a set of pure states belonging to H_s and p_i as the classical probability that the system is found in the state $|\psi_i\rangle$. If $p_i \neq 1$, the system is in a mixed state. The operator $\hat{\rho}$ is such that:

$$\hat{\rho} = \sum_i p_i |\psi_i\rangle \langle\psi_i| , \quad \sum_i p_i = 1 \ . \tag{2.1}$$

In cases where the probability of finding the system in state i is $p_i = 1$, and thus the state of the system is pure (completely determined), the density operator $\hat{\rho}$ is defined as:

$$\hat{\rho} = |\psi_i\rangle \langle\psi_i| \ . \tag{2.2}$$

In this context, the treatment of quantum physics using density operators is equivalent to the treatment using the state vector $|\psi_i\rangle$. An *operator* here is understood as a map acting on a vector belonging to the Hilbert space associated with the system to produce another element within it. An operator is considered *Hermitian* if it satisfies the following condition:

$$\hat{O} = \hat{O}^\dagger \ . \tag{2.3}$$

Where $\hat{O}^\dagger$ is the complex conjugate transpose of $\hat{O}$.

Positively defined operators are those for which, given $\hat{A}$ as a generic positively defined operator:

$$\langle\psi| \hat{A} |\psi\rangle = C, \quad C \in \mathbb{R}_0^+, \quad \forall |\psi\rangle \in H_s \ . \tag{2.4}$$

The *trace* applied to a generic operator $\hat{A}$ performs the following operation:

$$Tr(\hat{A}) = \sum_i \langle i_A| \hat{A} |i_A\rangle = \sum_i \hat{A}_{ii} \ . \tag{2.5}$$

This operation corresponds to the sum of all elements on the diagonal of $\hat{A}$. The set of vectors $|i_A\rangle$ represents any basis for the Hilbert space H_s associated with the system, with the trace having the property of being invariant with respect to the chosen basis. The condition that imposes $\hat{\rho}$ to have a unitary trace therefore requires that:

$$Tr(\hat{\rho}) = \sum_i \langle i| \hat{\rho} |i\rangle = \sum_i \hat{\rho}_{ii} = 1 \ . \tag{2.6}$$

The elements $|i\rangle$ represent a generic basis, that is, a set of vectors $|i\rangle \in H_s$ such that $\sum_i |i\rangle \langle i| = \hat{I}$ (where $\hat{I}$ is the identity operator). For simplicity, throughout this chapter, we will consider this basis coincident with the eigenstates basis of the density operator so that it can be considered diagonal.

It is crucial to note the distinction made between pure and mixed states. The introduction of mixed states is essential for addressing open quantum systems, which are subject to information exchange with the external environment.

2. Evolution of Quantum States *In quantum mechanics, the evolution of pure states is a fundamental concept, described by unitary transformations denoted as $\hat{U}(t)$. These transformations encapsulate the dynamic progression of quantum states over time. For a pure quantum state initially described by $|\psi(0)\rangle$, its evolution at a later time t is represented as:*

$$|\psi(t)\rangle = \hat{U}(t) |\psi(0)\rangle \quad . \tag{2.7}$$

This equation signifies that the state at time t, $|\psi(t)\rangle$, is obtained by applying the unitary operator $\hat{U}(t)$ to the initial state $|\psi(0)\rangle$. The unitary nature of $\hat{U}(t)$ ensures that the quantum state's evolution is reversible and preserves the probabilities inherent in the state.

Conversely, in the case of mixed states, which are described by the formalism of density operators, the evolution follows a different yet related pattern. A mixed state at an initial time is represented by a density operator $\hat{\rho}(0)$. As time progresses, the evolution of this mixed state is governed by both the unitary operator $\hat{U}(t)$ and its complex conjugate transpose $\hat{U}^\dagger(t)$, leading to the expression:

$$\hat{\rho(t)} = \hat{U}(t)\hat{\rho}(0)\hat{U}^\dagger(t) \quad . \tag{2.8}$$

This form of the evolution equation reflects how the mixed state, a statistical ensemble of pure states, evolves under the influence of $\hat{U}(t)$. The transformation encapsulates the combined effects of unitary evolution on each constituent pure state within the ensemble. In essence, this approach to describing the evolution of mixed states through density operators provides a comprehensive view of how quantum systems evolve, taking into account the probabilistic and statistical nature inherent in quantum mechanics.

3. Measurement of Quantum States *Measurement in quantum mechanics is a pivotal process that directly relates to the observables of a quantum system. Each dynamic variable related to the system S is associated with a linear and Hermitian operator $\hat{O}$, acting in the Hilbert space H_s. The eigenvalues of this operator represent the possible measurable values of the corresponding dynamic variable, defining $\hat{O}$ as an observable.*

In the context of state vector formalism, the expectation value, or mean value, of a generic observable $\hat{O}$ for a quantum system in state $|\psi\rangle$ is given by the relationship:

$$\langle \hat{O} \rangle = \langle \psi | \hat{O} | \psi \rangle \quad . \tag{2.9}$$

This equation calculates the average value of the measurements of $\hat{O}$, considering all possible outcomes weighted by their respective probabilities. It is a cornerstone in understanding quantum phenomena and provides insight into the probabilistic nature of quantum measurements.

When applied in a context where the density operator formalism is used, the expectation value of $\hat{O}$ adapts to incorporate the statistical properties of mixed states. This adaptation is reflected in the modified expression:

$$\langle \hat{O} \rangle = Tr(\hat{\rho}\hat{O}) \ . \tag{2.10}$$

Here, the trace operation, denoted as Tr, is applied to the product of the density operator $\hat{\rho}$ and the observable $\hat{O}$. This formula calculates the mean value by accounting for the probabilities of all the pure states constituting the mixed state.

The act of measuring an observable associated with the system induces a profound change: the collapse of its state vector, often a superposition of multiple eigenstates of the observable, into a single eigenstate. This collapse is an irreversible process, leading to a loss of information about the pre-measurement state of the system. The irreversible nature of measurement in quantum mechanics highlights the fundamental difference between quantum and classical systems; measuring a quantum system invariably alters its state due to the necessity of interaction between the measurer and the measured system to acquire information.

4. Composite Quantum Systems *For an isolated physical system S, viewed as a composition of multiple physical subsystems S_i, each associated with a Hilbert space H_i where $i \in [1, .., n]$, the corresponding Hilbert space H_s is defined by:*

$$H_s = H_1 \otimes \ldots \otimes H_n \ . \tag{2.11}$$

Here, the symbol $\otimes$ represents the operation of tensor product. A pure state of the overall system is defined as non-entangled if it can be expressed as:

$$|\phi\rangle = |\phi_1\rangle \otimes \ldots \otimes |\phi_n\rangle \,, \quad |\phi\rangle \in H_s \wedge |\phi_i\rangle \in H_i \ . \tag{2.12}$$

If this mathematical representation is not permissible, the system is in an entangled state. An example of a well-known entangled state is:

$$|\psi\rangle = \frac{1}{\sqrt{2}}(|0\rangle \otimes |0\rangle + |1\rangle \otimes |1\rangle) \ . \tag{2.13}$$

Conversely, an example of a non-entangled state is given by:

$$\begin{aligned} |\psi\rangle &= \frac{1}{2}(|0\rangle \otimes |0\rangle + |0\rangle \otimes |1\rangle + |1\rangle \otimes |0\rangle + |1\rangle \otimes |1\rangle) \\ &= \frac{|0\rangle + |1\rangle}{\sqrt{2}} \otimes \frac{|0\rangle + |1\rangle}{\sqrt{2}} \ . \end{aligned} \tag{2.14}$$

In cases where the overall system is in a non-entangled state, the state is considered separable, meaning it can be described through the tensor product of the states of the subsystems.

For notational convenience in this text, the tensor product symbol ⊗ is often omitted, with the following equivalence assumed:

$$|\psi\rangle \otimes |\phi\rangle = |\psi\phi\rangle \quad . \tag{2.15}$$

2.2 Qubit, The Unit of Quantum Information

At the heart of quantum information science lies the *qubit*, or quantum bit, the fundamental unit of quantum information. This section explores its conceptual framework, unique properties, and its pivotal role in quantum computing and information processing.

The qubit, unlike its classical counterpart, the bit, embodies the principles of quantum theory. While a classical bit exists in a definite state, either 0 or 1, a qubit can exist in a superposition of both states simultaneously. This corresponds to a quantum system being in multiple states at once, a phenomenon that defies classical intuition and provides the substrate for the enhanced capabilities of quantum computing.

To delve deeper into the nature of qubits, this section examines key quantum mechanical properties such as superposition and entanglement. Superposition allows a qubit to hold a combination of states. Entanglement, another quintessential quantum property, occurs when qubits become interconnected in such a way that the state of one qubit is dependent on the state of another, regardless of the distance separating them. This property is not just of theoretical interest; it is a critical resource for quantum computing, enabling complex computations that are infeasible for classical computers.

Nevertheless, harnessing the quantum realm presents significant challenges, primarily due to the difficulty in creating hardware qubits capable of maintaining a quantum state. These devices are perpetually at risk of unwanted interactions with their environment, leading to an inherent limitation in their coherence. Coherence refers to the time during which a qubit maintains its quantum state, and decoherence is the process by which qubits lose their quantum properties, often due to interactions with their external environment. Understanding and controlling decoherence is crucial for the practical realization of quantum computing, as it directly impacts the reliability and scalability of quantum processors.

Mathematically, a qubit is a vector on a two-dimensional Hilbert space representing the state of a quantum system. As a basis for the vector space, two eigenstates (i.e., eigenvectors) related to an observable associated with a dynamic variable of the system, such as energy, are used. The most common eigenbasis used in quantum information is the *computational basis*. This basis employs the eigenstates $|0\rangle$ and $|1\rangle$ to represent the logical states 0 and 1, respectively, in relation to classical information theory. The state of the qubit, being a vector belonging to the Hilbert space associated with the system, is described through the linear combination of the eigenstates of the basis, thanks to the principle of superposition of states:

$$|\psi\rangle = \alpha\,|0\rangle + \beta\,|1\rangle \quad . \tag{2.16}$$

The coefficients α and β are such that $\alpha, \beta \in \mathbb{C}$ and are subject to normalization, that is:

$$|\alpha|^2 + |\beta|^2 = 1 \ . \tag{2.17}$$

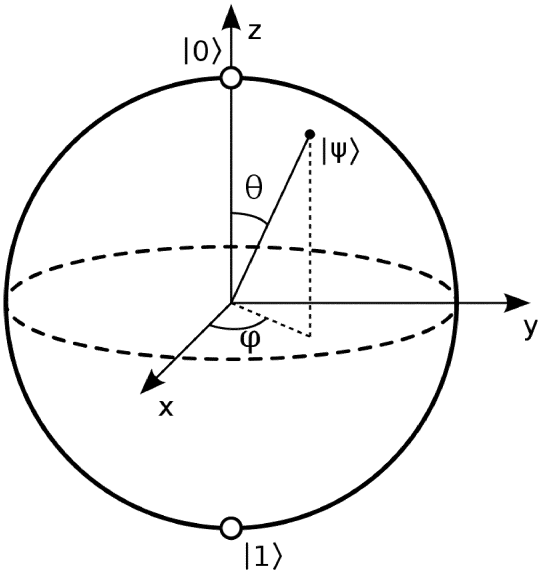

Figure 2.1: Representation of a qubit state using the Majorana-Bloch sphere. The probability amplitudes of the qubit's eigenstates superposition, $|\psi\rangle = \alpha\,|0\rangle + \beta\,|1\rangle$, are given by $\alpha = \cos\left(\frac{\theta}{2}\right)$ and $\beta = e^{i\phi}\sin\left(\frac{\theta}{2}\right)$.

Unlike bit, whose possible configuration includes only the two states $|0\rangle$ or $|1\rangle$, the qubit is capable of assuming an infinite number of states (see Figure 2.1). However, accurately capturing the state of a qubit is far from trivial. To reconstruct the pre-measurement state of the system, a statistical approach is typically employed, choosing observables that allow for *projective measurements*, i.e., such that the system collapses into one of the eigenstates relative to the basis after the measurement act.

In the case of the qubit, given the adoption of the computational basis, the act of projective measurement leads to collapse into one of the two eigenstates, $|0\rangle$ or $|1\rangle$. Since the measurement of quantum systems is destructive, once performed, it is impossible to apply transformations to the system to recover the pre-measurement state (the measurement is an irreversible operator unlike the system's time evolution).

Therefore, it is necessary to prepare multiple virtually identical states to perform the number of measurements required to statistically derive the pre-measurement state of the qubit (or more precisely the state in which the identically prepared qubits are found) with sufficient confidence. Obviously, the accuracy of the statistical approach is not infinite and makes it impossible to discriminate all the infinite possible states the qubit can assume, not to mention the further limits imposed by operational conditions. Furthermore, as we will see in the next chapter, errors in the system state can arise from escape to non-computational but physically permissible energy levels, making it difficult to associate it with a Hilbert space of actual two dimensions.

2.3 Closed Quantum Systems

As we have seen earlier, considering a qubit in a pure state, its evolution over time is defined by the following equation:

$$|\psi(t)\rangle = \hat{U}\,|\psi(0)\rangle \quad . \tag{2.18}$$

The famous *Schrödinger equation* links the generic linear transformation acting on a system with its *Hamiltonian*, the observable related to the system's energy:

$$i\hbar\frac{\partial\,|\psi(t)\rangle}{\partial t} = \hat{H}\,|\psi(0)\rangle \quad , \tag{2.19}$$

The solution to this differential equation is obtained through states such that:

$$|\psi(t)\rangle = e^{\frac{-i}{\hbar}\hat{H}t}\,|\psi(0)\rangle \quad . \tag{2.20}$$

By appropriately acting on the system's Hamiltonian, it is possible to transform the state of the system. Quantum computing exploits experimental realizations whose Hamiltonians are time-dependent through control parameters and that allow the implementation of one of the possible sets of quantum gates capable of enabling universal computation. This topic will be explored in greater detail in the following chapters.

Given the necessity for classical control, i.e., manageable through standard electronics, experimental realizations of qubits are chosen whose Hamiltonians allow good integration with traditional electronic technologies. For instance, qubits realized in Transmon technology exploit superconducting materials deposited on semiconductor-based substrates and are controllable through appropriate electromagnetic pulses and integrable with classical electronics. This promising technology will be extensively discussed in subsequent chapters.

2.4 Open Quantum Systems

Open quantum systems refer to those where interaction with the external environment is present. Accounting for the interactions of the system of interest with the external environment, in the analysis of experimental systems, allows for a theoretical approach much closer to real operational conditions. The process of exchanging information between the quantum system and the external environment for computational purposes poses a substantial challenge. This exchange is often a source of computational errors and adds complexity to system management. It is crucial to design a system that allows for controlled manipulation. However, simultaneously, it is essential to ensure that these control channels do not inadvertently introduce unwanted interactions from the environment, which can compromise the system's integrity.

The state of an open quantum system, which may not be perfectly determined, uses the formalism of density operators for description and can be written as:

$$\rho = \sum_i p_i \left|\psi_i\right\rangle \left\langle\psi_i\right| \quad . \tag{2.21}$$

It is important to note that the notation used previously imposes the use of a diagonal basis of eigenstates for the density operator. Mathematically, it is demonstrable that, given the properties of such an operator, it is always possible to derive a diagonal basis of eigenstates for it. When a preferential basis is adopted, such as the computational basis, the density operator is generically described by:

$$\rho = \sum_{i,j} \rho_{ij} \left|\psi_i\right\rangle \left\langle\psi_j\right| , \quad \rho_{ij} = \left\langle\psi_i\right| \rho \left|\psi_j\right\rangle \quad . \tag{2.22}$$

In this case, the matrix representation of the density operator may contain off-diagonal elements $\rho_{ij}, i \neq j$, encoding information about the *coherence of the system.* In the case where the system is in a pure state, we have absolute certainty, i.e., $p_i = 1$ of finding the system in the i-th state. Consequently, the probability of the system being in other states is zero, or:

$$\rho = \left|\psi_i\right\rangle \left\langle\psi_i\right| , \quad p_{i=j} = 1 \wedge p_{i \neq j} = 0 \quad . \tag{2.23}$$

This ideal operational condition is the goal towards which experimental realizations strive, however, it is impossible to completely exclude interaction with the external environment. From a computational perspective, to mitigate this problem, efforts are made to maximize the probability that the system is in the desired i-th state, along with the use of algorithms for error correction. Since it is not possible to completely exclude the external environment, it is more accurate to treat the total system $T = (S, E)$, which includes the computational subsystem S and the external environment E. With this approach, we return to a treatment that analyzes isolated systems and thus described through pure states:

$$\rho^T = \left|\psi^T\right\rangle \left\langle\psi^T\right| \quad . \tag{2.24}$$

As seen previously, the evolution of a pure state is described by the following equation:

$$\left|\psi^T(t)\right\rangle = e^{-\frac{i}{\hbar}\hat{H}t} \left|\psi^T(0)\right\rangle \quad . \tag{2.25}$$

Constructing the density operator of a pure state through the outer product of the state vector with itself, we find that the density operator's evolution over time is described by:

$$\rho^T(t) = e^{-\frac{i}{\hbar}\hat{H}t} \left|\psi^T(0)\right\rangle \left\langle\psi^T(0)\right| e^{\frac{i}{\hbar}\hat{H}t} \quad . \tag{2.26}$$

However, for computational purposes, it is interesting to consider the evolution of the computational subsystem. For this purpose, a mathematical tool called *partial trace* applied to the external environment is used, such that:

$$\rho = Tr^E(\rho^T) \ . \tag{2.27}$$

The partial trace operator applied to the external environment acts as follows:

$$Tr^E(\rho^T) = \sum_i \left\langle i^E \right| \rho^T \left| i^E \right\rangle \ . \tag{2.28}$$

It is possible to demonstrate that any basis of vectors $\left| i^E \right\rangle$ adopted for the description of the state of the external environment provides the same result and is therefore equivalent. Considering the case where the external environment and computational system are separable, the density operator related to the overall environment is defined as:

$$\rho^T = \rho \otimes \rho^E \ . \tag{2.29}$$

In this case, the partial trace operator perfectly retrieves the state of the computational subsystem alone without losing information on the link between the two subsets. However, it is necessary to consider that the total system is not necessarily in a separable state and therefore representable through the tensor product of density operators related to the subsystems that compose it. In the case where the two subsystems are in an entangled state (i.e., not separable), applying the partial trace to the environment on the total system leads to a loss of information regarding the relative phases between the states of the two subsystems.

2.5 DiVincenzo Criteria

The *Di Vincenzo Criteria*, proposed by physicist David P. Di Vincenzo in 2000 [13], play a fundamental role in the development of quantum computing by providing the necessary conditions for its experimental realization.

These criteria can conceptually be divided into two categories: *criteria inherent to quantum computation* and *criteria inherent to quantum communication.* For the purpose of this thesis, we will specifically analyze the criteria related to quantum computation:

1. Quantum Computing Criterion *It is necessary to create a scalable experimental system with well-defined qubits.*

As previously illustrated in the section on qubits, the realization of experimental systems for this purpose requires the ability to associate (ideally) a two-dimensional Hilbert space with the state of one of their dynamic variables. Over time, various experimental realizations have been proposed, but to date, it remains a challenge to design systems capable of implementing an arbitrary number of well-characterized qubits.

2. Quantum Computing Criterion *It must be possible to initialize qubits in a known and convenient state.*

The ability to initialize qubits in a known and convenient state is necessary since the state of the qubits is not measurable until the operations applied to them are completed. Measuring during intermediate stages of computation would lead to the collapse of their state vector (i.e., the wave function), invalidating the computation. It is impossible to account for potential errors during computation, so it is fundamental to be able to initialize the system in a trustworthy, known, and convenient state to proceed with potential computation algorithms.

3. Quantum Computing Criterion *The qubits must have long decoherence times.*

The main difficulty in the experimental realizations of quantum systems is due to the impossibility of preventing them from interacting with the external environment. One of the problems introduced by this interaction is decoherence. It is necessary to design systems with decoherence times much longer than the average time required to apply quantum logical gates so that multiple sequential operations can be performed on the system and error correction algorithms can be correctly applied. Typically, systems that can be controlled quickly are more prone to decoherence caused by the same type of interaction used for control. Thus, there is a compromise between the type of control applied to the system and the increase in decoherence.

4. Quantum Computing Criterion *It must be possible to define a set of logical gates capable of realizing universal computation.*

Referring back to what was discussed previously in the paragraph on quantum logical gates, defining this type of set allows for the attainment of any system state with arbitrary precision, thus achieving universal computation. A quantum system, designed for computation and that meets the previously mentioned criteria, must be able to allow control of its Hamiltonian to implement all the logical gates belonging to at least one of the sets that enable universal computation.

5. Quantum Computing Criterion *The state of the qubits must be measurable.*

The final state of the quantum system must be measurable to draw conclusions from the execution of algorithms. Since measuring techniques are often subject to significant tolerances in results, redundancy is used in computing systems to increase the correctness of measurements by aggregating data obtained from multiple measurements. Of course, the choice of quantum computing system is also influenced by the ease of making reliable measurements on it. If the considered system allows for projective-type measurements, these can also be used to initialize qubits by causing them to collapse into a known pure state.

For completeness, the criteria related to quantum communication are also reported below, although they will not be covered in the rest of the thesis:

1. Quantum Communication Criterion *It must be possible to convert stationary qubits to flying qubits and vice versa.*

Stationary qubits refer to qubits contained within quantum computers, and flying qubits to qubits used for transporting information through transmission media. This criterion is essential for creating distributed quantum computing systems and exploiting the inherently secure communication offered by this type of technology.

2. Quantum Communication Criterion *It must be possible to transmit qubits from one station to another reliably.*

Regardless of the operational conditions of the transmission system, the protocol used, and the type of qubits adopted for this purpose, reliable qubit transmission must be guaranteed.

Chapter 3

Superconducting Quantum Hardware Building Blocks

The journey of quantum computing from a theoretical concept to a technological reality hinges critically on the development of quantum hardware. This chapter delves into the base building blocks used to design superconducting quantum devices, aiming to provide a thorough understanding of the various components, materials, and technologies that underpin this technology.

Though other various promising technologies exist for implementing qubits, such as, trapped ion qubits, and photonic qubits, each offering distinct properties, advantages, and challenges, this discussion will be centered on quantum hardware based on superconducting qubits [14].

The discussion progresses to an in-depth analysis of the design and functioning of key components, including linear resonators, Josephson junctions and DC-SQUID. Such components are essential for the qubit implementation and its connection with control electronics, which in turn enables the control and readout functions within quantum systems.

3.1 Superconductivity Introduction and Fundamental Concepts

Superconductivity, a phenomenon where certain materials exhibit zero electrical resistance and the expulsion of magnetic fields, plays a pivotal role in the realm of quantum hardware. This phenomenon is observable in superconductors when the material's temperature is below a certain critical temperature, characteristic of the material, and the energy of the interacting external magnetic fields is below a critical value. Superconducting materials include metals like aluminum and cadmium, but there are also non-metallic superconductors.

This section explores the foundational principles of superconductivity and its critical application in the development and functioning of quantum hardware.

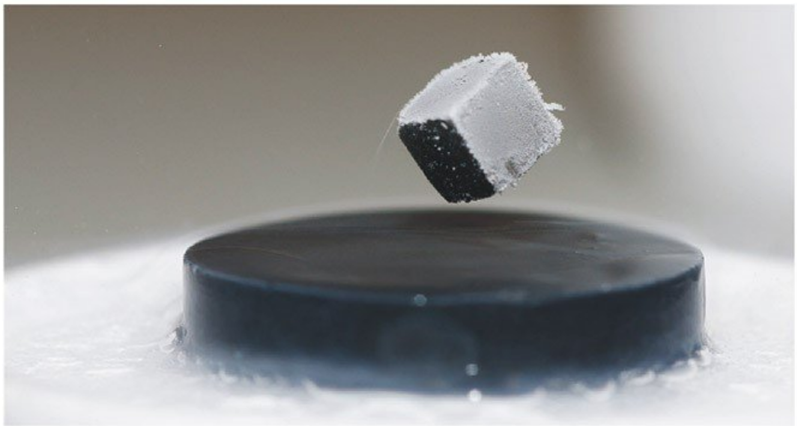

Figure 3.1: A magnetic material cube levitating above a superconductor. The magnetic field from the cube induces currents within the superconductor, creating a field that is equal and opposite, thereby perfectly counterbalancing the gravitational force exerted on the cube. *Source: Oak Ridge National Laboratory.*

Superconductivity is facilitated by particular charge carriers composed of phonon paired electrons in a single bosonic particle, called Cooper pairs or BCS pairs, in honor of physicists John Bardeen, Leon Cooper, and John Robert Schrieffer, who promoted the theory of superconductivity [15]. In 1956, analyzing the structure of conventional superconductors, American physicist Leon Cooper theorized the existence of a virtual attraction between electrons mediated by the exchange of phonons with the crystal lattice, as schematically shown in Figure 3.2.

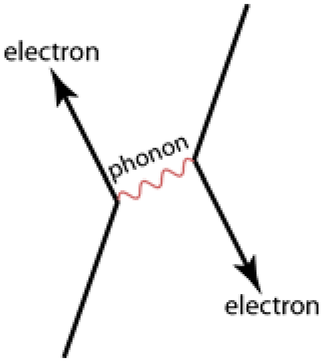

Figure 3.2: Representation of a Cooper pair, that is, two electrons coupled by a phonon.

This effect can also be interpreted classically, considering that the valence electrons in metals are easily delocalizable in a lattice of positive ions. The attraction between an electron and a positive ion, as schematically shown in Figure 3.3, causes small local distortions of the lattice, leading to a slight increase in positive charge that tends to attract other electrons.

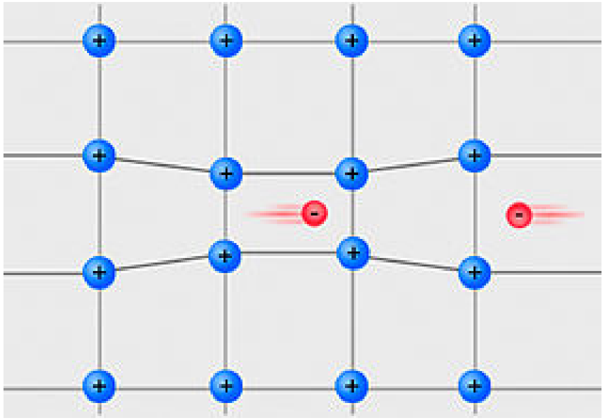

Figure 3.3: Classical representation of the local charge density variation in the crystalline lattice of the superconductor material, caused by the interaction of an electron with an ion.

As ions move much slower than electrons, once displaced from their original position, they maintain the new position for some time, even when the carrier that caused the shift has moved away, maintaining for a brief period a small variation in local charge density. Reducing the material's temperature decreases thermal agitation and increases the persistence of ions in their displaced state, thereby facilitating the attraction of other electrons. Although the attractive force caused by this mechanism is relatively weak, in cases where it can overcome the electron-electron repulsion, the two particles couple to form a Cooper pair.

Cooper pairs possess lower energy than the Fermi Energy, the energy of the highest occupied level in a system of fermions at absolute zero temperature, and hence have lower energy than free electrons. Being bound by a very weak interaction, on the order of 10^{-3} eV, they are observable (excluding conditions on external magnetic fields) only at very low temperatures, in materials able to exhibit a significant number of them, and for electron pairs that are within a maximum distance called the coherence length, characteristic of each superconductor.

Electrons composing Cooper pairs do not lose energy by interacting with the crystalline lattice, exchanging energy and momentum through it. Therefore, Cooper pairs are at an energy level that prevents energy dissipation due to lattice collisions, a concept schematized in Figure 3.4.

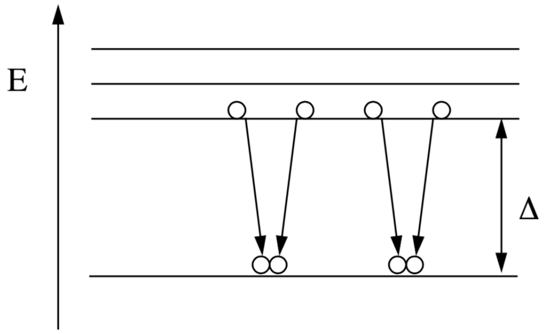

Figure 3.4: The image conceptually represents the energy gap between Cooper pairs and the energy levels of the crystalline lattice where standard electrons are found.

The energy gap Δ separating the energy of standard electrons and Cooper pairs corresponds to the energy required to separate the electrons composing them. This energy can be provided through an external magnetic field, which reaches the critical value as soon as its energy equals Δ. This explains the experimental evidence of a critical magnetic energy beyond which it is not possible to maintain the superconductive state of materials interacting with a given magnetic field. Like the critical temperature, each superconductor material has its critical energy value.

Spatially, since the interaction responsible for creating Cooper pairs can act at long distances, often the paired electrons are found at distances greater than the average electron distance in the material. Referring to Figure 3.5, this allows multiple Cooper pairs to occupy the same space.

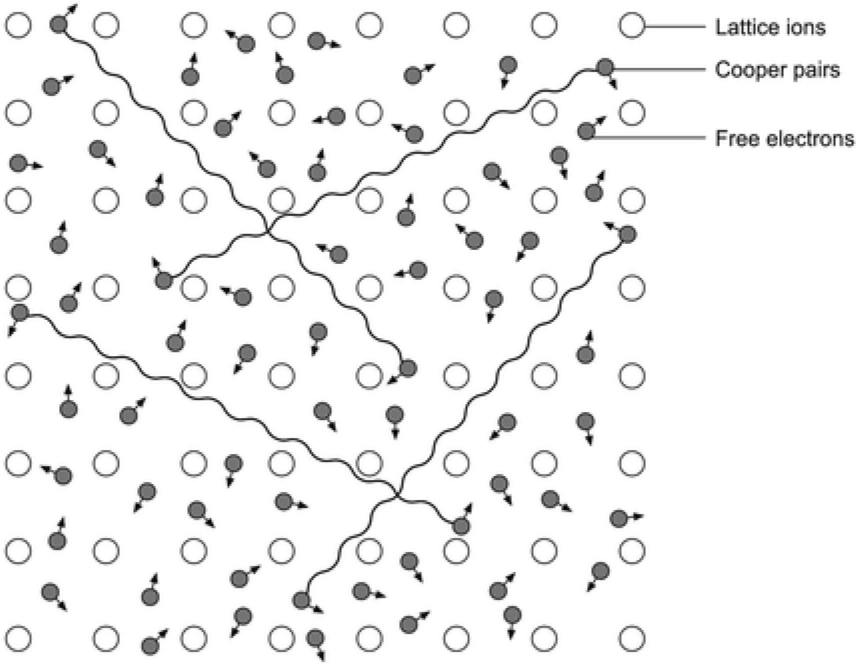

Figure 3.5: The image visually (and classically) represents the spatial overlap of multiple Cooper pairs.

Since electrons have a spin of $\frac{1}{2}$, the total spin of a Cooper pair is either 0 or 1. Consequently, it can be configured as a composite boson, and thus its statistics reflect those of bosonic particles (rather than fermionic as individual electrons). Being bosons described by a state vector symmetric with respect to the exchange of particles (in this case, Cooper pairs), multiple Cooper pairs can be in the same quantum state. This phenomenon is responsible for superconductivity.

In conclusion, superconducting materials, owing to their dissipation-less nature, play a pivotal role in facilitating efficient, and coherent quantum systems. Particularly noteworthy is their ability to maintain relatively extended coherence times, which is essential for preserving quantum states over significant durations.

3.2 Linear Resonator

At its core, a linear resonator is a device that supports standing electromagnetic waves at certain resonant frequencies. In quantum circuits, these resonators are typically realized as microwave cavities or transmission line resonators (usually Coplanar Wave Guides) [16]. The design of a linear resonator involves careful consideration of its geometrical structure and material properties to achieve specific resonant frequencies and quality factors.

In quantum circuits, linear resonators serve multiple essential functions [7, 6]. One of the primary roles is to act as a quantum bus, facilitating coherent interaction between qubits. By coupling multiple qubits to a common resonator, it is possible to mediate entanglement and implement two-qubit gates, fundamental operations in quantum computing. This coupling is achieved through the resonator's electromagnetic field, which can simultaneously interact with the qubits attached to it, allowing for controlled energy exchange.

Another critical function of linear resonators in quantum circuits is their application in qubit readout. Readout techniques can generally be categorized into two types: low-power [7] and high-power methods [17]. Currently, the most prevalent readout strategy is the low-power method that employs the dispersive shift of the resonator's resonant frequency when coupled with a qubit. The resonator is probed at low power to deduce the qubit state based on changes in its frequency. This technique will be discussed in greater detail in Chapter 6.

Furthermore, linear resonators contribute to the scalability of quantum computing architectures. Their relatively simple design and compatibility with standard fabrication techniques make them suitable for integration into complex quantum circuits with multiple qubits and resonators. This scalability is a crucial factor in advancing towards more powerful quantum computing systems capable of handling complex computational tasks.

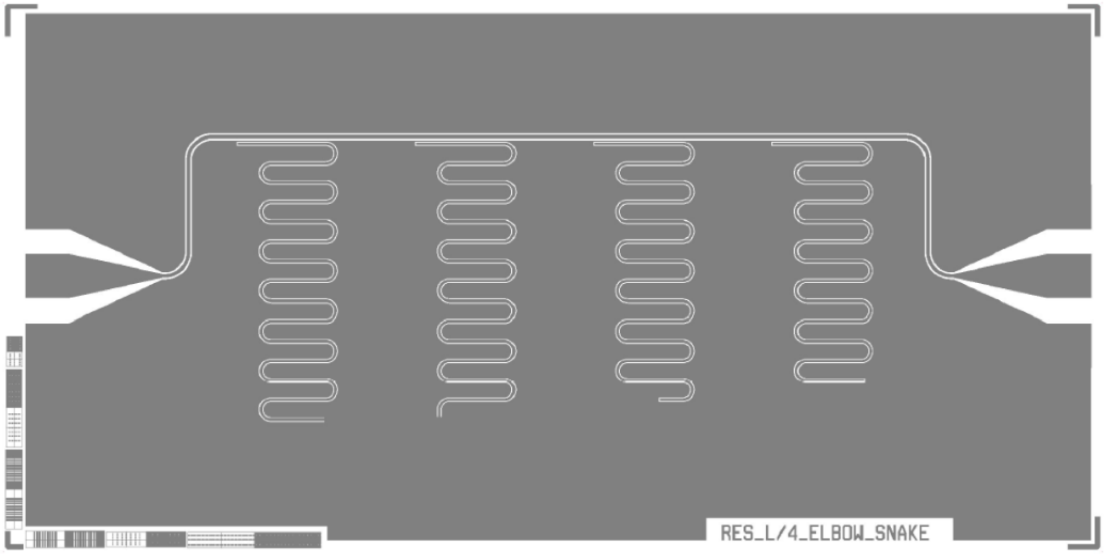

Figure 3.6: Quarter-wave resonator designed as test device for QubIT.

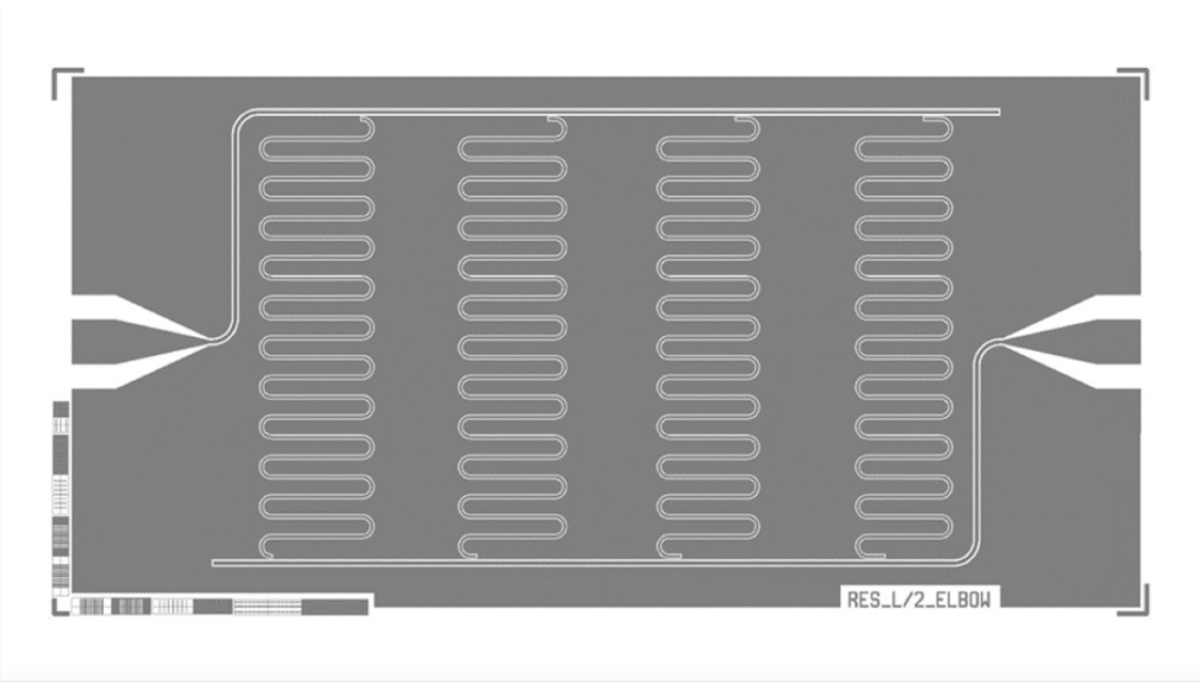

Figure 3.7: Half-wave resonator designed as test device for QubIT.

The design and optimization of linear resonators also involve addressing challenges such as minimizing loss and decoherence. Material imperfections, radiation loss, and dielectric loss are among the factors that can lead to unwanted energy dissipation in resonators, affecting their performance. Ongoing research in materials science and engineering seeks to mitigate these losses, enhancing the efficiency and coherence of quantum circuits.

To grasp the behavior of superconducting linear resonator, we begin with a classical linear LC resonant circuit. Here, energy perpetually transitions between the capacitor's electrical form and the inductor's magnetic form. For analysis, we equate the capacitor's electrical energy with an oscillator's kinetic energy, and the inductor's magnetic energy with an oscillator's potential energy. The energy present at any given moment within each component of the circuit is determined by its respective current and voltage values at that specific point in time:

$$E(t) = \int_{-\infty}^{t} V(t')I(t')dt' \ . \tag{3.1}$$

In this context, $V(t')$ and $I(t')$ represent the voltage across and current through either the capacitor or inductor, respectively. To formulate the classical Hamiltonian, we employ the classical mechanics approach of Lagrange-Hamilton formalism, expressing circuit components through generalized coordinates, either charge or flux. We opt for flux, which is the integral of voltage over time:

$$\Phi(t) = \int_{-\infty}^{t} V(t')dt' \ . \tag{3.2}$$

Analyzing the Equations 3.1 and 3.2, and considering the relationships $V = L\frac{dI}{dt}$ and $I = C\frac{dV}{dt}$, along with the application of the integration by parts technique, allows us to express the energy contributions of the capacitor and inductor directly through the nodal flux:

$$T_C = \frac{1}{2}C\dot{\Phi}^2 \ , \tag{3.3}$$

$$U_L = \frac{1}{2L}\Phi^2 \ . \tag{3.4}$$

The Lagrangian of the system is formulated by taking the difference between the kinetic and potential energies from the capacitor and inductor, respectively:

$$\mathcal{L} = T_C - U_L = \frac{1}{2}C\dot{\Phi}^2 - \frac{1}{2L}\Phi^2 \ . \tag{3.5}$$

Building upon the Lagrangian formalism outlined in Equation 3.5 the next step involves the derivation of the Hamiltonian, a fundamental descriptor of the system's energy landscape. This process necessitates the computation of the conjugate momentum through the Legendre transformation:

$$Q = \frac{\partial \mathcal{L}}{\partial \dot{\Phi}} = C\dot{\Phi} \ . \tag{3.6}$$

Then, we define the Hamiltonian of the system:

$$H = Q\dot{\Phi} - \mathcal{L} = \frac{Q^2}{2C} + \frac{\Phi^2}{2L} = \frac{1}{2}CV^2 + \frac{1}{2}LI^2 \ . \tag{3.7}$$

To transition from the classical framework to a quantum context, the system's Hamiltonian must undergo quantization. This process involves upgrading the classical charge and flux variables into quantum operators. Unlike classical coordinates, which comply with Poisson brackets:

$$\{\Phi, Q\} = \frac{\partial Q}{\partial Q}\frac{\partial \Phi}{\partial \Phi} - \frac{\partial \Phi}{\partial Q}\frac{\partial Q}{\partial \Phi} = 1 \ , \tag{3.8}$$

these quantum operators will adhere to the principles of *commutation relation* in quantum mechanics:

$$[\hat{\Phi}, \hat{Q}] = \hat{\Phi}\hat{Q} - \hat{Q}\hat{\Phi} = i\hbar \ . \tag{3.9}$$

By introducing the normalized flux, represented by $\hat{\phi} = 2\pi\frac{\hat{\Phi}}{\Phi_0}$, and the reduced charge, denoted by $\hat{n} = \frac{\hat{Q}}{2e}$, the quantum Hamiltonian of such a circuit can be then expressed as:

$$H = 4E_C\hat{n}^2 + \frac{1}{2}E_L\hat{\phi}^2 \ . \tag{3.10}$$

In the quantum mechanical framework of superconducting circuits, the Hamiltonian is characterized by a charging energy $E_C = \frac{e^2}{2C}$, representing the energy to add one electron of a Cooper pair to an island, and an inductive energy $E_L = (\frac{\Phi_0}{2\pi})^2/L$, linked to the superconducting magnetic flux quantum $\Phi_0 = \frac{h}{2e}$. The coefficient 4 in the term for charging energy within the LC Hamiltonian traces its roots to the origins of single-electron system analyses, and was subsequently extended to accommodate systems based on two-electron Cooper pairs.

The operators $\hat{n}$ and $\hat{\phi}$, denoting the excess number of Cooper pairs and the gauge-invariant phase, respectively, comply with the canonical commutation relation $[\hat{\phi}, \hat{n}] = i$.

3.3 Josephson Junction

The technology, discovered in 1962 by the English physicist Brian David Josephson and known as the *Josephson junction* [18], underpinning the most promising experimental implementations of superconducting qubits involves the use of superconducting metals separated by a weakly conductive barrier of nanometric dimensions.

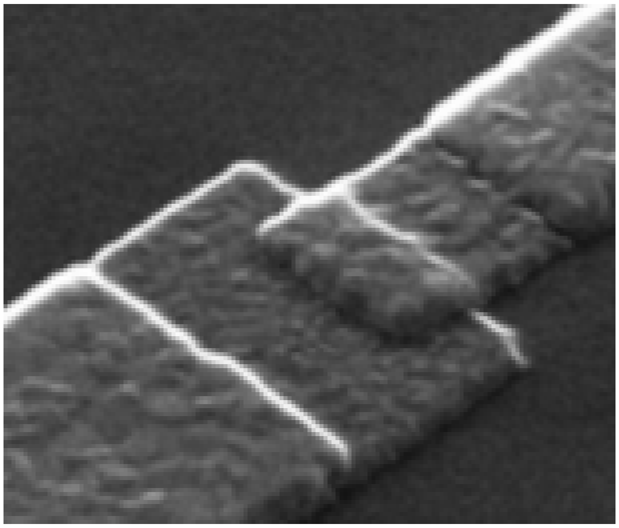

Figure 3.8: Josephson Junction developed at NIST for the QubIT Project: This image displays two Aluminum lines distinctly separated by an ultra-thin layer of Aluminum Oxide.

An example of such an experimental setup can be seen in Figure 3.8 and 3.9. Materials like semiconductors or insulators can be used as the barrier, or any configuration that effectively weakens the superconductivity of the system, including superconducting layers with a reduced cross-section.

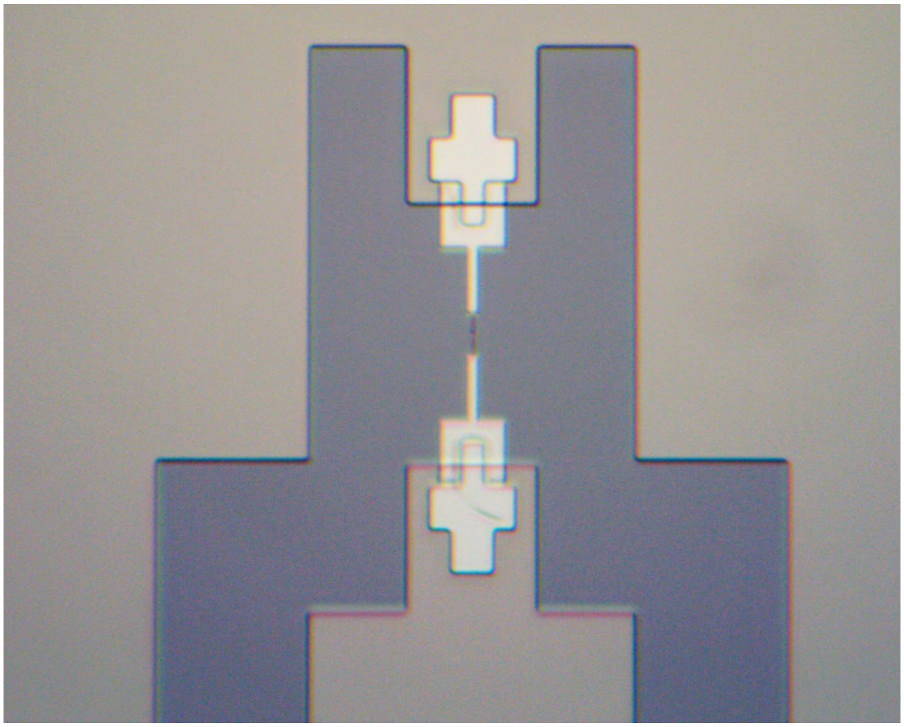

Figure 3.9: Josephson Junction manufactured at NIST for the QubIT Project: This image presents the complete structural layout of the Josephson junction.

By cooling these devices below the critical temperature of the superconductors comprising them, conduction through the weakly conductive barrier no longer follows Ohm's law, as the charge carriers in the material are not standard electrons but Cooper pairs. Despite the weakly conductive barrier, if the electromagnetic field exciting the current in the material has energy below the critical energy, the Cooper pairs remain intact and can tunnel through the barrier without developing a voltage difference across it, as can be seen from the graph in Figure 3.10.

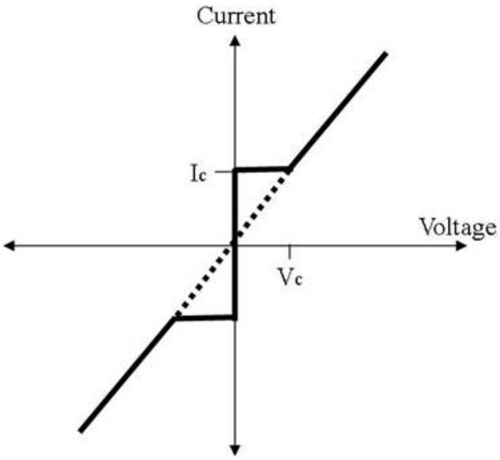

Figure 3.10: The image presents the voltage-current characteristic of a Josephson junction. It is observed that the resistance to the current flow remains zero up to a critical current value.

To understand this phenomenon, let us consider the following illustrative model of a Josephson junction. In this model, materials A and B correspond to superconducting materials (for simplicity, of the same type), and C represents the barrier made of weakly conductive material. This structure is schematically represented in Figure 3.11.

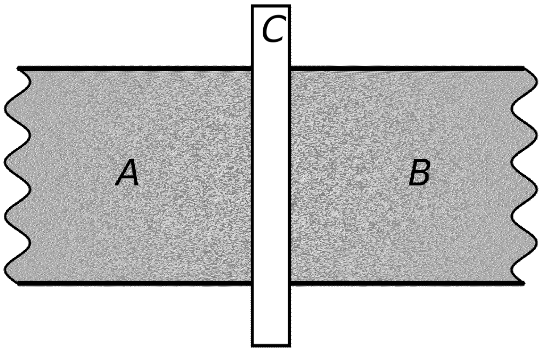

Figure 3.11: The image depicts the configuration of the materials that constitute a Josephson junction.

Let us analyze the ideal case, considering the junction in isolation. Since Cooper pairs are in a coherent state, it is possible to associate to them a common Schrödinger equation accounting for the time evolution of their density in materials A and B, such that:

$$i\hbar\frac{\partial\left|\psi\right\rangle}{\partial t} = \hat{H}\left|\psi\right\rangle \quad . \tag{3.11}$$

Wherein the state of the overall system, comprising the sub-systems A and B, is described by the following equation:

$$\left|\psi\right\rangle = \psi_A\left|A\right\rangle + \psi_B\left|B\right\rangle \quad . \tag{3.12}$$

Utilizing vector notation, we arrive at the following representation:

$$i\hbar\frac{\partial}{\partial t}\begin{pmatrix}\psi_A\\ \psi_B\end{pmatrix} = \begin{pmatrix}eV & K\\ K & -eV\end{pmatrix}\begin{pmatrix}\psi_A\\ \psi_B\end{pmatrix} \quad , \tag{3.13}$$

where ϕ_A and ϕ_B are defined as follows:

$$\psi_A = \sqrt{n_A}e^{i\phi_A} \quad , \quad \psi_B = \sqrt{n_B}e^{i\phi_B} \quad . \tag{3.14}$$

In this model, the terms ϕ_A and ϕ_B correspond to the global phase of the state vectors related to the Cooper pairs within materials A and B, respectively. Simultaneously, n_A ed n_B represent the number of Cooper pairs present in each of these materials.

The parameter V denotes the potential difference applied across the junction by an external generator, e is the charge of an electron, and K signifies the characteristic parameter of the junction. Notably, K functions to couple the two equations, taking into account the probability that the wave function related to material A can influence the Cooper pair density in material B, and vice versa.

Theoretically, the constant K could vary between the two materials. However, assuming equivalence simplifies the analysis, allowing us to consider K identical for both materials. To advance towards solving the system, we initially examine the partial time derivative related to superconductor A. It is pertinent to note the use of dot notation, where $\dot{x} = \frac{\partial x}{\partial t}$:

$$\frac{\partial}{\partial t}\sqrt{n_A}e^{i\phi_A} = \dot{\sqrt{n_A}}e^{i\phi_A} + i\sqrt{n_A}\dot{\phi}_A e^{i\phi_A} = (\dot{\sqrt{n_A}} + i\sqrt{n_A}\dot{\phi}_A)e^{i\phi_A} \quad . \tag{3.15}$$

Considering the Equation 3.13, we can show that:

$$(\dot{\sqrt{n_A}} + i\sqrt{n_A}\dot{\phi}_A)e^{i\phi_A} = \frac{1}{i\hbar}(eV\sqrt{n_A}e^{i\phi_A} + K\sqrt{n_B}e^{i\phi_B}) \quad . \tag{3.16}$$

Defining, as the *phase difference across the junction*:

$$\phi = \phi_A - \phi_B \quad , \tag{3.17}$$

we obtain the following equation:

$$\dot{\sqrt{n_A}} + i\sqrt{n_A}\dot{\phi}_A = \frac{1}{i\hbar}(eV\sqrt{n_A} + K\sqrt{n_B}e^{i\phi}) \quad . \tag{3.18}$$

The complex conjugate of the preceding equation is given by:

$$\dot{\sqrt{n_A}} - i\sqrt{n_A}\dot{\phi}_A = -\frac{1}{i\hbar}(eV\sqrt{n_A} + K\sqrt{n_B}e^{-i\phi}) \quad . \tag{3.19}$$

By adding the two previous equations, we eliminate the term $i\sqrt{n_A}\dot{\phi}_A$, thus obtaining:

$$2\dot{\sqrt{n_A}} = \frac{1}{i\hbar}(K\sqrt{n_B}e^{i\phi} + K\sqrt{n_B}e^{-i\phi}) = \frac{2K\sqrt{n_B}}{\hbar}\sin\phi \quad . \tag{3.20}$$

Since the following equation is valid:

$$\dot{\sqrt{n_A}} = \frac{\dot{n}_A}{2\sqrt{n_A}} \quad . \tag{3.21}$$

Substituting into the previous equation, we obtain:

$$\dot{n}_A = \frac{2K\sqrt{n_A n_B}}{\hbar}\sin\phi \quad . \tag{3.22}$$

Now, by applying a similar reasoning, we eliminate the term $\dot{n}_A$ by subtracting the two conjugate equations:

$$2i\sqrt{n_A}\dot{\phi}_A = \frac{1}{i\hbar}(2eV\sqrt{n_A} + K\sqrt{n_B}e^{i\phi} + K\sqrt{n_B}e^{-i\phi}) \ . \tag{3.23}$$

From the preceding equation, we derive the following:

$$\dot{\phi}_A = -\frac{1}{\hbar}(eV + K\sqrt{\frac{n_A}{n_B}}cos\phi) \ . \tag{3.24}$$

The following equations, which describe superconductor B, can be derived in a manner completely analogous to the equations pertaining to superconductor A:

$$\dot{n}_B = -\frac{2K\sqrt{n_A n_B}}{\hbar}\sin\phi \ , \tag{3.25}$$

$$\dot{\phi}_B = \frac{1}{\hbar}(eV - K\sqrt{\frac{n_B}{n_A}}cos\phi) \ . \tag{3.26}$$

The temporal evolution of the Cooper pair density, or the current density related to the Cooper pairs, is directly proportional to the current flowing through the material. Consequently, from the equations, it is inferred that the current exhibits a sinusoidal behavior with respect to the phase difference across the junction. This behavior is described by the following relationship:

$$I(t) = I_c\sin(\phi(t)) \ . \tag{3.27}$$

Here, I_c represents the critical current, a characteristic parameter of the device, which corresponds to the maximum supercurrent that can continuously flow through it. This is essentially the highest current that can traverse the material without inducing the emergence of a potential difference across the junction. The aforementioned equation is known as the *First Josephson Relation*.

From the previous equations, it is possible to deduce the behavior of the potential difference across the junction as a function of the temporal variation of the phase across the junction. Indeed, combining Equations 3.24 and 3.26 we obtain:

$$V(t) = \frac{\hbar}{2e}\dot{\phi}(t) \ . \tag{3.28}$$

The equation just described is referred to as the *Second Josephson Relation*. It reveals that applying a constant potential difference across the junction necessitates a linear temporal progression of the phase difference at the junction. This phenomenon corresponds to the establishment of an alternating current with a constant frequency. Now considering the energy stored by the junction during current flow, the First Josephson Relation dictates that:

$$I(t) = I_c\sin(\phi(t)) \ . \tag{3.29}$$

Suppose that at time $t = 0$, the junction is in its resting state, indicated by $\phi = 0$. The energy stored by the junction over a time interval is given by:

$$\begin{aligned} U &= \int_{\tau_0}^{\tau_1} IV dt = \frac{\hbar}{2e} \int_{\tau_0}^{\tau_1} I_c \sin\phi \cdot \frac{\mathrm{d}\phi}{\mathrm{d}t} dt \\ &= \frac{\hbar}{2e} \int_{\psi_0}^{\psi_1} I_c \sin\phi d\phi = -\frac{\Phi_0 I_c}{2\pi} \Delta(\cos\psi) \ . \end{aligned} \tag{3.30}$$

This demonstrates that the energy variation in the Josephson junction is solely dependent on the initial and final states of the junction, rather than the path taken between these states. Consequently, the energy stored in a Josephson junction qualifies as a state function. Mathematically:

$$U(\phi) = -\frac{\Phi_0 I_c}{2\pi} \cos\psi \ . \tag{3.31}$$

Here, the term $\Phi_0 = \frac{h}{2e}$ represents the magnetic flux quantum. We consider the reference term for the magnitude order of the stored energy, referred to as the *Josephson energy*:

$$E_J = \frac{\Phi_0 I_c}{2\pi} \ . \tag{3.32}$$

The energy stored by the junction depends solely on the current state of the system and corresponds to potential energy. At the circuit level, a Josephson junction can be compared to a non-linear dissipation-less inductor. Standard inductors store magnetic energy when a current passes through them. Contrary to ordinary inductances, Josephson junctions do not store magnetic energy; instead, the energy stored in the junction is *Josephson energy*, that is, the kinetic energy of charge carries.

However, from a practical standpoint, even though the energy stored within the junction does not equate to the storage of magnetic energy, it is expedient to define a *Josephson inductance* associated with the junction. This allows for straightforward treatment of the junction as a circuit element. To achieve this, we consider that the current passing through the junction has a specific phase difference ϕ_0 across it:"

$$I_0 = I_c \sin(\phi_0)) \ . \tag{3.33}$$

We hypothesize a current increase δ_I such that $\delta_I \ll I_0$, for which the following relation holds:

$$I_0 + \delta_I = I_c \sin(\phi_0 + \delta_\phi) \ . \tag{3.34}$$

By truncating the Taylor series expansion to the first order, we obtain:

$$\delta_I = I_c \cos(\phi_0)\delta_\phi \ . \tag{3.35}$$

Using the Second Josephson Relation, we deduce that the voltage across the junction is:

$$
\begin{aligned}
V &= \frac{\Phi_0}{2\pi}\dot{\phi} = \frac{\Phi_0}{2\pi}(\dot{\phi_0} + \dot{\delta_\phi}) \\
&= \frac{\Phi_0}{2\pi}\dot{\delta_\phi} = \frac{\Phi_0}{2\pi}\frac{\dot{\delta_I}}{I_c\cos(\phi_0)} \quad .
\end{aligned}
\tag{3.36}
$$

Comparing this equation with the characteristic equation of inductances:

$$
V = L\frac{\partial I}{\partial t} \quad . \tag{3.37}
$$

We can define the *Josephson inductance* as the quantity:

$$
L_J(\phi_0) = \frac{\Phi_0}{2\pi I_c\cos(\phi_0)} = \frac{L_J(0)}{\cos(\phi_0)} \quad . \tag{3.38}
$$

As observed from the preceding equations, the value of the inductance depends on the phase across the junction, and its minimum value (in absolute terms) is determined by the critical current of the junction. It is important to note from this definition that the inductance, unlike ordinary inductances, can also assume negative or infinite values, depending on the phase difference across the junction.

3.4 DC-SQUID

The DC-SQUID (Direct Current Superconducting Quantum Interference Device) is a device comprising two Josephson junctions in parallel, integrated into a superconducting loop.

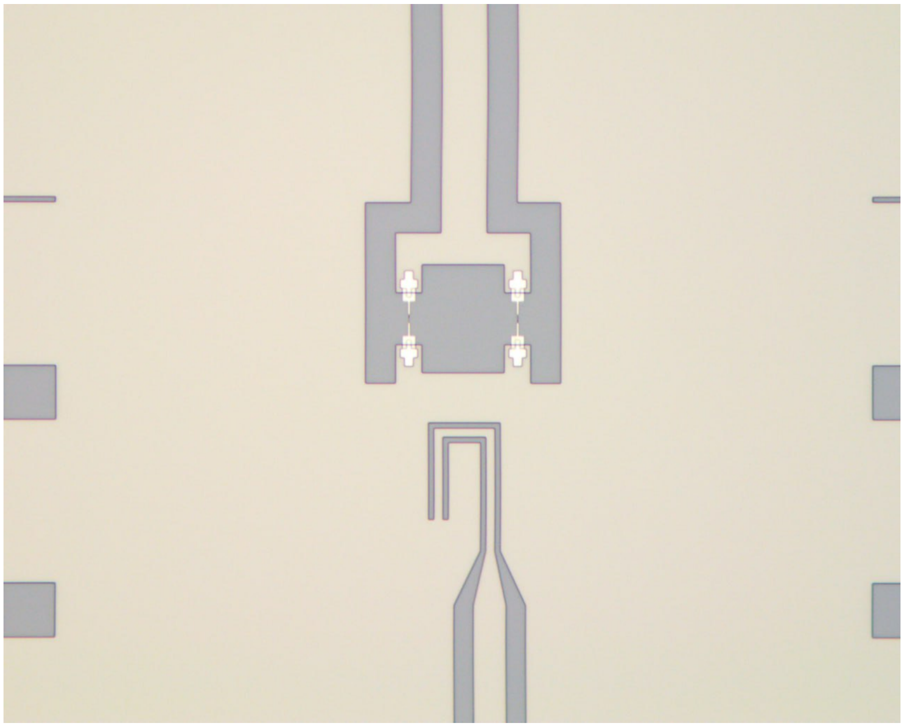

Figure 3.12: DC-SQUID manufactured at NIST for the QubIT Project: This image presents the complete structural layout of the DC-SQUID and flux bias line.

In the realm of quantum devices, a DC-SQUID is conceptualized as a variable Josephson junction, the properties of which can be modulated by an external magnetic flux. This characteristic enables the DC-SQUID to function as tunable dissipation-less non-linear inductance. In the scenario where the two junctions satisfy the following relationship:

$$E_1 = E_2 = E_J \ , \tag{3.39}$$

the DC-SQUID inductance can mathematically describes as:

$$L_{J,\mathrm{eff}}(\Phi_{\mathrm{ext}}) = \left(\frac{\Phi_0}{2\pi}\right)^2 \frac{1}{2E_J \cos\left(\frac{\Phi_{\mathrm{ext}}}{2}\right)} \ , \tag{3.40}$$

where Φ_{ext} denoted the magnetic flux chained into the DC-SQUID loop and Φ_0 is the magnetic flux quantum.

The external tunability of a DC-SQUID's parameters stands as a significant advantage, leveraged in the design of superconducting tunable qubits and parametric amplifiers. However, it is crucial to acknowledge that this flexibility can also present challenges. For instance, rendering a qubit tunable increases its vulnerability to external noise, which can couple as magnetic flux into the DC-SQUID, thereby detrimentally affecting the coherence performance of the device. Therefore, to harness the full potential of this feature, meticulous design considerations are imperative. These include implementing effective filtering of the flux bias line used to control it parameters and engineering the device layout to minimize undesired couplings with adjacent circuitry. Such thoughtful design strategies are essential to optimize the performance and reliability of these quantum devices.

Chapter 4

Transmon Quantum Processing Units Architecture and Design

In the evolving landscape of superconducting quantum computing, Transmon based Quantum Processing Units (QPUs) stand as the heart of computational power, driving the execution of quantum algorithms. In the field of superconducting QPUs, IBM is currently one of the most significant players. They have been making strides with their development roadmap, which includes an ambitious plan to unveil a 100000 qubit chip by the year 2033. This follows their recent achievement of launching the Condor and Osprey processor, which features respectively 1121 and 433 qubits. Such advancements are crucial milestones towards solving some of the world's most complex problems that today's supercomputers may not be able to handle.

Google has also marked a significant milestone in the field of superconducting quantum processing units. The company achieved a notable feat of quantum supremacy [19], albeit with a non-practical algorithm, using its Sycamore processor, which is equipped with 53 qubits. This achievement, while primarily of theoretical interest, represents a critical step forward in the demonstration of the capabilities of quantum computers to perform certain tasks exponentially faster than classical computers.

This starts exploring the physical implementation of Transmon qubits. The Transmon qubit, known for its relative insensitivity to charge noise and ease of fabrication, represents a significant advancement in quantum hardware and a de-facto standard for superconducting quantum devices. We will explore the fundamental principles underlying Transmon qubits, unraveling their operational mechanics and the features that make them suitable for integration into QPUs.

Condor

Pushing the limits of scale & yield

1,121

Superconducting qubits

50%

Increase in qubit density

1 mile +

Of flex cabling

IBM Quantum Summit
2023

Figure 4.1: 1121-Qubit chip produced by IBM: This chip not only contains an array of qubits but also includes resonators and control lines essential for qubit operation. *Source: IBM.*

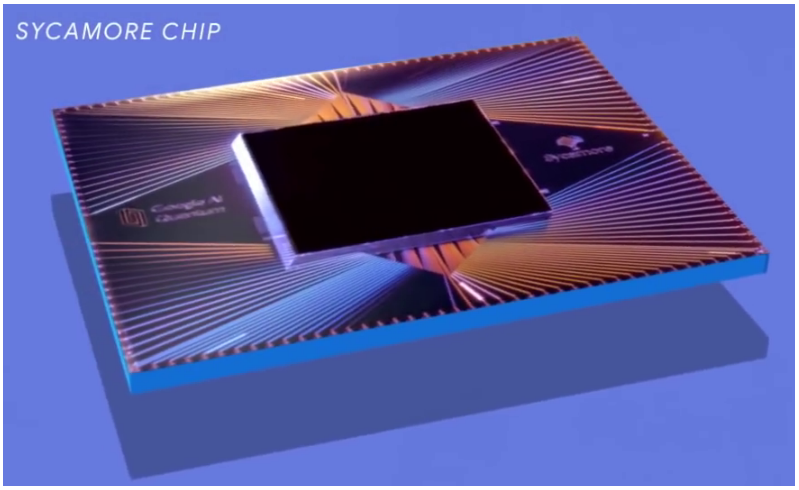

Figure 4.2: Sycamore quantum chip by Google: This advanced chip features an array of 53 qubits, complemented by essential resonators. Thanks to this remarkable chip, Google claimed the achievement of quantum supremacy since they employed it to completed a complex task in 200 seconds, that would take a 10,000 years to accomplish for state-of-the-art supercomputer. *Source: Google.*

Additionally, the chapter will provide an in-depth analysis of QPU design, architectural considerations and challenges. QPUs are sophisticated systems that not only contains qubits as their core computational units, but also integrate essential components such as LC resonators, drive lines, bias lines and coupling structures. This integration is crucial for performing quantum computations and for the effective control and readout of the quantum states of the qubits.

Furthermore, QPUs must be designed to operate in environments that minimize noise, quantum decoherence and unwanted interference. This requires not only advanced materials and fabrication techniques, but also innovative cooling and isolation technologies to maintain the qubits in a quantum coherent state as long as possible.

4.1 Transmon Qubit Design and Implementation

A qubit can conceptually be thought of as a non-linear resonator. In order to use a resonator as a qubit, it's essential to delineate a computational subspace constrained to two specific energy states for operational transitions, typically the lowest energy eigenstates, without inadvertently affecting other levels. The linear LC resonator discussed in the previous section has uniform energy level spacing thus presents a challenge for gate operations that rely on frequency discrimination.

To resolve the issue of unintentional engagement with non-computational states in a qubit system, it is necessary to incorporate an element of anharmonicity or non-linearity to the resonator. This is achieved through the insertion of a Josephson junction. This unique, non-dissipative circuit component is critical in the creation of superconducting circuits, as it alters the harmonic potential to introduce the desired non-linearity. Let's consider the Josephson junction as a lumped non-linear non-dissipative inductor.

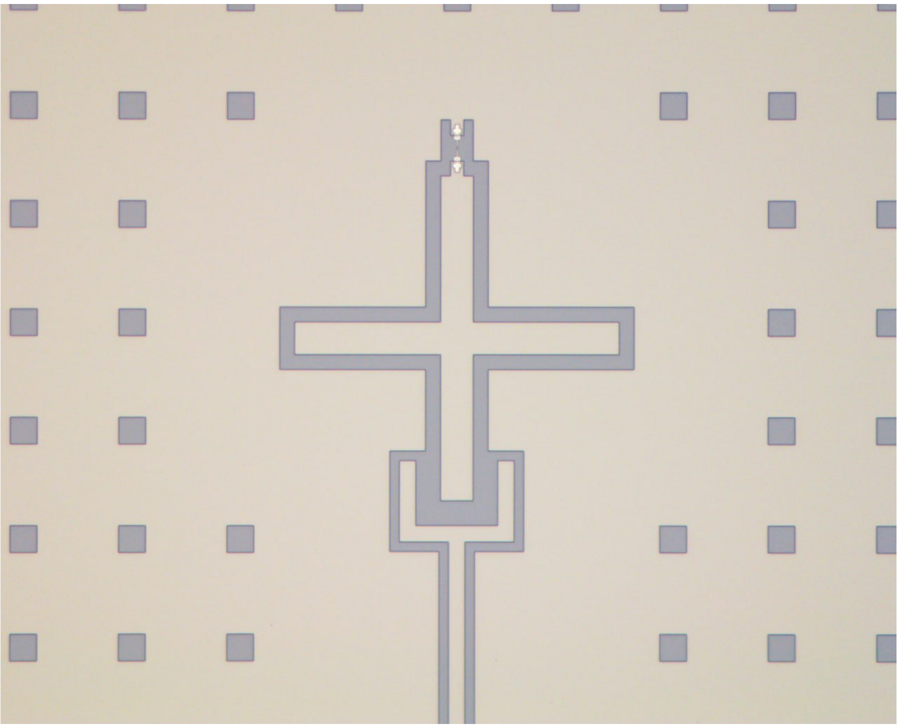

Figure 4.3: Transmon Qubit Manufactured at NIST for the QubIT Project: This image presents the complete structural layout of a Transmon qubit. The cross at the center of the image is the qubit, with its Josephson junction located at the top.

Mathematically speaking, an LC resonator where the inductance is implemented by a Josephson junction can be described by the following Hamiltonian:

$$H = 4E_C n^2 - E_J \cos(\phi) \ . \tag{4.1}$$

In this context, E_C is defined as $\frac{e^2}{2C_R}$, where C_R represents the total capacitance combining both the shunt capacitance C_s and the parasitic capacitance of the junction C_J. Additionally,

E_J is the Josephson energy, expressed as $\frac{I_c \Phi_0}{2\pi}$, with I_c being the critical current of the Josephson junction and Φ_0 the magnetic flux quantum. In the modified Hamiltonian, the potential energy has been replaced with the energy stored in the Josephson junction.

In the development of superconducting qubits [20], the relationship between Josephson energy (E_J) and charging energy (E_C) is pivotal. Superior functionality is realized when E_J significantly surpasses E_C, which mitigates the qubit's susceptibility to charge noise:

$$E_J \gg E_C \ . \tag{4.2}$$

This working regime is called *Transmon regime* [21]. From an hardware point, it is usually implemented shunting a Josephson junction (or a DC-SQUID) with a capacitance much larger than its parasitic capacitance:

$$C_s \gg C_J \ . \tag{4.3}$$

Figure 4.3 shows a Transmon qubit, wherein the cross structure functions as a shunt capacitance, significantly larger than the parasitic capacitance of the Josephson junction located at the apex of the cross. This expansive conductive area guarantees that the qubit operates within the Transmon regime, ensuring the desired performance characteristics.

In this regime, the superconducting phase ϕ shows only minor quantum fluctuations of ϕ values. Let's expand the potential term of Equation 3.19 into a power series, considering the small magnitude of ϕ:

$$E_J \cos(\phi) = \frac{1}{2} E_J \phi^2 - \frac{1}{24} E_J \phi^4 + \mathcal{O}(\phi^6) \ . \tag{4.4}$$

The first term of the series is the potential part of the harmonic behavior of the linear LC oscillator. The subsequent term introduces the necessary anharmonicity, deviating from pure linearity and enabling the discrete, non-equidistant energy levels required for qubit operation. Anharmonicity is mathematically defined as $\alpha = E_{12} - E_{01}$, representing the difference between the energy gap from the first to the second excited state and from the ground state to the first excited state.

In terms of physical realization, Transmon qubits are fabricated using techniques similar to those used in the conventional semiconductor industry, making them relatively easier to produce compared to other types of qubits. They are typically constructed using superconducting materials like aluminum on a silicon substrate.

The operation of Transmon qubits involves manipulating their quantum states using microwave pulses. These pulses induce transitions between the energy levels of the qubit, allowing for the execution of quantum gates. The design of the Transmon allows for precise control of these transitions, which is essential for performing complex quantum algorithms.

One of the key advantages of Transmon qubits is their scalability. The relatively simple design and robustness against noise make them suitable candidates for scaling up to larger quantum systems. This scalability is crucial for building quantum processors capable of tackling real-world problems that require a substantial number of qubits to perform complex calculations.

Furthermore, Transmon qubits can be coupled to microwave resonators for qubit readout and to other qubits for implementing two-qubit gates, both of which are essential for quantum computing.

4.2 Transmon Qubit Coupling and Entanglement

In order to describe the entanglement of distinct quantum systems, it's essential to construct an interaction Hamiltonian that interlinks the degrees of freedom within these systems:

$$H = H_1 + H_2 + H_{\text{int}} \ . \tag{4.5}$$

In the equation at hand, H_1 and H_2 represent the Hamiltonians corresponding to two separate quantum systems, in this case, two of the Transmon qubit previously described. The term H_{int} constitutes the interaction Hamiltonian that facilitates the coupling between the variables of the two systems. Within the domain of superconducting circuits, this coupling is achieved through an interaction mediated by the electromagnetic field.

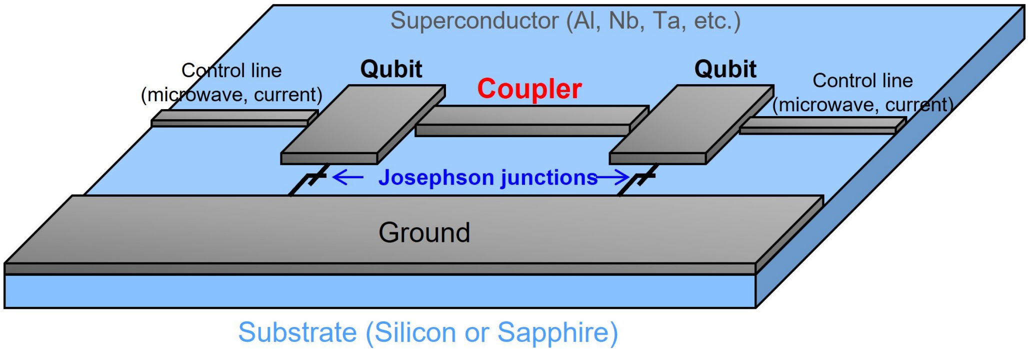

Figure 4.4: Conceptual diagram of two Transmon qubits coupled through a resonator. *Source: Toshiba.*

Probably the most common method of coupling qubits is the capacitive coupling method [7]. This type of coupling can be implemented by placing two qubits in close proximity to each other without the need for any additional external coupling structures. The interaction Hamiltonian for a capacitive coupling has the following form:

$$H_{\text{int}} = C_c V_1 V_2 \ . \tag{4.6}$$

In this configuration, C_c represents the capacitance that facilitates the coupling, while V_1 and V_2 correspond to the voltage operators at the respective nodes that are being interconnected. We can construct the following Hamiltonian adding the interaction term to the Hamiltonian of two uncoupled qubits:

$$H = \sum_{i=1}^{2} \Big(4E_{C_i} n_i^2 - E_{J_i} \cos(\phi_i) \Big) + 4e^2 \frac{C_c}{C_1 C_2} n_1 n_2 \ . \tag{4.7}$$

In case where we have an inductive coupling [7] the interaction terms can be modeled as follow:

$$H_{\text{int}} = M_c I_1 I_2 \ , \tag{4.8}$$

In this context, M_c represents the mutual inductance between the two qubit circuits, while I_1 and I_2 correspond to the loop current operators. The construction of the complete Hamiltonian for the coupled system mirrors the principles applied in capacitive coupling; it necessitates the integration of the individual Hamiltonians of the two isolated qubits with an interaction term reflective of mutual inductance. This interaction term is not merely a mathematical construct but a physical representation of the quantum entanglement between qubits, which is the cornerstone of multi-qubit quantum logic operations and error correction mechanisms.

4.3 Structure and Functionality of Transmon QPUs

The design of a Transmon-based Quantum Processing Unit (QPU) is anchored on the Transmon qubit. This can be structured using either a grounded or floating topology for the shunt capacitance, which constitutes a major portion of the chip. There's no particular advantage choosing the former or the latter, so the decision on which architecture to use in a design can be led by other constraints.

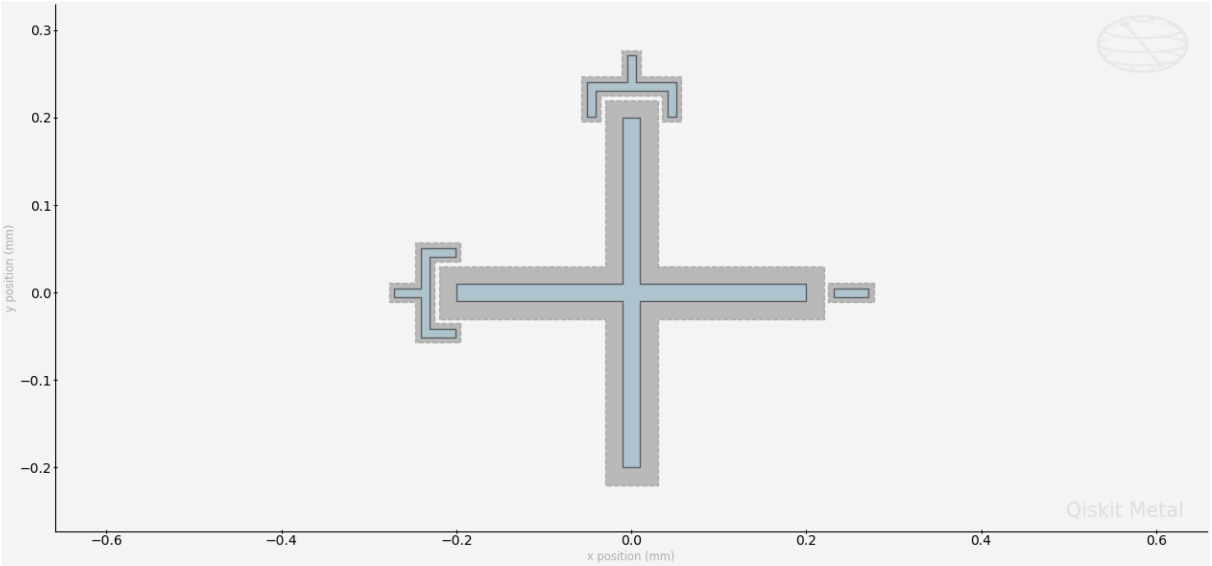

Figure 4.5: Grounded Transmon Qubit: In this design, a Josephson junction is placed at the right end of the superconducting cross, which serves as the shunt capacitance necessary for operating in the Transmon regime. It is termed 'grounded' because the Josephson junction is connected to the ground plane (depicted by the white patch surrounding the qubit). This topology is used by Google quantum processors. *Source: Qiskit Metal (IBM).*

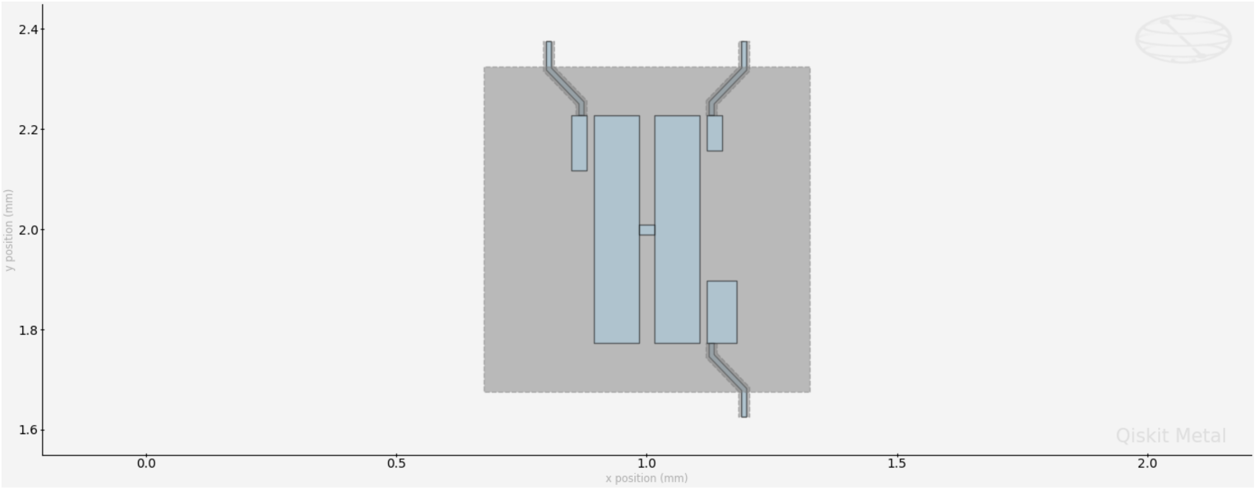

Figure 4.6: Floating Transmon Qubit: This design features a Josephson junction placed between two superconducting pads, which act as the shunt capacitance necessary for operating in the Transmon regime. It is termed 'floating' as the Josephson junction is not grounded. This topology is used by IBM quantum processors. *Source: Qiskit Metal (IBM).*

Typically, the Transmon is dispersively coupled to an LC resonator. In dispersive coupling, the interaction between the Transmon and the resonator is sufficiently weak to prevent energy exchange, yet strong enough to allow for the inference of the qubit's state through the resonator, without destroying the qubit measured state through the measuring process. It's crucial to understand that while this *non-destructive measurement* approach does not interfere with the qubit's actual eigenstate extrapolation during the measurement process, it does not prevent the collapse of the qubit's wavefunction into one of its eigenstates post-measurement.

Drive lines are a critical component of a QPU, responsible for transmitting the electromagnetic pulses necessary for manipulating the qubit's state, specifically its rotations around the x and y axes of its Majorana-Bloch sphere. These lines are typically capacitively coupled to the Transmon qubit structure, with a relatively minor coupling strength, typically in the order of ≈ 100 aF. This modest coupling is deliberately designed to minimize the intrusion of external noise and disturbances into the qubit from drive lines. It's vital to remember that the control electronics for both driving and reading out the qubit state are located outside the QPU. If not meticulously managed during the design phase, this external interfacing could introduce noise and disruptions into the QPU, potentially degrading its performance significantly or even rendering it inoperative.

In QPU, structures that facilitate the coupling between multiple qubits are vital for enabling quantum entanglement. The design approaches for these coupling structures can vary significantly. One common method, particularly for neighboring qubits in close proximity on the chip, is capacitive coupling, which, while seemingly straightforward, involves intricate design considerations. More complex techniques include the use of fixed or tunable resonators for qubit coupling. Of particular note are tunable resonators [22, 23], which, despite their increased spatial requirements and design complexity, offer the significant advantage of being able to activate or deactivate qubit coupling on demand. When deactivated, these resonators can effectively isolate qubits, providing greater control and flexibility during qubit manipulation. This feature is crucial in complex quantum operations, balancing the need for qubit interaction with the necessity of maintaining qubit isolation to prevent unintended entanglements or noise interference.

A critical aspect of the Transmon QPU's design is the integration of qubits into a larger circuit framework. This aspect becomes increasingly crucial as the complexity of the QPU grows, with a higher number of qubits and related structures. Precise fabrication is essential for realizing a functional QPU, as it ensures that qubits and resonators are created with the specific frequencies, quality factors (Q), and coupling characteristics initially determined during simulation phases. Deviations from these intended values can result in frequency overlaps or unintended couplings between different components on the chip, leading to performance issues. Managing these fabrication challenges is one of the most critical and ongoing areas of research in the field of quantum hardware [24]. Achieving high precision in manufacturing is fundamental to scaling up and efficiently operating large-scale QPUs.

For the next section of this chapter, I will delve into a Transmon QPU to which I have significantly contributed in terms of design. This examination will encompass a thorough exploration of each core component of the QPU, elucidating the rationale and considerations that guided their design.

4.4 Case Study: Transmon QPU Developed at INFN

The Transmon QPU developed at the Istituto Nazionale di Fisica Nucleare (INFN) for the QubIT project represents a significant step for the Italian superconducting quantum computing research [2, 3]. This section offers a comprehensive case study of the Transmon QPU at INFN, highlighting its design features, technological advancements, and the challenges overcome during its development. While this section builds upon the knowledge of the basic building blocks and design principles of the Transmon QPU, revisiting it after exploring the entirety of the thesis is recommended for a more thorough understanding of the rationale behind its development.

INFN, renowned for its contributions to physics research, ventured into quantum computing with the aim of leveraging its expertise in high-energy physics and material science. This initiative's primary objective was to develop an advanced axion detector utilizing Transmon qubit technology. While the chip primarily functioned as a sensor, its design paralleled that of a typical Transmon Quantum Processing Unit. Consequently, the research team's initial approach was to design and construct a functional QPU. This would serve both as a preliminary prototype for the detector and as a means to evaluate various designs of qubits and resonators.

Our design stack was based on Qiskit Metal [25], an open-source Python framework and library dedicated to the design of superconducting quantum chips and devices. To facilitate the classical electromagnetic simulations necessary for defining quantum parameters, Qiskit Metal seamlessly interfaces with Ansys's HFSS and Q3D software. This integration enables a comprehensive simulation environment, crucial for the accurate design and analysis of superconducting quantum circuits. The endeavor provided an opportunity to assess the effectiveness of simulation tools, as well as to understand the impact of the fabrication process on the final performance of the chip.

Qiskit Metal has significantly accelerated the design process. It has proven to be invaluable for extracting quantum parameters from circuits and simplifying layout design, tasks that are more cumbersome when performed directly in Ansys software. Qiskit Metal can script Ansys to create chip layouts, set up electromagnetic simulations, and execute them. Despite these conveniences, it is crucial to monitor the interaction between these software tools, as automation can sometimes yield unexpected results. In particular, ensuring that Qiskit Metal scripts HFSS with an appropriately defined mesh is essential for obtaining meaningful simulation results, especially for calculating the quality factors of resonators. Additionally, conducting a sufficiently high number of simulation passes is vital to ensure their convergence. Another significant benefit of using Qiskit Metal, given that it is a Python library, is the ability to implement version control via Git. This functionality has been instrumental in managing the code used to generate the designs for quantum devices. It allows for straightforward modifications and the capability to revert to previous versions of the designs when necessary.

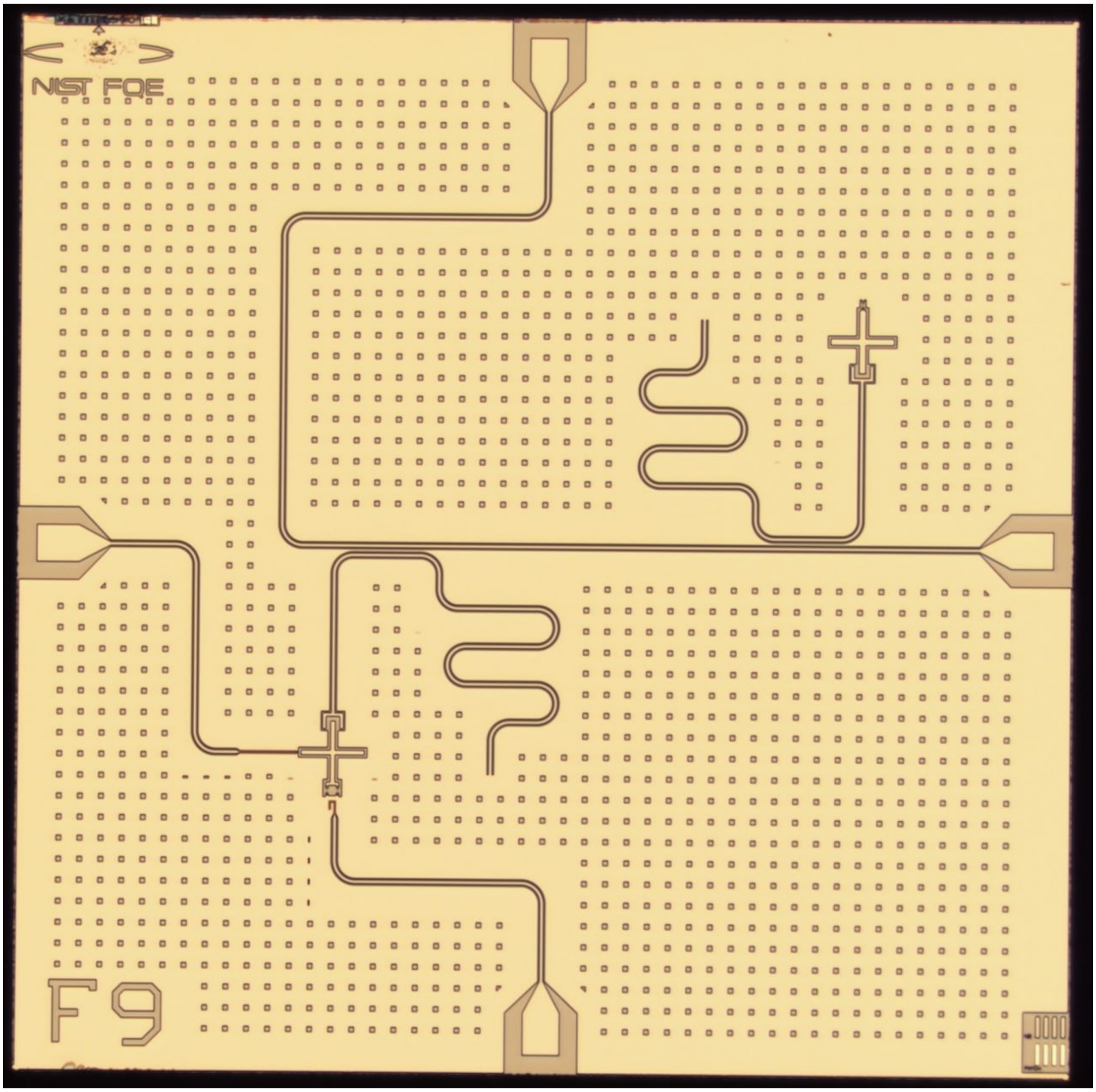

Figure 4.7: Image of a Test Quantum Chip Produced at NIST: Showcasing the two qubits and their readout resonator, as well as the feedline and control lines.

The QPU presented in this section (Figure 4.7) has been manufactured and measured by the Superconductive Electronics Group at the National Institute of Standards and Technology (NIST) in Colorado United States. The significant adaptation of our chip design to the NIST manufacturing standards was primarily achieved through the expertise and dedicated efforts of my colleague, Danilo Labranca, who played a very important role in both the chip design and this crucial aspect of our project.

Unfortunately, despite NIST expertise in crafting such devices, the QPU encountered some fabrication errors that adversely affected its coherence time performance. This situation underscores the critical importance of precise chip fabrication in achieving a high-performing Quantum Processing Unit. It highlights that even for seasoned manufacturers, ensuring flawless fabrication is still a challenging and non-trivial task, fundamental for the overall success and efficiency of the QPU.

The quantum chip in question integrates two qubits, each capacitively coupled to a quarter-wave resonator for readout purposes. Additionally, it features a 50 ohm feedline and a 50 ohm drive line for each qubit. Notably, one of these qubits is engineered with a fixed frequency, while the other is designed to be frequency-tunable. This tunability is achieved through the introduction of a DC-SQUID and a bias line, controlled by a dc current, that allows the induction of an external magnetic flux into the DC-SQUID, thus allowing for dynamic frequency adjustments.

The QPU was meticulously constructed on a 380 nm high-resistivity silicon substrate, layered with a 100 nm thick film of Niobium superconductor. The critical Josephson junctions were fabricated employing an Al-AlOx-Al stack structure. Notably, the Niobium layer underwent a selective etching process even in the areas designated for the Josephson junctions, ensuring precision in the device's architecture. This careful material selection and processing technique are instrumental in optimizing the QPU's performance characteristics.

A pivotal goal of this fabrication process was to evaluate the congruence between simulated and realized circuit parameters. Establishing this correspondence is essential to validate the reliability of the design framework, laying the groundwork for the advancement to more complex quantum circuitry.

In addition to verifying the alignment between simulation and fabrication parameters, it was essential to evaluate several key performance indicators of the qubit system. This included assessing the control over the qubit state, the tunability of the qubit frequency, the effective coupling between the qubit and its readout resonator, and the durations of coherence times. These aspects are critical for the practical application and operational reliability of these qubit designs.

The measurement of the fixed qubit readout resonator whose resonant frequency was determined to be 7.573 GHz, closely aligning with the designed frequency of 7.6 GHz.

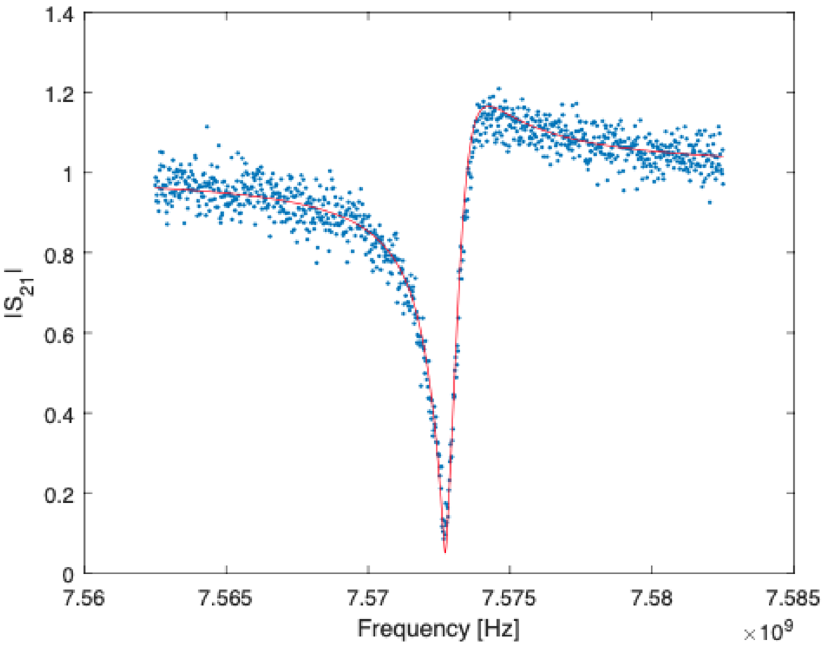

Figure 4.8: Spectroscopy of the fixed-frequency qubit readout resonator: This image displays the resonant frequency of the readout resonator.

Unfortunately, the resonator's quality factor fell short of the anticipated benchmarks. Specifically, the coupling quality factor Q_c was measured at $5.063 \cdot 10^3$, and the internal quality factor Q_i at $5.624 \cdot 10^4$, significantly lower than the expected 10^6 magnitude for Q_i.

In the spectroscopic analysis of the fixed-frequency qubit, the measured frequency f_{01} was found to be 5.689 GHz. This value is remarkably close to the 5.682 GHz frequency predicted by the Lumped Oscillator Model (LOM) quantum simulation, an integral component of Qiskit Metal. This close alignment between the observed and predicted values significantly reinforces the predictive precision of the simulation in this specific application.

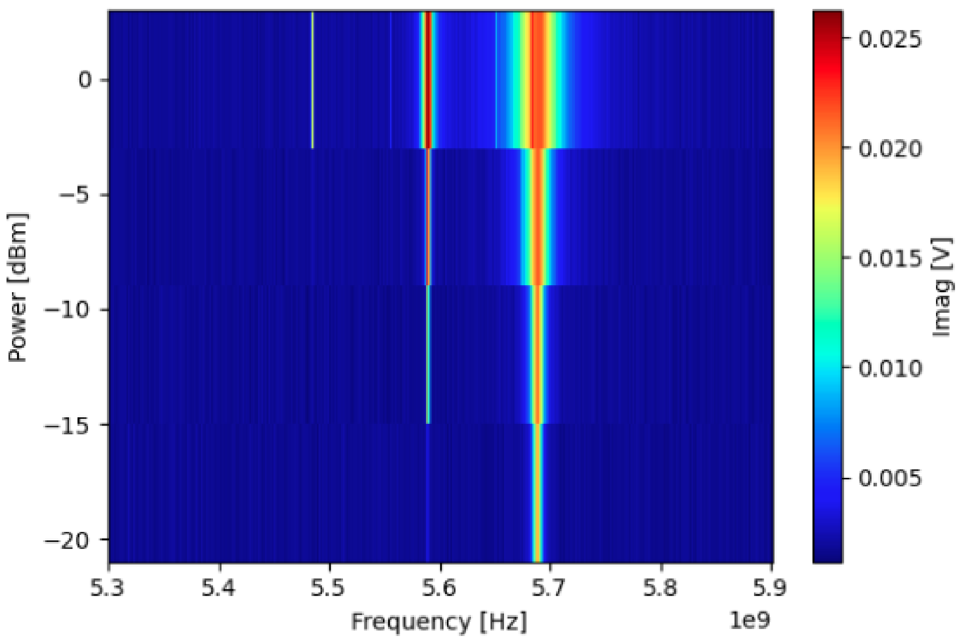

Figure 4.9: Spectroscopy of the fixed-frequency qubit: This image displays the resonant frequency f_{01} (the first peak from the right), along with $f_{02}/2$ (the second peak from the right) – representing half the transition frequency between the ground and second energy levels excitable at high powers, and f_{12} (the third peak from the right) – denoting the transition between the first and second energy levels.

The anharmonicity value $\alpha/2\pi$, considering $\hbar = 1$, was observed to be -204 MHz. This measurement closely aligns with the -206 MHz value predicted by the LOM simulation, further evidencing the simulation's accuracy in replicating experimental outcomes.

The measured Josephson inductance of the fabricated fixed-frequency qubit's Josephson junction was observerd to be 7.641 nH. This contrasts with the 7.2 nH value initially employed in conducting the quantum simulation, indicating a notable discrepancy between the experimental device and the simulation parameter.

While the previously mentioned parameters exhibited remarkable performance and accordance with the simulations, the qubit's T_1 longitudinal relaxation time demonstrated a notably poor behavior far from the performances achieved in state-of-the-art devices [26]. In fact, the measured T_1 approximated 4 µs, a value significantly lower than the Purcell-limited T_1 (i.e., the maximum achievable T_1 under Purcell effect constraints), which was calculated to be around 40 µs for this particular device. The Purcell limited T1 was estimated from the qubit's decay rate through its readout resonator, using the following equations [27]:

$$T_{\text{Purcell}} = \frac{1}{\Gamma} \ , \tag{4.9}$$

$$\Gamma = \left(\frac{g}{\Delta}\right)^2 \frac{\omega_r}{Q} \ , \tag{4.10}$$

where g denotes the qubit-resonator coupling rate, Δ represents the detuning between the qubit and resonator excited mode frequencies, Q corresponds to the resonator loaded quality factor, and ω_r is the resonator excited mode frequency.

Moreover, the T_2 transverse relaxation time performance was not exceptional, with the measured value of approximately 6 µs.

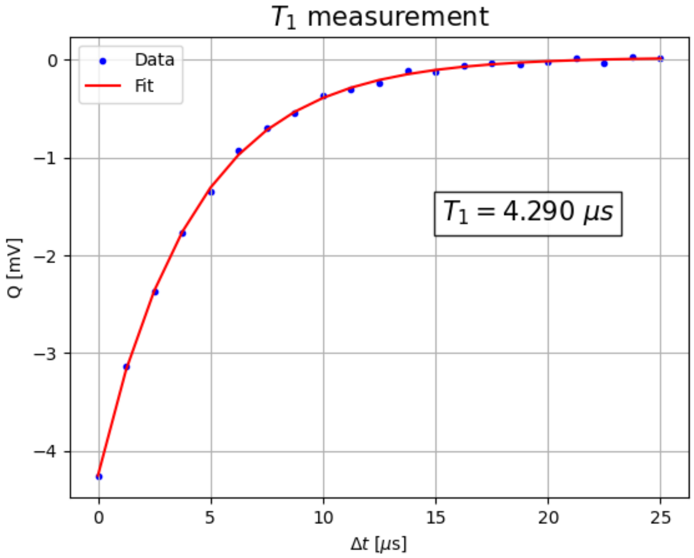

Figure 4.10: Fixed-frequency qubit: Measurement of the T_1 longitudinal relaxation time.

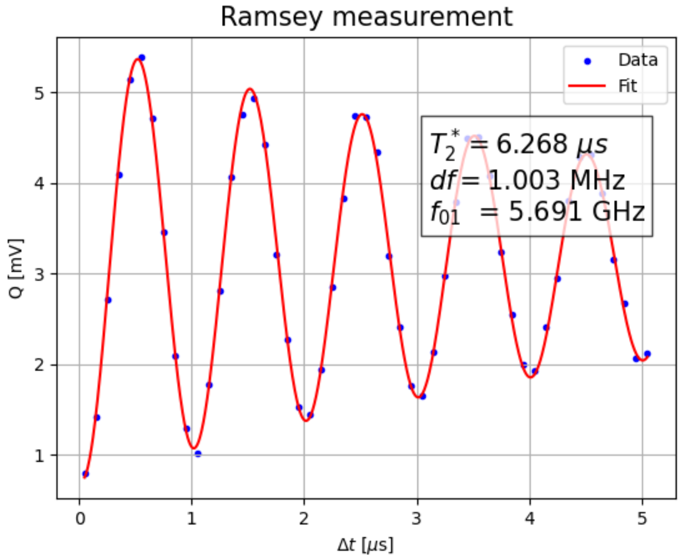

Figure 4.11: Fixed-frequency qubit: Ramsey measurement of the T_2 transverse relaxation time.

The tables below provide a comparative overview of the design and measured parameters for the fixed-frequency qubit.

Table 4.1: Fixed Qubit Resonator Comparison of Design and Measurement Parameters

Parameter	**Design**	**Measurement**
Resonant Frequency	7.6 GHz	7.573 GHz
Q_i	10^6	$5.624 \cdot 10^4$

Table 4.2: Fixed Qubit Comparison of Design and Measurement Parameters

Parameter	**Design**	**Measurement**
f_{01}	5.682 GHz	5.689 GHz
$\alpha/2\pi$	-206 MHz	-204 MHz
Josephson inductance	7.2 nH	7.641 nH

The spectroscopic analysis of the tunable qubit readout resonator revealed a resonant frequency of 7.403 GHz, aligning remarkably well with the design objective of 7.4 GHz. Given that the readout resonators of both qubits are interconnected via a feedline, meticulous design considerations were implemented to prevent frequency collisions by ensuring their resonant frequencies were neither identical nor excessively proximate.

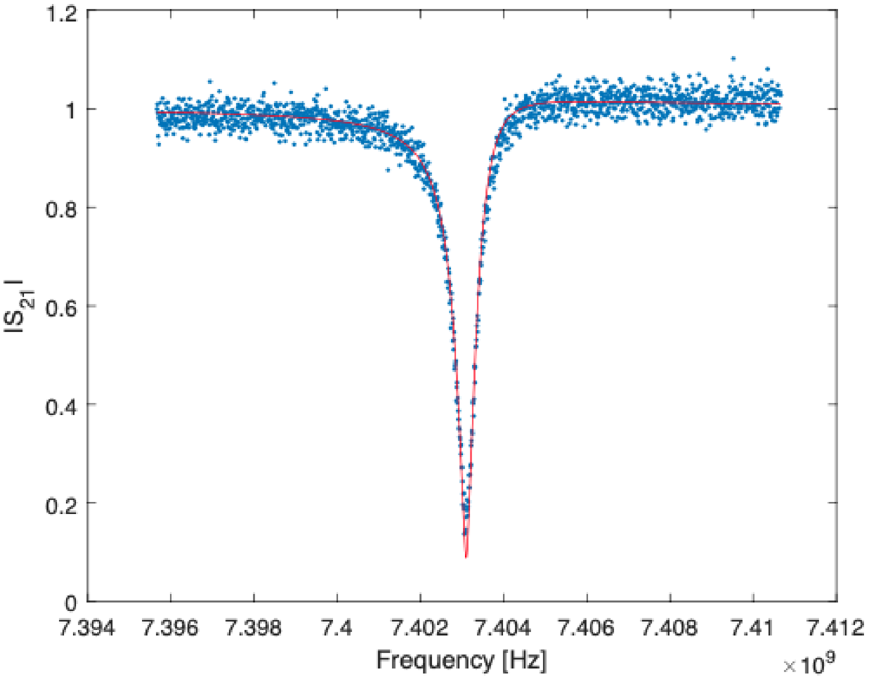

Figure 4.12: Spectroscopy of the tunable-frequency qubit readout resonator: This image displays the resonant frequency of the readout resonator.

The assessment of the quality factors also reflected the device's persistently sub-optimal performance. The coupling quality factor, Q_c, was recorded at $9.673 \cdot 10^3$, and the internal quality factor, Q_i, at $4.927 \cdot 10^4$. These values are notably inferior to the anticipated magnitude of 10^6 for Q_i.

The tunable qubit lowest measured frequency f_{01} was found to be 5.649 GHz. This value is in accordance with a LOM simulation that adopts a Josephson Inductance L_J of 7.9 nH. However, the measured Josephson inductance of the DC-SQUID was observed to be 8.364 nH at that frequency. Similarly, in this instance, a significant deviation was observed between the experimental device's performance and the parameters set in the simulation.

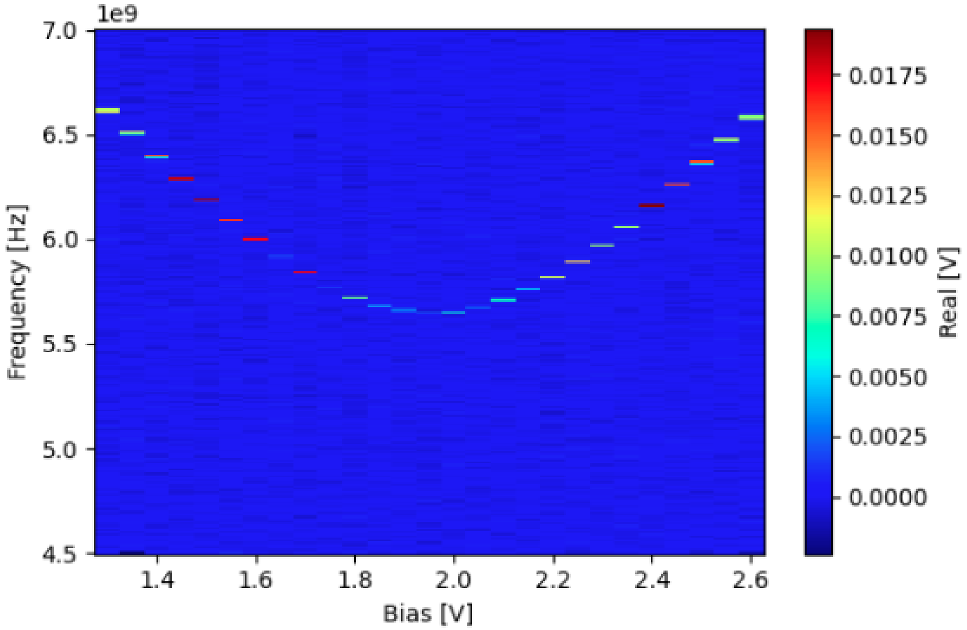

Figure 4.13: Spectroscopy of the tunable-frequency qubit: This image displays the frequency span achievable with this qubit.

Owing to the inferior quality factors, the measured T_1 relaxation time of the tunable qubit was approximately 3 µs. Furthermore, the T_2 performance was similarly disappointing, with a measured value of around 4 µs.

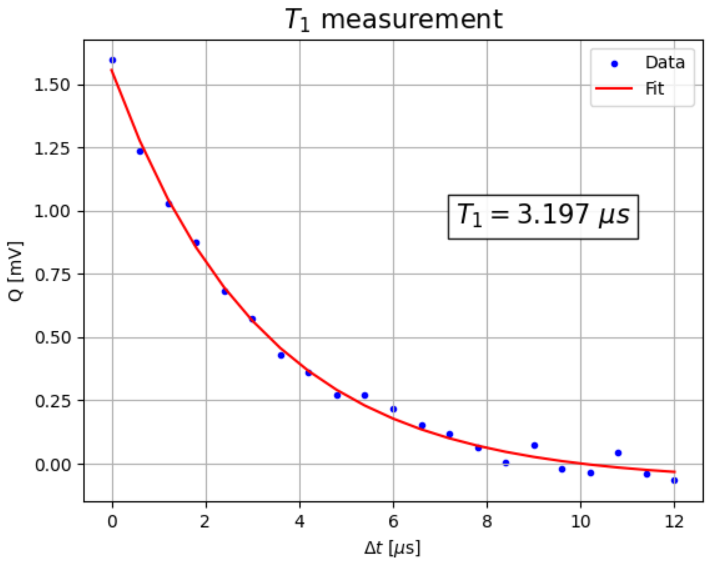

Figure 4.14: Tunable-frequency qubit: Measurement of the T_1 longitudinal relaxation time.

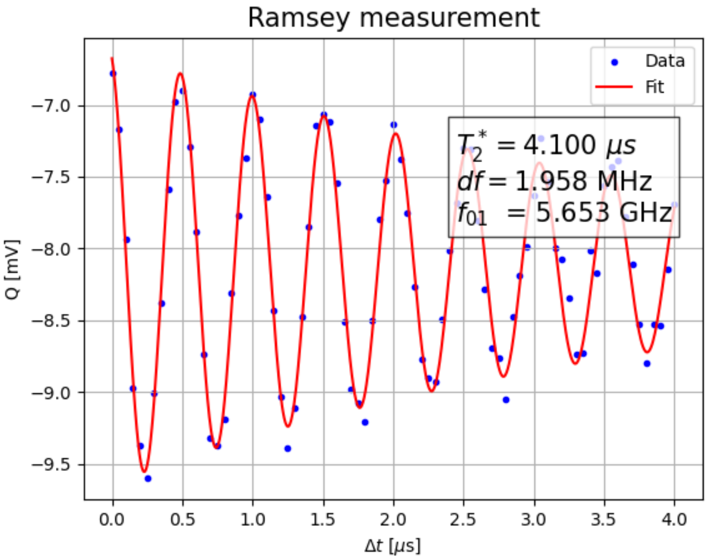

Figure 4.15: Tunable-frequency qubit: Ramsey measurement of the T_2 transverse relaxation time.

In this context, it is noteworthy to mention the analysis of the cavity spectroscopy against the voltage bias of the tunable qubit exhibits a distinct *avoided crossing* pattern. In fact, when the qubit frequency nears that of the resonator, a gap of approximately 200 MHz becomes observable. Theoretical predictions expect it to be twice the value of g, that is, the coupling rate between the qubit and the readout resonator. Utilizing the Electromagnetic Participation Ratio (EPR) [28] simulation, another tool provided by Qiskit Metal for simulating quantum device parameters, g is calculated to be 104 MHz. This figure closely corresponds with the measured values, demonstrating the accuracy of the simulation. Contrarily, the Lumped Element Model (LOM) analysis estimates g to be approximately 49 MHz, which in this instance, underestimates the coupling rate compared to the actual device measurements.

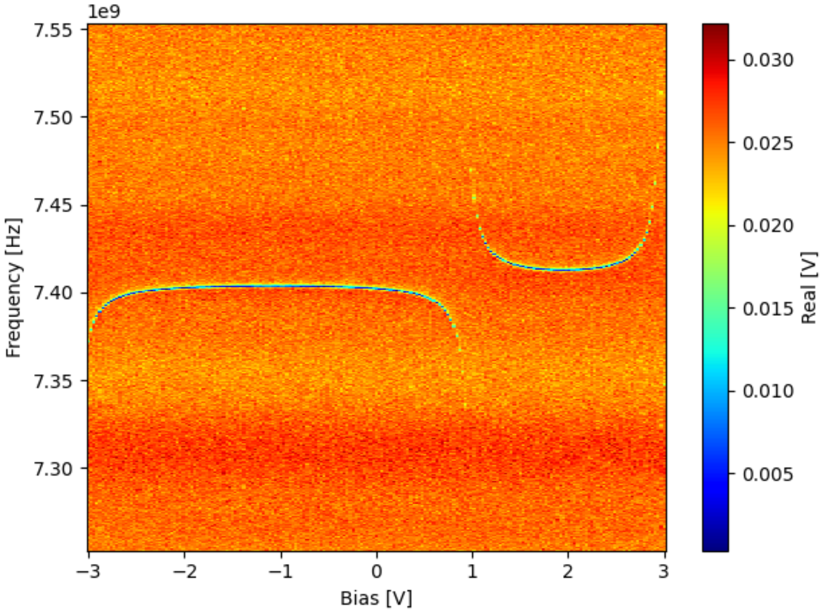

Figure 4.16: Tunable-frequency qubit readout resonator: frequency range influenced by coupling to a tunable qubit.

The tables below provide a comparative overview of the design and measured parameters for the tunable-frequency qubit.

Table 4.3: Tunable Qubit Resonator Comparison of Design and Measurement Parameters

Parameter	**Design**	**Measurement**
Resonant Frequency	7.4 GHz	7.403 GHz
Q_i	10^6	$4.927 \cdot 10^4$

Table 4.4: Tunable Qubit Comparison of Design and Measurement Parameters

Parameter	**Design**	**Measurement**
Josephson inductance @ f_{01}=5.649 GHz	7.9 nH	8.364 nH
g	104 MHz (EPR) / 49 MHz (LOM)	100 MHz

Even if not perfectly functioning, The QPU development has been instrumental to deepen the understanding of quantum hardware development, moving from the pure theoretical approach to the challenges that encompass an actual hardware implementation.

In conclusion, this section has presented a comprehensive overview of a device to which I have significantly contributed in terms of design. The coherence between our simulations and the experimental measurements is a confirmation to the robustness of our design approach, with the predicted frequencies and couplings closely mirroring those observed experimentally.

Future wafer productions are planned to discern whether the low quality factors are attributable to fabrication methods rather than design errors, with additional investigation into the potential influence of fridge grounding. The impact of the flux line on dissipation emerges as another area for further research.

The design initially fabricated at NIST has also been successfully modified for production at Fondazione Bruno Kessler (FBK), marking a significant step in the advancement of quantum device development in Italy. Additionally, we are in the process of developing a novel design for a two-coupled qubit chip, an initiative that holds the potential to considerably enhance our comprehension and technical proficiency in the realm of quantum computing.

Chapter 5

Controlling the Quantum Processing Unit

Control over Quantum Processing Units is a vital aspect that underpins the functionality and effectiveness of quantum computing [29, 30]. This chapter delves into the topic of QPU control, exploring the principles, techniques, and challenges involved in manipulating and managing the quantum states within these advanced computing systems. The operation of QPUs involves initializing qubits into specific states, executing quantum gates to manipulate these states, and finally reading out the results, all while maintaining the delicate quantum coherence essential for accurate computations.

A substantial section of this chapter is devoted to the methods employed for interfacing with qubits. The control technologies discussed herein predominantly utilize control signals based on microwave pulses. As quantum systems grow in complexity, the demand for advanced control algorithms and the development of both hardware and software capable of automating and refining the control process becomes increasingly critical. Consequently, researchers have investigated the application of optimal control techniques in the management of qubits. Given the extensive focus on this topic during my PhD research, I will include a case study in this chapter, enriching it with experimental results and practical insights.

Figure 5.1: Qblox control electronics connected to a quantum computer. *Source: Qblox.*

In conclusion, this chapter provides a comprehensive overview of the control of QPUs, highlighting the delicate balance between theoretical principles, engineering practices, and technological advancements required to operate these sophisticated quantum systems. Effective control of QPUs is not just about manipulating qubits; it is about harnessing the full potential of quantum mechanics to open up new frontiers in computing power.

5.1 Fundamentals of Qubit Control and Gate Implementation

The control of qubits and the implementation of quantum gates are foundational aspects of quantum computing. This section delves into the fundamental concepts and methodologies that underpin these crucial processes, laying the groundwork for understanding how quantum computers manipulate information at the quantum level.

Qubit control is the precise manipulation of the fundamental unit of quantum information, the qubit. This intricate process begins by initializing the qubit into a defined state, typically achieved by allowing the qubit to stabilize in its ground state. To reach this initial state, one must wait for a duration exceeding the qubit's T_1 longitudinal relaxation time, that is, the period it requires to naturally decay to its lowest energy level.

Quantum gates are the quantum equivalent of classical logic gates and are the building blocks of quantum algorithms. Implementing a quantum gate involves applying specific operations to one or more qubits, altering their states in a controlled manner. These operations can range from simple single-qubit rotations, which change the state of a single qubit, to more complex multi-qubit gates, which entangle multiple qubits and are essential for harnessing the full power of quantum computing. Mathematically speaking, a closed quantum system time evolution is described by the time-evolution operator (or propagator) obtained solving the Schrödinger equation:

$$\hat{U}(t) = e^{-i\hat{H}t/\hbar} \ . \tag{5.1}$$

Therefore, the implementation of a target gate operation necessitates the design of the system's Hamiltonian. This design ensures that the subsequent unitary evolution of the qubits realizes the intended quantum gate function, that is, quantum state time evolution:

$$|\psi(t)\rangle = \hat{U}(t)\,|\psi(0)\rangle \ . \tag{5.2}$$

To enable the realization of any possible unitary transformation, and thereby achieve universal computation, it is possible to define various sets of quantum gates. These sets, referred as *universal sets*, when applied in an appropriate finite sequence, can approximate any transformation with arbitrary accuracy:

$$\|\hat{U} - \hat{U}_N ... \hat{U}_2\hat{U}_1\| < \epsilon \ , \tag{5.3}$$

where $\|...\|$ is a norm operation, and ϵ represents the figure that defines the approximation accuracy, and can be made arbitrary small.

Let's consider the pure state of a qubit using the following notation:

$$|\psi\rangle = \alpha\,|0\rangle + \beta\,|1\rangle \ . \tag{5.4}$$

It is often convenient to represent the state of a qubit using vector notation, especially when studying the transformations applied to the system in the form of unitary matrices applied to the vector describing its state. According to this approach, once a basis of eigenstates is defined, the operator associated with it is considered as a matrix. The particular matrix representation of the operator depends on the chosen basis of eigenstates and is not unique. The following is the vector notation for the state of a generic qubit when the vectors $|0\rangle$ and $|1\rangle$ are chosen as the basis:

$$|\psi\rangle = \begin{pmatrix} \alpha \\ \beta \end{pmatrix} \ . \tag{5.5}$$

Both notations are equivalent and describe the same physical entity; the choice between them depends solely on the context.

In quantum computing, a universal gate set is a vital toolkit comprising quantum gates that can simulate any quantum operation to a desired degree of precision. As an example. it is possible to consider the specific universal gate set that includes the Hadamard (H), Phase (S), $\pi/8$ (T), and Controlled-NOT (CNOT) gates. The aforementioned set of gates can be mathematically described in the computational basis as follows:

$$Hadamard = \frac{1}{\sqrt{2}}\begin{pmatrix} 1 & 1 \\ 1 & -1 \end{pmatrix} \ , \tag{5.6}$$

$$Phase = \begin{pmatrix} 1 & 0 \\ 0 & i \end{pmatrix} \quad , \tag{5.7}$$

$$\pi/8 = \begin{pmatrix} 1 & 0 \\ 0 & e^{i\frac{\pi}{4}} \end{pmatrix} \quad . \tag{5.8}$$

The Solovay–Kitaev theorem posits that any arbitrary single-qubit gate can be effectively represented by a finite sequence drawn from the subset H, S, T. To extend this representation to multi-qubit operations, the inclusion of the CNOT gate, which interacts with two qubits, one as a control that remains unchanged, and the other as a target that is conditionally flipped, is necessary:

$$CNOT = \begin{pmatrix} 1 & 0 & 0 & 0 \\ 0 & 1 & 0 & 0 \\ 0 & 0 & 0 & 1 \\ 0 & 0 & 1 & 0 \end{pmatrix} \quad . \tag{5.9}$$

This additional gate enriches the computational capabilities, allowing for the manipulation and interaction of multiple qubits within a quantum system.

The ensemble of quantum gates produced by the H, S, and CNOT gates constitutes a set known as the Clifford group. This group is of considerable significance in the context of quantum computing, particularly for applications in quantum error correction and gate operation evaluation. However, according to the Gottesman-Knill theorem, a quantum computer that operates exclusively with Clifford gates can be efficiently emulated using a probabilistic classical computer. Therefore, to fully harness the computational superiority of quantum computing, the inclusion of a non-Clifford gate, such as the T gate, is essential.

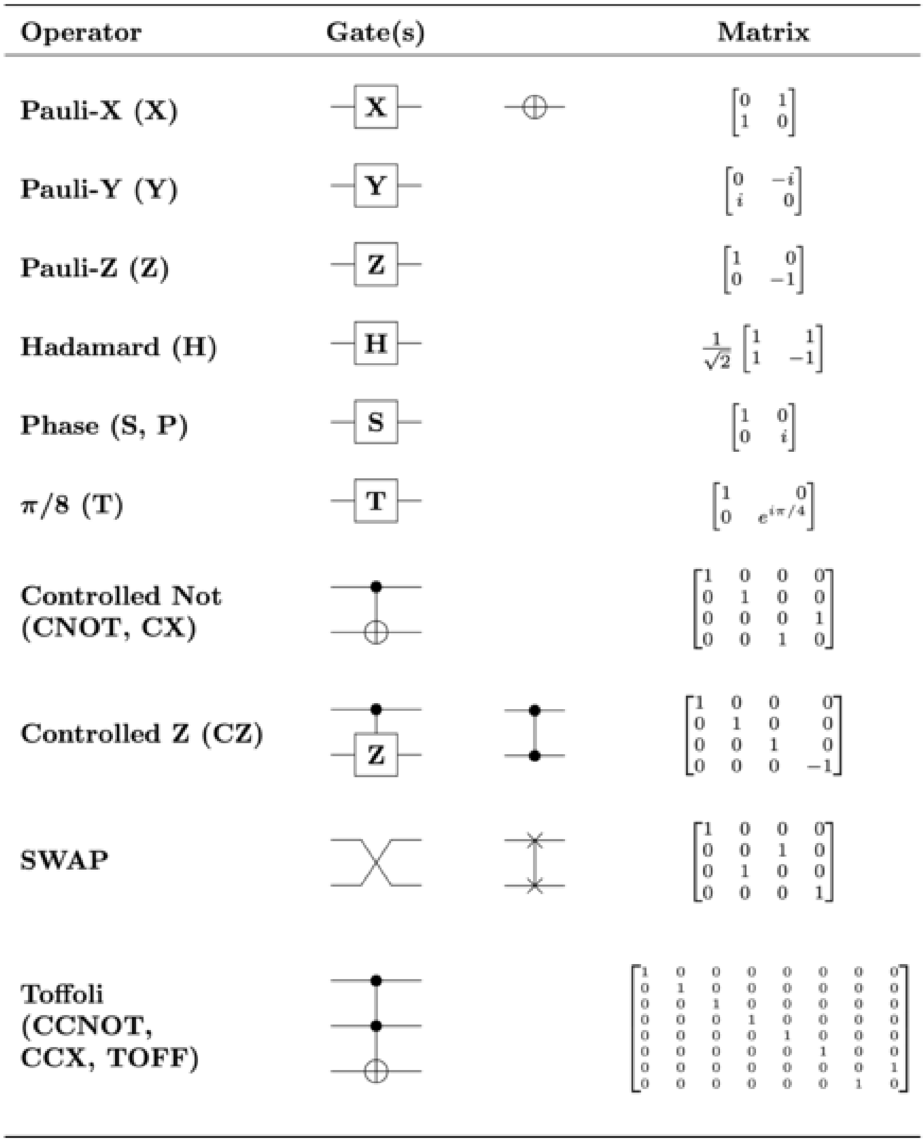

Operator	Gate(s)	Matrix
Pauli-X (X)	X	$\begin{bmatrix} 0 & 1 \\ 1 & 0 \end{bmatrix}$
Pauli-Y (Y)	Y	$\begin{bmatrix} 0 & -i \\ i & 0 \end{bmatrix}$
Pauli-Z (Z)	Z	$\begin{bmatrix} 1 & 0 \\ 0 & -1 \end{bmatrix}$
Hadamard (H)	H	$\frac{1}{\sqrt{2}}\begin{bmatrix} 1 & 1 \\ 1 & -1 \end{bmatrix}$
Phase (S, P)	S	$\begin{bmatrix} 1 & 0 \\ 0 & i \end{bmatrix}$
$\pi/8$ (T)	T	$\begin{bmatrix} 1 & 0 \\ 0 & e^{i\pi/4} \end{bmatrix}$
Controlled Not (CNOT, CX)		$\begin{bmatrix} 1 & 0 & 0 & 0 \\ 0 & 1 & 0 & 0 \\ 0 & 0 & 0 & 1 \\ 0 & 0 & 1 & 0 \end{bmatrix}$
Controlled Z (CZ)	Z	$\begin{bmatrix} 1 & 0 & 0 & 0 \\ 0 & 1 & 0 & 0 \\ 0 & 0 & 1 & 0 \\ 0 & 0 & 0 & -1 \end{bmatrix}$
SWAP		$\begin{bmatrix} 1 & 0 & 0 & 0 \\ 0 & 0 & 1 & 0 \\ 0 & 1 & 0 & 0 \\ 0 & 0 & 0 & 1 \end{bmatrix}$
Toffoli (CCNOT, CCX, TOFF)		$\begin{bmatrix} 1 & 0 & 0 & 0 & 0 & 0 & 0 & 0 \\ 0 & 1 & 0 & 0 & 0 & 0 & 0 & 0 \\ 0 & 0 & 1 & 0 & 0 & 0 & 0 & 0 \\ 0 & 0 & 0 & 1 & 0 & 0 & 0 & 0 \\ 0 & 0 & 0 & 0 & 1 & 0 & 0 & 0 \\ 0 & 0 & 0 & 0 & 0 & 1 & 0 & 0 \\ 0 & 0 & 0 & 0 & 0 & 0 & 0 & 1 \\ 0 & 0 & 0 & 0 & 0 & 0 & 1 & 0 \end{bmatrix}$

Figure 5.2: Table of the most common quantum gates, each with its associated logical symbol and corresponding matrix in the computational basis.

The development and application of quantum gates must account for the practical boundaries and restrictions presented by the quantum hardware and its controlling apparatus. This encompasses elements like the time of gate executions, the specifications of the control electronics, and the unwanted leakages of the system state outside the computational space. To counteract the constraints encountered in experimental configurations, researchers have devised methods to sculpt the control pulses, thereby enabling the generation more accurate quantum gates.

A fundamental challenge in qubit control and gate implementation is maintaining quantum coherence. Qubits are highly susceptible to decoherence, which occurs when they interact with their external environment, leading to a loss of quantum information. Effective qubit control requires isolating the qubits from external noise and disturbances, while still allowing precise manipulation through external control signals.

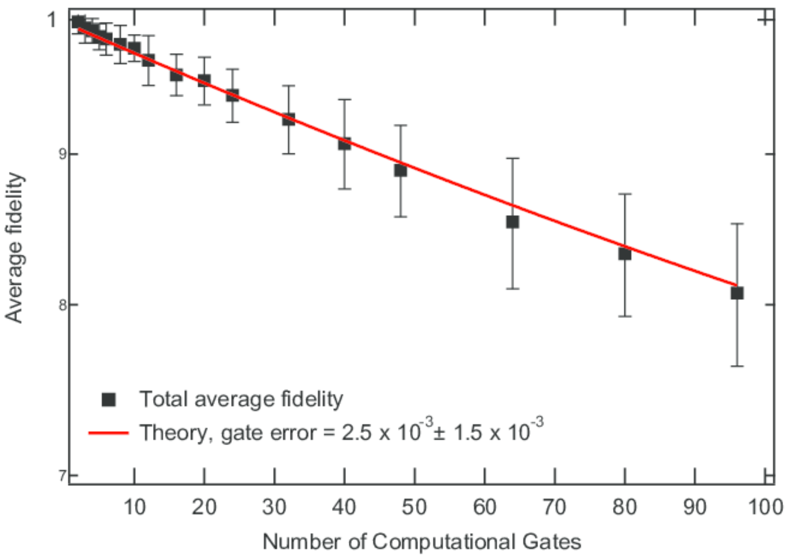

Figure 5.3: The image illustrates the decline in fidelity with an increasing number of gates implemented. Consequently, shorter gate durations are advantageous, as they enable the execution of more gates within the same time frame.

Error correction is another critical aspect of qubit control. Quantum error correction schemes are employed to detect and correct errors that occur during computation, without collapsing the quantum state. This involves encoding the quantum information in a way that allows for errors to be detected and corrected, often by using additional qubits for redundancy.

5.2 Jaynes–Cummings Hamiltonian

In order to manipulate and measure the state of a qubit, a common strategy involves leveraging its interaction with the electromagnetic field. To thoroughly examine this qubit-field interaction, this section will delve into the Jaynes-Cummings model. This model elucidates the dynamics of a two-level quantum system, equivalent to a qubit, as it interacts with a quantized mode within a resonator, or a bosonic field. This model lays the theoretical foundation essential for the development of control and readout mechanisms in Transmon qubits.

Let's consider the following Hamiltonian describing the whole system:

$$\hat{H} = \hat{H}_{\text{qubit}} + \hat{H}_{\text{field}} + \hat{H}_{\text{int}} \quad . \tag{5.10}$$

$\hat{H}_{\text{qubit}}$ and $\hat{H}_{\text{field}}$ corresponds to the qubit and electromagnetic field Hamiltonians in isolation, while the term $\hat{H}_{\text{int}}$ models their interaction. Mathematically, the qubit Hamiltonian can be defined as:

$$\hat{H}_{\text{qubit}} = \frac{\hbar\omega_q}{2}\hat{\sigma}_z \quad . \tag{5.11}$$

Here, ω_q represents the qubit transition frequency, and $\hat{\sigma}_z$ is the Pauli-z operator. The Hamiltonian of the electromagnetic field can be described as follows:"

$$\hat{H}_{\text{field}} = \hbar\omega\hat{a}^\dagger\hat{a} \ . \tag{5.12}$$

The operators $\hat{a}^\dagger$ and $\hat{a}$ are the bosonic creation and annihilation operators, and ω is the frequency of the excited mode in the electromagnetic field. Finally, the interaction between the two system is modeled as:

$$\hat{H}_{\text{int}} = \hbar g(\hat{a} + \hat{a}^\dagger)(\hat{\sigma}_+ + \hat{\sigma}_-) \ . \tag{5.13}$$

The term g corresponds to the coupling rate between the qubit and the field's mode, $\hat{\sigma}+$ and $\hat{\sigma}-$ are the qubit excitation and de-excitation operators.

In order to simplify the Hamiltonian analysis, it is convenient to move from the *Schrödinger picture* to the *interaction picture*, which is useful in dealing with changes to the wave functions and observables due to interactions. Mathematically, this corresponds to applying the following transformation:"

$$\hat{H}_{\text{ip}} = e^{i\hat{H}_0 t/\hbar}\hat{H}_{\text{int}}e^{-i\hat{H}_0 t/\hbar} \ , \tag{5.14}$$

where $\hat{H}_0 = \hat{H}_{\text{qubit}} + \hat{H}_{\text{field}}$. The Hamiltonian that we obtain has the following form:

$$\hat{H}_{\text{ip}} = \hbar g(\hat{a}\hat{\sigma}_- e^{-i(\omega+\omega_q)t} + \hat{a}^\dagger\hat{\sigma}_+ e^{i(\omega+\omega_q)t} + \hat{a}\hat{\sigma}_+ e^{i(-\omega+\omega_q)t} + \hat{a}^\dagger\hat{\sigma}_- e^{-i(-\omega+\omega_q)t}) \ . \tag{5.15}$$

Since this Hamiltonian contains fast-rotating terms, specifically those with $(\omega + \omega_q)$, we can further simplify the Hamiltonian through the *Rotating Wave Approximation.* Practically, this means removing the fast-rotating terms from the equation, resulting in:

$$\hat{H}_{\text{ip}} = \hbar g(\hat{a}\hat{\sigma}_+ e^{i(-\omega+\omega_q)t} + \hat{a}^\dagger\hat{\sigma}_- e^{-i(-\omega+\omega_q)t}) \ . \tag{5.16}$$

Transforming back into the Schrödinger picture we obtain the *Jaynes–Cummings Hamiltonian* (JCH):

$$\hat{H}_{\text{JC}} = \frac{\hbar\omega_q}{2}\hat{\sigma}_z + \hbar\omega\hat{a}^\dagger\hat{a} + \hbar g(\hat{a}\hat{\sigma}_+ + \hat{a}^\dagger\hat{\sigma}_-) \ . \tag{5.17}$$

The interaction term of the JCH can only induce system transitions from $|n+1, 0\rangle$ to $|n, 1\rangle$, where n represents the number of photons in the excited mode of the field. Considering the orthogonality of the states (i.e., $\langle n+1, 0|n, 1\rangle = 0$), we can use this basis to express the JCH in matrix form:

$$\hat{H}_{\text{JC}}^{(n)} = \begin{pmatrix} n\hbar\omega + \frac{1}{2}\hbar\omega_q & \hbar g\sqrt{n+1} \\ \hbar g\sqrt{n+1} & (n+1)\hbar\omega - \frac{1}{2}\hbar\omega_q \end{pmatrix} \ . \tag{5.18}$$

The energy eigenvalues of Equation 5.18 are given by:

$$E_{\pm}(n) = \left(n + \frac{1}{2}\right) \hbar\omega_c \pm \hbar\sqrt{\Delta^2 + 4g^2(n+1)} \ , \tag{5.19}$$

where the parameter $\Delta = \omega - \omega_q$ represents the detuning between the excited mode frequency and the qubit frequency.

To understand how the Jaynes-Cummings Hamiltonian can be engineered to control qubit transitions, we can analyze the state transitions of the system from $|n,1\rangle$ to $|n+1,0\rangle$. For this purpose, let's consider the interaction component of the JCH:

$$\hat{H}_{\text{JC-int}} = \hbar g(\hat{a}\hat{\sigma}_+ + \hat{a}^\dagger\hat{\sigma}_-) \ . \tag{5.20}$$

Going back to the interaction picture the Schrödinger equation of the system can be defined as:

$$i\hbar\frac{\partial\left|\psi(t)\right\rangle}{\partial t} = \hat{H}_{\text{JC-int}}\left|\psi(0)\right\rangle \ . \tag{5.21}$$

Since the state vector of the system can be defined as:

$$\left|\psi(t)\right\rangle = \alpha\left|n,1\right\rangle + \beta\left|n+1,0\right\rangle \ , \tag{5.22}$$

from the Schrödinger equation we obtain two differential equation:

$$\dot{\alpha} = -ig\sqrt{n+1}\cdot\beta \ , \tag{5.23}$$

$$\dot{\beta} = -ig\sqrt{n+1}\cdot\alpha \ . \tag{5.24}$$

We can combine these equations obtaining:

$$\ddot{\alpha} + g^2(n+1)\alpha = 0 \ , \tag{5.25}$$

$$\ddot{\beta} + g^2(n+1)\beta = 0 \ . \tag{5.26}$$

Solving the previous differential equations imposing as initial conditions $\alpha = 1$ and $\beta = 0$ we obtain:

$$\alpha = \cos\left(g\sqrt{n+1}\cdot t\right) \ , \tag{5.27}$$

$$\beta = -i\sin\left(g\sqrt{n+1}\cdot t\right) \ . \tag{5.28}$$

We can then write the system state function as:

$$|\psi(t)\rangle = \cos\left(g\sqrt{n+1}\cdot t\right)|n,1\rangle - i\sin\left(g\sqrt{n+1}\cdot t\right)|n+1,0\rangle \ , \tag{5.29}$$

In the following section, we will demonstrate how to engineer the Jaynes-Cummings Hamiltonian to implement the desired quantum evolution.

5.3 Rabi Oscillation

Transmon qubit control is typically achieved through Rabi oscillations [31]. These oscillations represent the coherent exchange of energy between the computational levels of the qubit in response to an external oscillating field, which, in the case of Transmon qubits, is an electromagnetic microwave pulse.

As observed from the time evolution of the state vector $|\psi(t)\rangle$, the qubit undergoes oscillations between its ground and excited states. These dynamics are known as *Rabi oscillations*, characterized by the *Rabi frequency.* This frequency is directly proportional to both the strength of the driving field mode and the coupling rate between the qubit and the field mode. By meticulously adjusting amplitude, duration and phase of the microwave pulse, it is possible to precisely manipulate the qubit's state vector, dictating its rotation angle on the Bloch sphere.

The ability to perform such rotations with high precision is fundamental for quantum gate operations. For example, a π pulse, which corresponds to a Rabi pulse that induces a rotation of π radians, can flip the qubit from its ground state to excited state or vice versa. Similarly, a $\pi/2$ pulse can be used to place the qubit in a superposition of states, forming the basis of a Hadamard gate.

The Hadamard gate is a single-qubit operation that maps the basis states $|0\rangle$ and $|1\rangle$ to superpositions of these states, with equal amplitudes and a relative phase. Mathematically, the Hadamard gate can be represented as:

$$H = \frac{1}{\sqrt{2}}\begin{pmatrix}1 & 1\\ 1 & -1\end{pmatrix} \ . \tag{5.30}$$

For a qubit initially in the state $|0\rangle$, the application of a pulse at the Rabi frequency Ω for a time duration τ results in the state evolution described by:

$$|\psi(\tau)\rangle = \cos\left(\Omega\tau\right)|0\rangle - i\sin\left(\Omega\tau\right)|1\rangle \ . \tag{5.31}$$

To realize the Hadamard gate, we need to set the pulse duration τ such that the qubit is rotated to a superposition of the $|0\rangle$ and $|1\rangle$ states with equal probabilities. This condition is met when $\Omega\tau = \pi/2$, leading to:

$$|\psi(\tau)\rangle = \frac{1}{\sqrt{2}}(|0\rangle - i\,|1\rangle) \ . \tag{5.32}$$

However, this state is not exactly the same as the one produced by the Hadamard gate, which has real coefficients. To address this, we can introduce a phase shift ϕ in the driving field to align the phases properly. By adjusting the phase of the driving field by $\pi/2$, the final state becomes:

$$|\psi(\tau)\rangle = \frac{1}{\sqrt{2}}(|0\rangle + |1\rangle) \ , \tag{5.33}$$

which is the desired output of the Hadamard gate applied to the state $|0\rangle$. A similar approach can be used to apply the Hadamard gate to the state $|1\rangle$, and by extension, to any superposition of $|0\rangle$ and $|1\rangle$.

The Rabi model not only provides a framework for single-qubit gates but also lays the groundwork for more complex, multi-qubit gate operations. By entangling qubits through their mutual interactions and employing Rabi oscillations, one can achieve controlled-NOT (CNOT) and other two-qubit gates which are essential for universal quantum computing.

However, it is important to note that in the theoretical treatment of quantum control, especially when discussing Rabi oscillations and gate implementation, it is common to idealize the hardware qubit as a perfect two-level system. This simplification allows for a clearer understanding of the basic principles of qubit manipulation.

This idealization does not fully encapsulate the complexities inherent in actual qubit hardware. In reality, superconducting qubits, like the Transmon, have additional energy levels beyond the computational basis states. These higher, non-computational energy levels play a significant role in the dynamics of the qubit, particularly in the context of quantum computation.

The presence of non-computational energy levels in a physical qubit introduces a potential source of error in quantum computations. During gate operations, there is a risk that the qubit might inadvertently transition to these higher energy states, a phenomenon known as leakage. This leakage can lead to computational errors as the qubit's state no longer remains confined within the designated computational subspace.

The control of qubits, therefore, must be executed with precision to avoid or minimize excitation to these non-computational states. This necessitates advanced control techniques and meticulous pulse engineering. The pulses must be designed not only to implement the desired quantum gates but also to ensure that the qubit remains within the computational subspace, avoiding leakage to higher energy levels.

5.4 Derivative Removal by Adiabatic Gate

In this section, we explore the Derivative Removal by Adiabatic Gate (DRAG) technique [32], an indispensable strategy in the field of quantum computing. The essence of DRAG centers on its capacity to precisely define control pulses for quantum gates, thereby minimizing errors and avoiding leakages outside the computational space.

A critical aspect of this approach is the meticulous control of the pulse bandwidth to ensure that spectral components near the system's anharmonicity are suppressed as much as possible. This suppression is vital for reducing non-adiabatic transitions that occur during the rapid switching of quantum gates, which are a principal source of inaccuracies in quantum computations. By employing the DRAG technique, we can significantly enhance the fidelity of qubit manipulations, a crucial step towards the development of more accurate and reliable quantum computing systems.

Let's consider an example of a Gaussian control pulse lasting tens of nanoseconds with a bandwidth in the order of 100 MHz, a value comparable with a typical Transom qubit anharmonicity. A pulse possessing such bandwidth tends to induce transitions not merely between the states $|0\rangle$ and $|1\rangle$, but also between $|1\rangle$ and $|2\rangle$, leading to the undesired leakage of information out of the computational subspace. An evolved solution to mitigate this problem is the implementation of the Derivative Removal by Adiabatic Gate pulse.

To illustrate the principle of DRAG, let us consider a single qubit driven by the following Hamiltonian, formulated under the Rotating Wave Approximation:

$$\hat{H}_{\text{drive}}^{\text{RWA}} = \hbar\Omega_x(t)\left(\frac{\hat{\sigma}_x}{2}\right) + \hbar\Omega_y(t)\left(\frac{\hat{\sigma}_y}{2}\right) \quad , \tag{5.34}$$

Here, Ω_x and Ω_y represent the amplitudes for rotation about the x-axis and y-axis, respectively. In the context of a qubit with an anharmonicity denoted by α, the condition for implementing DRAG is provided by:

$$\Omega_y(t) = -\frac{\dot{\Omega}_x(t)}{\alpha} \quad . \tag{5.35}$$

This implies that the imaginary component of the control pulse maintains a proportional relationship to the derivative of its real component. Within the frequency domain, the act of taking the derivative leads to a pronounced suppression at a specific frequency, and the coefficient $-\frac{1}{\alpha}$ allows to target the frequency suppression with the transition frequency between $|1\rangle$ and $|2\rangle$.

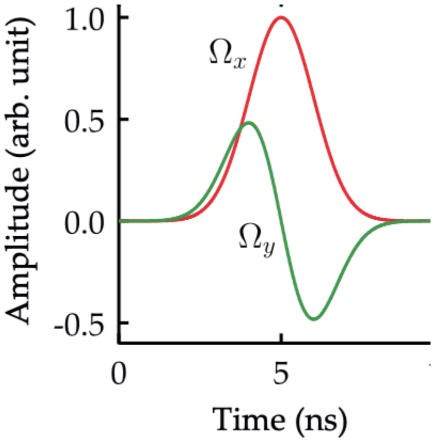

Figure 5.4: The image shows the in-phase and quadrature components of a typical DRAG pulse.

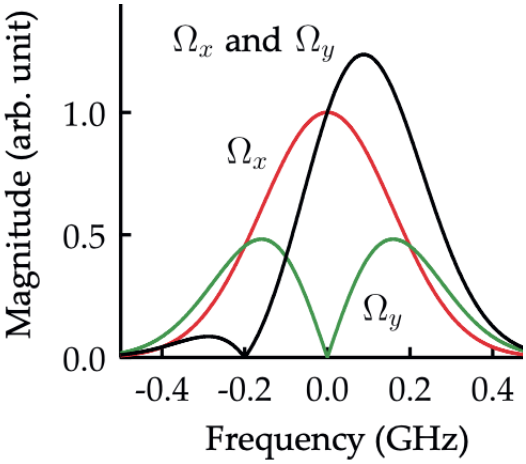

Figure 5.5: The image demonstrates the cancellation of the 200 MHz frequency, a value closely aligning with the typical anharmonicities of Transmon qubits. The black line shows the resulting spectrum magnitude.

An especially notable feature of the DRAG technique is its versatility. Although initially demonstrated using a Gaussian envelope, it can be effectively applied to various other pulse shapes. Additionally, its computation and implementation are relatively straightforward, enhancing its appeal for practical applications.

5.5 Optimal Control Techniques Fundamentals

The field of quantum computing has witnessed significant advancements in the optimal control of qubits [33], driven by the need to enhance precision, efficiency, and scalability in quantum computations. This section explores the recent innovations and techniques that have marked progress in the realm of qubit optimal control, reflecting the ongoing efforts to overcome the challenges inherent in manipulating quantum states.

To further elucidate the implementation of optimal control, it is instructive to analyze a generic Hamiltonian that characterizes a closed quantum system:

$$\hat{H}(t) = \hat{H}_0^{\text{drift}} + \sum_{j=1}^{N} \Gamma(t)_j \cdot \hat{H}_j^{\text{control}} \quad , \tag{5.36}$$

The Hamiltonian of the system can be conceptually divided into two distinct parts. The first is the drift component, which delineates the system's dynamics in the absence of external influences. The second encompasses all the control terms, each corresponding to a potential control parameter that can be employed to modify the system's dynamics. Within the realm of superconducting circuits, these control parameters are typically linked to electromagnetic pulses.

In order to find the desired parameters it is mandatory to define a cost function that spawns our control space. The optimization goal is to find the global minima (or maxima) of the function, thus controlling the dynamic with the maximum precision possible. Here below is one of the most common cost function used, the *quantum gate infidelity*:

$$I(\hat{U}_{\text{target}}, \hat{U}) = 1 - \frac{1}{\dim^2} \left| \text{Tr}(\hat{U}^{\dagger}_{\text{target}} \hat{U}) \right|^2 \quad . \tag{5.37}$$

The role of the cost function is to define how close to the target dynamic $\hat{U}_{\text{target}}$ is to the dynamic implemented using the optimal control optimization $\hat{U}$. As shown in Chapter 2 the dynamic of the system (i.e. its time evolution operator) is directly linked to its Hamiltonian through the following relationship:

$$\hat{U}(t) = e^{-\frac{i}{\hbar}\hat{H}(t)t} \quad . \tag{5.38}$$

To summarize, the objective of quantum optimal control is to delineate control parameters that steer quantum dynamical processes along a desired trajectory, thereby achieving congruence with a pre-established target dynamic. Within the domain of quantum computation, this translates to the precise implementation of quantum gates, which is pivotal for the execution of coherent and high-fidelity quantum algorithms.

A multitude of optimization algorithms are available to determine the parameters corresponding to a minimum, ideally pinpointing a global minimum. These algorithms can be classified into two principal categories: those based on gradients and those which do not rely on gradient information.

The gradient-based algorithms typically benefit from requiring fewer iterations to converge to a minimum; however, the computation of gradients can become prohibitively complex as the number of control parameters increases. Algorithms such as GRAPE and Krotov fall within this category and have been successfully employed in the control of quantum systems. On the contrary, non-gradient based algorithms are often less computationally demanding, yet they tend to necessitate a greater number of iterations to achieve convergence, resulting in a slower process.

The Chopped Random Basis (CRAB) algorithm is one such technique. It has been effectively applied to the control of quantum systems, although its application to Transmon qubits has not been explored. Throughout my doctoral research, I have been deeply intrigued by the potential of CRAB's non-gradient nature as a distinctive feature that could enable the scaling of this optimization method for QPUs with multiple qubits. Initially, I explored this possibility through numerical simulations [1]; subsequently, collaboration with Chalmers University of Technology presented me the opportunity to test this approach on their quantum hardware. I will provide a detailed exposition of this subject in the last section of this chapter.

Machine learning and artificial intelligence have also found applications in the optimal control of qubits. These technologies are employed to automate the design of control pulses and to optimize quantum gate sequences. Machine learning algorithms can learn from experimental data, adapt to changing conditions in the quantum system, and predict the most effective control strategies.

The integration of optimal control techniques with quantum error correction protocols has also been a significant focus. As quantum systems scale up, the need for effective error correction becomes paramount. Advances in control techniques have enabled the implementation of more sophisticated error correction codes, which are essential for preserving quantum information over longer durations and for more complex computations.

5.6 Chopped Random Basis

The Chopped Random Basis (CRAB) optimization algorithm, introduced in 2011 by Tommaso Caneva, Tommaso Calarco, and Simone Montangero, stands as one of the most recent and effective algorithms for optimizing quantum systems [34, 35]. This algorithm adopts a non-gradient-based approach to optimal control, utilizing a *direct search method*. From a computational standpoint, this approach requires significantly less numerical effort compared to gradient-based algorithms.

Choosing to employ the CRAB algorithm (and generally non-gradient-based algorithms) proves effective in optimizing quantum systems in cases where the calculation of propagators is relatively straightforward (i.e., systems whose associated Hilbert spaces have low dimensionality), for systems with a limited number of control parameters, or when the cost function does not allow gradient calculation. For the study of systems composed of relatively few qubits, this type of approach can be an efficient method for seeking optimal control, given the low dimensionality of the total system.

The essence of the CRAB algorithm lies in selecting optimization parameters based on a physically motivated function basis that constructs control signals. An example of such a basis is a limited Fourier expansion.

The algorithm then proceeds to optimize the coefficients of the basis. This method has proven to be quite effective, especially when control pulses consist of simple signals, and the number of control parameters defined by this algorithm is less than the number of steps in the control pulse. Furthermore, the algorithm's authors have demonstrated that randomizing the basis expedites its convergence. In the specific example of targeting a Fourier expansion, this translates to randomizing the frequency basis, which results in the loss of orthonormality.

This algorithm can also easily integrate experimental constraints such as function smoothness, known solutions within the system's pulses, and a physically meaningful initial guess that can greatly speed up its convergence.

Typically, the *Nelder-Mead simplex algorithm* [36] is used for the actual optimization of the control parameters defined by CRAB. Introduced in 1965 by John Nelder and Roger Mead, the Nelder-Mead simplex algorithm (or simplex method) is a numerical method used for finding the minimum or maximum of a given cost function, where the control parameters form a multidimensional space. It is a direct search method based on comparing the cost function's value.

For instance, in an n-dimensional control space, the algorithm manages the exploration of the control landscape in the form of a simplex (a generalization of the notion of triangle or tetrahedron in n dimensions) formed by n+1 test points of the cost function. Correctly defining the initial simplex is crucial for the algorithm's proper functioning. An initially too small simplex can locally trap the search, hence the necessity to define a simplex appropriate to the topological and geometric characteristics of the control landscape for the optimization problem at hand.

Once the first simplex is correctly defined, the algorithm calculates the control function's value at the test points. The goal is to find a new test point and replace one of the old points with the new one, adopting this approach iteratively.

The simplest technique replaces the point with the worst cost function performance with the centroid (or barycenter) obtained from the arithmetic means of all control parameters related to the other n test points of the simplex. If the point defined by the centroid performs better than the best of the tested points, the algorithm may attempt to extend the simplex in that direction. Otherwise, if the new point does not provide significantly better performance than the point slated for replacement, indicating a valley (or minimum), the algorithm can attempt to extend the simplex in search of a better point (to avoid getting stuck in local minima).

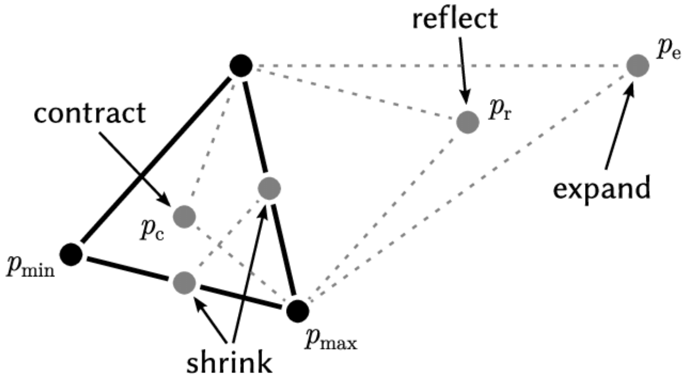

Figure 5.6: An iteration of the Nelder-Mead method over a two-dimensional space.

The CRAB algorithm, when applied with Fourier expansion, proposes for each control parameter of the Hamiltonian a pulse. The optimization process then involves the algorithm searching for the most effective correction to this pulse, represented as follows:

$$\Gamma(t)_j^{CRAB} = \Gamma(t)_j^0 * G_j(t) \ . \tag{5.39}$$

The functions $G_j(t)$ are expressed by a limited number of components N_c, corresponding to the adopted random basis, with random amplitude and frequency:

$$G_j = \sum_{k=1}^{N_c} c_j^k g_j^k(\omega_j^k t) \ . \tag{5.40}$$

The terms $g_j^k(\omega_j^k t)$ represent the basis functions that allow for the expansion of G_j into a Fourier series through the coefficients c_j^k. The parameters ω_j^k are thus angular frequencies. In the implementation of the CRAB algorithm used in this thesis work, the functions g_j^k correspond to sinusoidal or cosinusoidal functions. By using a limited number of components ($k = 1...N_c$), the computational cost remains relatively low. The randomization of the basis functions is achieved through the following approach:

$$g_j^k \rightarrow g_j^k(\omega_j^k(1 + r_j^k)t) \ . \tag{5.41}$$

The terms r_j^k are random numbers responsible for the randomization of the basis functions. Once the basis functions are randomized, the optimization problem is reformulated as the search for coefficients c_j^k that can minimize the cost function defined for the system. As previously explained, the coefficients c_j^k can be determined through direct optimization algorithms.

5.7 Case Study: Transmon Qubit Optimal Control at Chalmers

The quantum computing research group at Chalmers University has achieved significant progress in superconducting QPU design and control, establishing themselves as a leading force in both European and global quantum computing research. This section presents a focused study on the qubit control strategies that I developed with Chalmers QTL, highlighting the innovative approaches and significant findings that have emerged from the research.

The key topic of our joint effort has been the development of advanced pulse shaping techniques in order to implement fast and accurate quantum gates. These techniques involve the customization of the waveform of control pulses to maximize their effectiveness in manipulating qubit states. By finely tuning the amplitude, phase, and frequency components of the pulses, we can significantly reduce errors and enhance the precision of quantum gate operations. This meticulous adjustment, guided by the principles of optimal control theory, optimizes the development and implementation of qubit gates. Such optimization is crucial for creating more reliable and efficient quantum computing architectures.

The initial stride in applying quantum optimal control techniques involved employing the an optimization algorithm based on the Chopper Random Basis method. The motivation behind this decision was that numerical simulation of the application of this optimization technique on Transmon qubit showed very promising results, a topic that I extensively studied during my first year of PhD [1].

The algorithm I crafted was utilized to shape the in-phase and quadrature electromagnetic pulses responsible for executing single-qubit gates. The primary objective was to surpass the fidelity achieved by single-qubit gates implemented using Derivative Removal by Adiabatic Gate pulses.

The Hamiltonian used to characterize the single Transmon qubit designed at Chalmers in the Rotating Wave Approximation (RWA) [37] is delineated as follows:

$$\hat{H}_{\mathrm{RWA}} = \frac{\eta}{2}\hat{n}(\hat{n}-1) + if(t)(\hat{a}-\hat{a}^{\dagger}) + q(t)(\hat{a}+\hat{a}^{\dagger}) \ . \tag{5.42}$$

The control parameters $f(t)$ and $q(t)$ correspond to the in-phase and quadrature components, respectively, of the envelope generator's signal. This signal is subsequently upconverted to the qubit's operational frequency by means of a mixing process. The adoption of the Rotating Wave Approximation and the alignment of the control signal's carrier frequency with that of the qubit enable the use of the RWA simplified Hamiltonian, and treat $f(t)$ and $q(t)$ as optimization parameters.

For the efficient execution of optimization, it is imperative to define a cost function that is both straightforward and rapid to compute, while simultaneously maintaining accuracy. Achieving this balance is a complex task, as these two requirements often stand in opposition to each other. To accurately estimate the state of the qubit, multiple experimental iterations are required to statistically infer its state with precision. Typically, a greater number of experimental repetitions enhances accuracy, yet this incrementally increases the time required for completion. Therefore, it is crucial to establish an equilibrium between the demands for accuracy and time efficiency in the optimization process.

When the fluctuations in the cost function values are predominantly a result of inherent uncertainties in the measurement process, rather than being reflective of genuine alterations in the system's state or control parameters, it becomes exceedingly challenging to optimize these parameters effectively. The difficulty lies in distinguishing between variations caused by measurement noise and those arising from actual system changes, rendering the optimization process practically infeasible.

An additional critical aspect that emerged as pivotal in our optimization endeavors was the establishment of a significant initial guess. Initially, we embarked on the optimization from a random starting point, an approach that proved markedly inefficient. Our CRAB-based optimization routine frequently became lost in the pursuit of a minimum, leading to impractically prolonged optimization times. To address this issue, we shifted our strategy to commence the optimization with DRAG-shaped pulses for the in-phase and quadrature components, constructed with underlying CRAB-like structures. This adjustment markedly enhanced the effectiveness of our optimization process. From a mathematical perspective, the following equations describe the control parameters utilized for the in-phase component:

$$f(t) = \Gamma_f(t) \cdot \left(\sum_{k=1}^{2} c_k \cdot \sin_k(\omega_k t) + \sum_{l=1}^{2} c_l \cdot \cos_l(\omega_l t) \right) \quad . \tag{5.43}$$

The following equations describe the control parameters utilized for the quadrature component:

$$q(t) = \Gamma_q(t) \cdot \left(\sum_{j=1}^{2} c_j \cdot \sin_j(\omega_j t) + \sum_{n=1}^{2} c_n \cdot \cos_n(\omega_n t) \right) \quad . \tag{5.44}$$

In the context of the in-phase equation, $\Gamma_f(t)$ represents a Gaussian envelope. However, unlike in the DRAG approach, the quadrature equation's envelope, $\Gamma_q(t)$, is identical to $\Gamma_f(t)$ and not its time derivative scaled by a specific coefficient. The rationale behind this deviation from the DRAG methodology will be explained later in this section.

To determine the appropriate DRAG-like initial pulse shapes, we embraced an empirical approach. This process commenced with the calibration of the most efficient DRAG pulses, which served as our benchmark. Subsequently, we crafted the in-phase and quadrature components to closely mirror the contours of this DRAG reference. We shaped both the envelopes and the underlying structure, with an emphasis on minimizing the number of control parameters. This strategy was based on the observation that not all parameters significantly contributed to the optimization process. Redundant parameters tend to complicate the control space, thereby prolonging the optimization time. Given that our methodology hinged on a non-gradient-based optimization technique, the judicious pruning of parameters emerged as a crucial factor in shortening the optimization times.

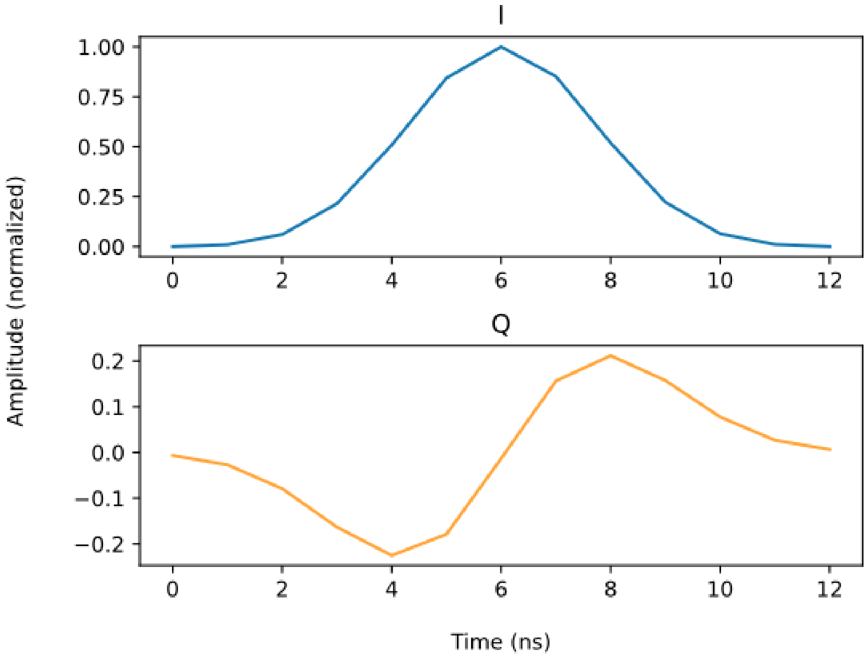

Figure 5.7: This image illustrates pulses designed in the DRAG style, further enhanced with a CRAB-based underlying framework.

The reference DRAG pulses utilized by Chalmers had a duration of 20 ns. Aiming to enhance efficiency, we sought to reduce this duration and thus opted to optimize pulses with durations of 8 and 12 ns, both values above the *quantum speed limit* [38]. This decision was a critical aspect of our study, as shorter pulses inherently lead to greater accuracy. This is attributed to the reduced time available for the qubit to undergo decay or experience decoherence. Furthermore, the adoption of shorter pulses also facilitates the execution of more complex algorithms within the same temporal window, a significant advantage in the realm of quantum computing.

For the actual generation of the control pulses, we employed QBLOX control electronics. A primary constraint of this hardware stemmed from its design, wherein pulses are delineated in 1 ns time steps. This specification inherently restricts the attainable smoothness of the pulses, a limitation that becomes particularly pronounced with shorter pulse durations. Nevertheless, this hardware limitation did not impede the optimization process.

The QBLOX hardware used process control pulses in 4 ns blocks, so every pulse must have a duration that is a multiple integer of this minimum duration. Although pulse durations as low as 4 ns are theoretically achievable, we were unable to test these shorter durations. To drive the same gate with a shorter pulse requires a carrier with greater power. Unfortunately, the carrier we used was incapable of delivering such power, thus limiting us to a minimum pulse duration of 8 ns.

Presented below is a schematic depiction of the entire experimental system:

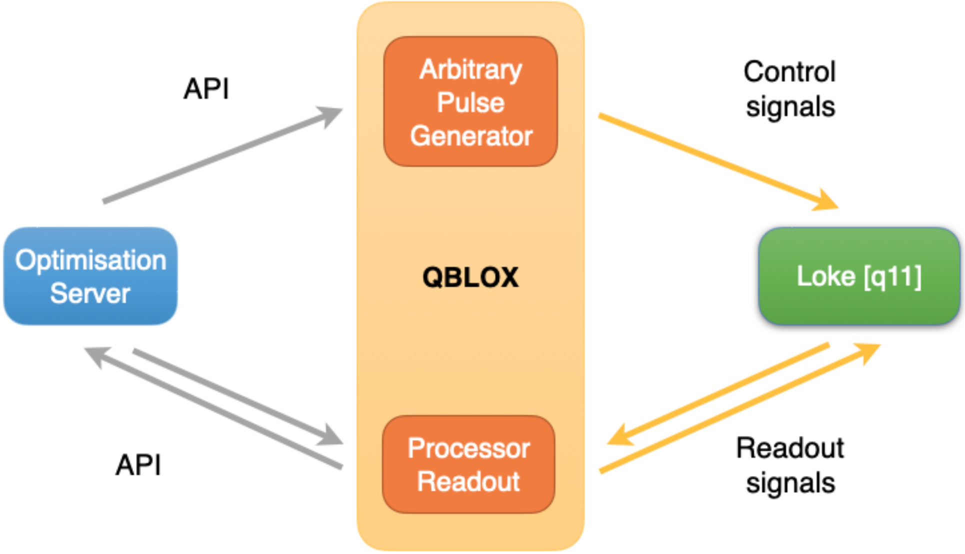

Figure 5.8: Block diagram of the experimental setup: "Loke" refers to the Quantum Processing Unit, and "q11" denotes the target qubit in the system.

An exhaustive trial-and-error approach was employed to ascertain the appropriate number of basis functions. This rigorous exploration led to the determination of $N_c = 2$ as the optimal value, striking a balance between achieving the desired accuracy and avoiding the unnecessary optimization of redundant parameters. Thus, $N_c = 2$ assumed two sinusoidal and two cosinusoidal bases for the in-phase and quadrature components, respectively.

The optimization process involved determining the optimal control parameters, specifically the frequencies of the basis functions, their associated coefficients, and the sigma values of the Gaussian envelopes.

Nonetheless, incorporating the basis frequencies and the sigma of the Gaussian envelope into the optimization process proved to be advantageous for achieving precise optimizations, though it was not deemed essential. Indeed, it was observed that with proper tuning of these parameters, satisfactory optimization results could still be attained even while keeping them fixed. This finding highlights the flexibility of the optimization strategy, allowing for effective adjustments even under fixed-parameter conditions.

In constructing the in-phase pulse, we initially activated only the base frequency cosine component. This component's frequency was calibrated to achieve a period that is half the duration of the pulse, and it was then combined with a simple Gaussian envelope. For the quadrature component, we activated only the first harmonic sinusoidal component, aligning its period with the duration of the pulse, and subsequently weighting it with the same Gaussian envelope as the in-phase component. Then, we multiplied the result by a meticulously selected coefficient to implement the unwanted frequency cancellation as in the DRAG technique. This approach effectively emulated a DRAG pulse. In particular, the in-phase component closely resembled a Gaussian envelope, while the quadrature component, created by multiplying a sine function with a Gaussian envelope and a DRAG-enabling coefficient, effectively simulated the weighted derivative of the Gaussian envelope as employed in the DRAG method.

During the course of my experimental work, I observed that excessive randomization of the basis frequencies posed a significant issue. It tended to excessively distort the pulse shape, rendering it markedly different from the benchmark DRAG pulse. This distortion often resulted in asymmetries and abrupt discontinuities at the beginning and/or end of the pulse, leading to undesirable steps. Ensuring a smooth transition at both the initial and final stages of the control function is crucial to prevent the introduction of frequencies that might induce transitions outside the computational space. In this context, a modest degree of frequency randomization was found to be sufficient.

For the actual optimization algorithm we opted for the Nelder-Mead direct search method, a non-gradient-based approach. This decision was taken on the understanding that, although this method exhibits slower convergence, it possesses scalability to multi-qubit systems and generally demands less computational intensity compared to gradient-based methods. Our experience with the Nelder-Mead search method revealed a propensity for becoming stuck in local minima. Consequently, the adoption of a meaningful initial guess proved instrumental in achieving successful optimizations. Even with this strategy, it remains uncertain whether the optimization reached a global minimum, although it was adequate for fulfilling our optimization objectives. Additionally, the presence of fluctuations in the cost function further complicated the analysis of the control space. As previously discussed, striking a balance between the accuracy of the cost function and the expediency of its evaluation is essential for efficient and precise optimization.

The intricate task of defining an appropriate cost function constituted the most tough challenge in this research. The constraints associated with experimental systems, particularly the time required for each step of measurement, computation, and interaction between the measured system and the measurement apparatus, posed significant challenges. After several attempts, we chose to utilize the All XY analysis as our cost function [39]. The All XY analysis is exceptionally adept at evaluating X π rotations (i.e. π rotation around the x-axes of the Majorana-Bloch sphere), Y π rotations (i.e. π rotation around the y-axes of the Majorana-Bloch sphere), X $\pi/2$ rotations, and Y $\pi/2$ rotations. This method comprehensively tests all possible two-gate combinations from the aforementioned gate set, along with the Identity gate, and measures the qubit population for each combination. These measurements are then compared against the ideal scenario. From this benchmarking process, the mean standard deviation is calculated, which serves as the cost function for our optimization algorithm to minimize.

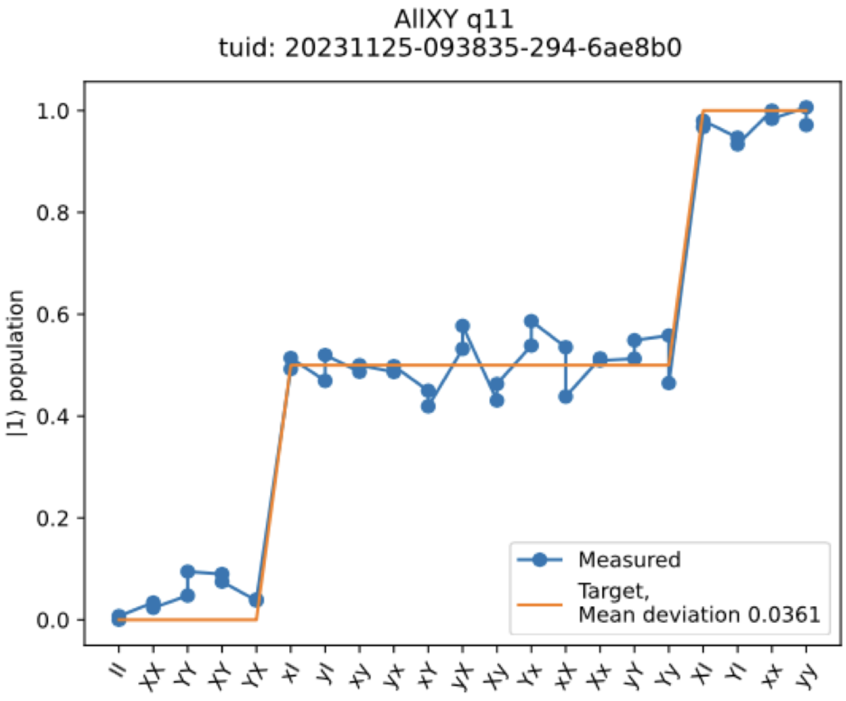

Figure 5.9: Example of an All XY measurement: The orange line represents the target population in the $|1\rangle$ quantum state. The blue line shows the actual measured population in comparison.

For the optimization of both the 8 and 12 ns pulses, our specific goal was to ensure that the mean standard deviation in the All XY analysis remained lower than that of the DRAG pulses, which were utilized in formulating our initial pulse guess. This objective was set with the intention of achieving a more precise implementation of the All XY analysis gate compared to the precision attainable with a standard DRAG pulse.

Numerous optimization trials were conducted, yielding successful outcomes. As an example, the mean standard deviation goal set by the benchmark DRAG pulses was established at 0.49. In comparison, the mean standard deviation achieved with our optimized pulses was 0.23, a significantly lower figure. In this particular instance, the algorithm required 205 iterations to identify the optimal control parameters, which equated to approximately 50 minutes of optimization time. The results obtained from other optimization attempts were consistently similar, thereby affirmatively validating the effectiveness of our algorithm.

Chapter 6

Measuring the Quantum Processing Unit

In the realm of quantum computing, measurement plays a pivotal role, serving as the bridge between the quantum and classical worlds. This chapter delves into the intricacies of measurement techniques in quantum computing, offering insights into both the methodologies employed and the challenges encountered in accurately measuring quantum states.

Measurement in quantum computing is fundamentally different from classical measurement. In a classical system, measurement can be performed without significantly disturbing the system [40]. However, in a quantum system, measurement has a profound impact on the state being measured due to the quantum mechanical principle of wave function collapse. This principle states that measuring a quantum state forces it into one of the eigenstates of the measurement basis, thereby altering the original quantum state.

The focus of the chapter is on the quantum non-demolition techniques used for measuring the state of Transmon qubits. The challenges associated with quantum measurement are also examined in detail. One of the primary challenges is quantum decoherence, where interaction with the environment causes the loss of quantum information before the measurement can be completed.

6.1 Dispersive Readout Method

Readout of Transmon qubits, involves specialized techniques to accurately determine their quantum states. This section introduces the primary method of readout in superconducting qubits, focusing on the prevalent *dispersive readout* technique.

Dispersive readout effectively gather the qubit's quantum state through its entanglement with a superconducting resonator that act as probe. In this regime the qubit causes a shift in the resonator's frequency, dependent on the qubit's state. This shift enables the deduction of the qubit state by examining the resonator. However, being a measurement is important to not be meslead thinking that the qubit do not collapse in a eigenstate upon measurement. In fact, despite the indirect probing of the qubit, as soon as, the measurement signal interacts with the resonator the qubit state collapse since those structures are entangled.

In this context, optimizing readout efficacy translates to maximizing the signal-to-noise ratio of the microwave signal sent to the resonator while minimizing any undesired impact on the qubit, known as *back-action.* The interaction between the qubit and resonator is governed by the Jaynes–Cummings Hamiltonian:

$$H_{JC} = \omega_r \left(\hat{a}^\dagger \hat{a} + \frac{1}{2} \right) + \frac{\omega_q}{2} \hat{\sigma}_z + g(\hat{\sigma}_+ \hat{a} + \hat{\sigma}_- \hat{a}^\dagger) \ . \tag{6.1}$$

In this context, ω_r and ω_q denote the frequencies of the resonator and the qubit, respectively. All other parameters are as defined in the section dedicated to the Jaynes–Cummings Hamiltonian in Chapter 5. However, in contrast to the formulation presented in that chapter, this version sets the *reduced Planck constant* $\hbar$ to 1 and also accounts for the half-photon term, which establishes the ground energy level for the resonator. This half-photon term was omitted in the earlier formulation for simplicity. Employing such simplifications is a common mathematical practice among physicists to streamline equations.

In the dispersive regime, characterized by the qubit's detuning from the resonator frequency far exceeding their coupling rate g and the resonator's linewidth κ, such that $\Delta = |\omega_q - \omega_r| \gg g, \kappa$, the energy exchange between the two systems is effectively suppressed. Under these conditions, the qubit and resonator frequency shift in response to each other's presence. By employing second-order perturbation theory with respect to the ratio g/Δ and considering a resonator photon population in the low-excitation limit, we can derive an approximate form of the Hamiltonian known as the *dispersive Hamiltonian*:

$$H_{\text{disp}} = (\omega_r + \chi \hat{\sigma}_z) \left(\hat{a}^\dagger \hat{a} + \frac{1}{2} \right) + \frac{\tilde{\omega}_q}{2} \hat{\sigma}_z \ , \tag{6.2}$$

The parameter $\chi = \frac{g^2}{\Delta}$ denotes the qubit-dependent frequency modification, termed as the *dispersive shift*. This shift enables the differentiation between the qubit's two distinct states. Additionally, the resonator's vacuum fluctuations, due to its half-photon ground energy, induce a modification in the qubit frequency. This phenomenon is referred as the *Lamb shift*, resulting in an adjusted qubit frequency given by $\tilde{\omega}_q = \omega_q + \frac{g^2}{\Delta}$.

In the regime where the resonator harbors a limited number of photons, the Hamiltonian, as delineated in Equation 6.2, commutes with $\hat{\sigma}_z$ (i.e. the qubit observable), thereby enabling a Quantum Non-Demolition (QND) measurement. However, should the resonator's photon count operator, denoted by $\hat{n} = \hat{a}^\dagger \hat{a}$, surpass the designated critical photon number $n_c = \frac{\Delta^2}{4g^2}$, the previously stipulated dispersive Hamiltonian ceases to provide an accurate representation. Consequently, n_c delineates the threshold for the probe signal's power within the resonator to ensure the retention of a QND measurement.

The dispersive interaction between the qubit and the resonator can be conceptualized from an alternative perspective. By rearranging the terms in Equation 6.2, we obtain a mathematically equivalent expression:

$$\hat{H}_{\text{disp}} = \omega_r \left(\hat{a}^\dagger \hat{a} + \frac{1}{2} \right) + \frac{1}{2} \left(\omega_q + \frac{g^2}{\Delta} \hat{\sigma}_z + \frac{2g^2}{\Delta} \hat{a}^\dagger \hat{a} \right) \hat{\sigma}_z \ . \tag{6.3}$$

As in the previous equation form the term $\frac{g^2}{\Delta}$ is called Lamb Shift and represents the qubit frequency shift induced by resonator's vacuum fluctuations. While the term $\frac{2g^2}{\Delta} \hat{a}^\dagger \hat{a}$

called *ac-Stark shift* accounts for the frequency shift induced by the amount of photons populating the resonator. This phenomenon may inadvertently shift the qubit from its intended rotational frame, leading to a loss of coherence. Therefore, the presence of unintended photons, whether from thermal sources or coherent states, can modify the qubit's frequency and induce dephasing. To mitigate this, careful thermal management of the QPU and meticulous filtering and attenuation of control lines are essential to reduce photon number fluctuations.

6.2 Resonator Probing

In the preceding section, we delved into the mechanics of the dispersive readout method, understanding that the resonator's frequency is modulated depending on the state of the qubit. Our current exploration shifts to the methodology of probing the resonator, a process integral to measuring the qubit state. This involves differentiating between the two classical signatures that the resonator exhibits in response to the qubit's distinct eigenstates.

The differentiation of the qubit states is achieved by enhancing the separation of these states on the (I, Q)-plane—that is, the in-phase and quadrature components of reflected probe signal sent by the readout pulse generator. Theoretical analyses reveal that this state separation reaches its peak when the resonator interrogation occurs at the midpoint between the resonance frequencies associated to the qubit eigenstates, denoted by $\omega = \frac{\omega_{|0\rangle}+\omega_{|1\rangle}}{2}$. Under such circumstances, the reflected signal's magnitude for states $|0\rangle$ and $|1\rangle$ is equivalent, thereby encoding the qubit's state information exclusively within the phase φ, as depicted by Figure 6.1. Consequently, the detuning between the qubit and resonator should be tailored to fulfill the criterion for optimal state visibility, $\chi = \frac{\kappa}{2}$, which is particularly advantageous for phase measurements, while also mitigating qubit dephasing effects.

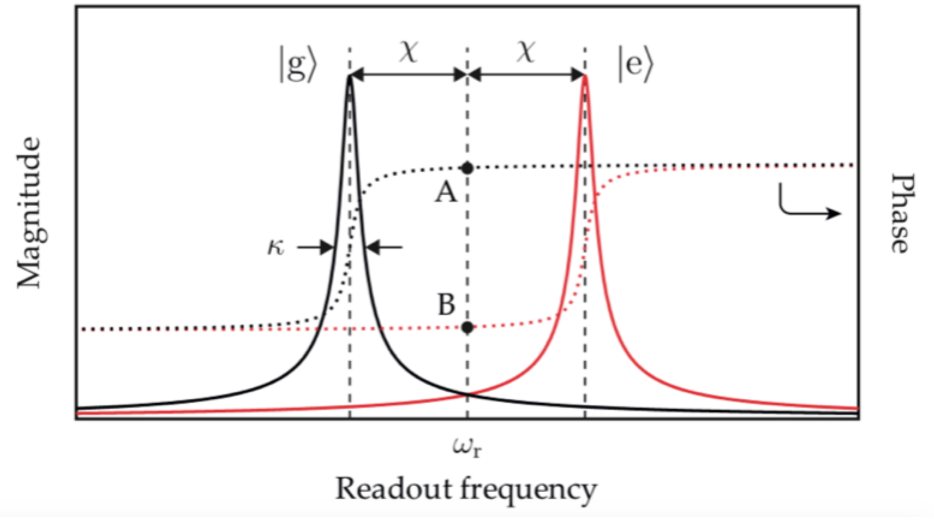

Figure 6.1: This image enables the identification of the ideal point for probing the resonator, denoted as ω_r.

Upon selecting the appropriate frequency, amplitude and duration of the tone used to probe the resonator, we can measure the qubit eigenstate extracting the phase of the reflected classical microwave though a *homodyne* or *heterodyne* demodulation.

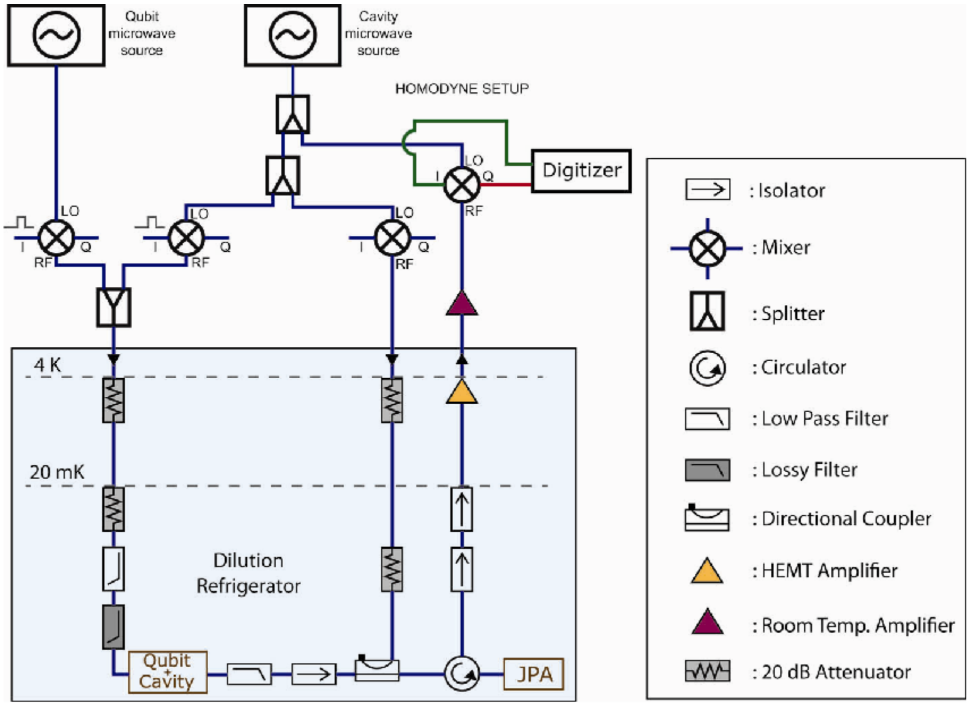

Figure 6.2: The image illustrates the schematic setup of a quantum system, encompassing the measurement chain and all components, from room temperature equipment to cryogenic apparatus.

6.3 Measurement Accuracy

In the realm of quantum measurements, the influence of noise is paramount, impacting the precision with which outcomes can be measured. In an idealized scenario without noise, any measurable shift in the resonator frequency, would enable a clear distinction between the states of a qubit. Realistically, the quantum measurement's result tends to manifest as a Gaussian spread within the (I, Q)-plane, attributable to both classical and quantum noise interferences.

The noise affecting readout signals originates from multiple sources. Inherently associated with the resonator used for interrogation, each mode carries a quantum noise of $\frac{\hbar\omega}{2}$, attributable to *Zero-point energy* that establishes the mode's half-photon ground energy. Additionally, significant noise contributions arise from classical noise leaking through the measurement electronics. The amplifiers employed to boost the reflected signal introduce further noise, adding classical noise and at least $\frac{\hbar\omega}{2}$ quantum noise, in accordance with Heisenberg's uncertainty principle. Moreover, any attenuation of the signal before it reaches the initial amplifier results in additional noise.

Noise induces undesired fluctuations in the probe signal, leading to ambiguity in the demodulated outputs, and thus in the qubit state measurement. In order to be able to perform precise qubit measurement it is fundamental to have probe signals with a high signal-to-noise ratio to minimize the errors in state differentiation to a tolerable threshold that does not degrade the fidelity of the readout.

It is also very important to be able to perform rapid readouts in order complete the process within a temporal span that is notably brief in comparison to the qubit's longitudinal relaxation time, that is:

$$\tau_{ro} \ll T_1 \ . \tag{6.4}$$

While the dispersive readout technique, particularly within the few-photon limit, exerts minimal back-action on the qubit state, prolonged readout intervals increase the probability of qubit T_1 relaxation, which adversely impacts the fidelity of the readout, so achieving high-precision readout demands the execution of single-shot measurements in a timeframe τ_{ro} considerably shorter than the qubit's relaxation time. The measurement fidelity, function of the measurement span, can be modeled through the following equation:

$$F(\tau_{ro}) = e^{-\tau_{ro}/T_1} \ , \tag{6.5}$$

In order to implement accurate readout systems, designer have two strategic approaches: broadening the resonator linewidth to decrease its ring-up duration and minimizing the integration period. Balancing the dual objectives of shielding a quantum system from environmental decoherence while simultaneously conducting rapid state readouts poses a challenging trade-off.

6.4 Josephson Parametric Amplifiers

Despite the reasonable signal-to-noise ratio (SNR) offered by dispersive readout, achieving single-shot readout is non-trivial. The SNR suffers due to thermal noise as the signal transits from the cryogenic environment of the chip to room-temperature electronics. This is attributed to the low number of microwave photons used to measure, and the fact that their energy is significantly lower than room-temperature thermal energy. Thus, amplification prior to detection becomes crucial.

Chaining multiple amplifiers in series isn't a viable solution as the SNR is primarily determined by the first amplifier's noise figure, according to the Friis formula [41]. Therefore, the presence of a very high-quality and low noise, ideally quantum limited, pre-amplification stage is crucial.

The Josephson Parametric Amplifier (JPA) [42, 43] plays a critical role in quantum computing by significantly enhancing the accuracy of quantum measurements. Indeed, as elucidated by Friis formula, the initial stage of amplification plays a pivotal role in the entire amplification chain, establishing the minimum noise figure that will be appended to the amplified signal. Consequently, the presence of a high-quality amplifier in close proximity to the qubit is of fundamental importance. Although this section focuses on JPA, Traveling Wave Parametric Amplifies (TWPA) can also be used to ideally implement quantum limited amplification [44, 45].

Commercially available High-Electron-Mobility Transistor (HEMT) amplifiers, typically installed at the 4K stage of a dilution refrigerator, provide substantial gain but add significant noise photons to the signal. This added noise worsens the SNR. To counteract this, nearly noiseless parametric amplifiers using Josephson junctions have been developed.

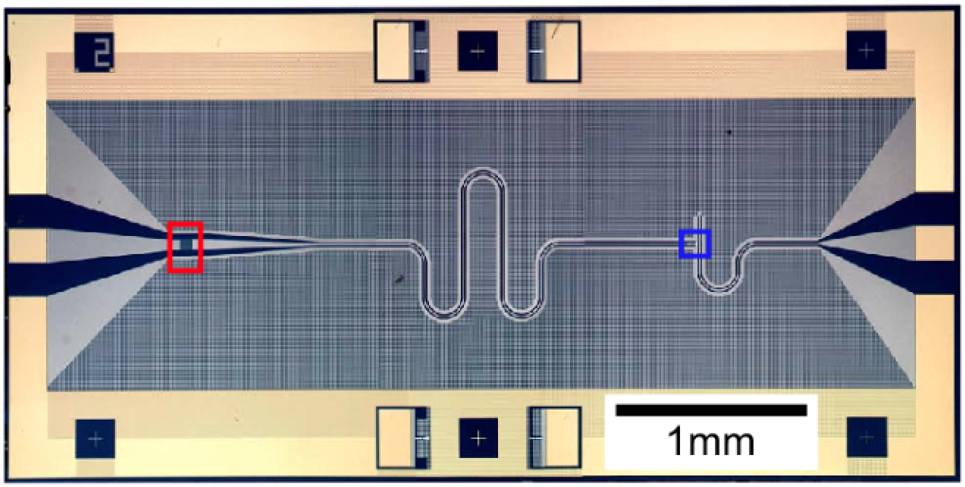

Figure 6.3: The image displays one of the most renowned Josephson Parametric Amplifier (JPA) designs, realized by Y. Nakamura et al.

Parametric amplifiers enhance a weak signal by transferring energy from a strong pump through the frequency-mixing enabled by time-variable reactance modulation. The low noise characteristic of these amplifiers arises from modulating reactance rather than resistance. In superconducting circuits, Josephson junctions are used to create a tunable inductor, leading to the development of the Josephson Parametric Amplifier (JPA).

Parametric amplification, involves the interplay between the signal and the idler, that is, a tone generated as a byproduct of energy conservation, satisfying the equation $\omega_m = \omega_s + \omega_i$, with ω_m representing the modulation frequency, ω_s the signal frequency, and ω_i the idler frequency.

Parametric amplifiers, specifically JPAs, are classified according to two key considerations. The first is the optimization of the energy transfer from the pump to the signal, which can be achieved through a resonant structure enabling multiple reflections within a cavity. The second consideration is the method by which the inductance is modulated. Depending on the technique and operational parameters, the modulation frequency ω_m may equate to the pump frequency ω_p or be double its value.

To present this amplification method, consider the resonator-based JPA depicted in Figure 6.4.

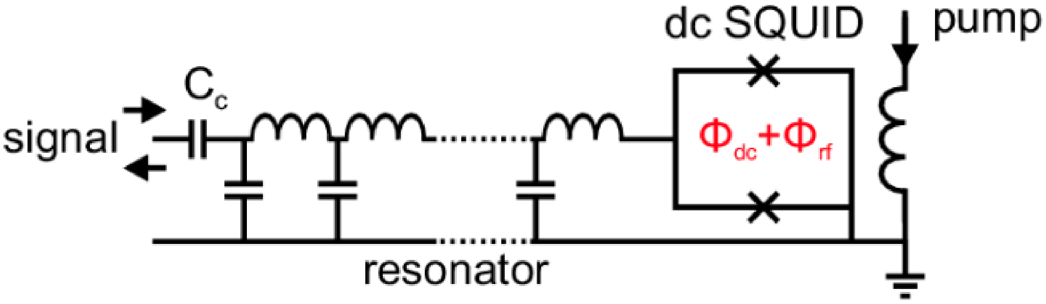

Figure 6.4: The image shows a schematic representation of the Josephson Parametric Amplifier architecture, as realized by Y. Nakamura et al.

This figure showcases a quarter-wavelength ($\lambda/4$) resonator that terminates in a DC-SQUID, which is subject to a flux bias. As discussed in Section 3.5, a DC-SQUID functions as a tunable Josephson junction. Its effective inductance, denoted as $L_{J,\text{eff}}$, is determined by the equation:

$$L_{J,\text{eff}}(\Phi_{\text{ext}}) = \left(\frac{\Phi_0}{2\pi}\right)^2 \frac{1}{2E_J \cos\left(\frac{\Phi_{\text{ext}}}{2}\right)} \ . \tag{6.6}$$

Employing Equation 6.6, we proceed under the premise that $E_{J1} = E_{J2} = E_J$. The DC-SQUID inductance, is modulated via flux bias variation, a process termed flux pumping. For this operation, the external flux Φ_{ext} is dissected into a DC bias Φ_{dc} and a pumping term Φ_{pump}. The amplifier's operational regime hinges on the value of Φ_{dc}.

In fact we can have two type of working regimes, the three-wave mixing and the four-wave mixing. When the DC flux bias Φ_{dc} is zero, the effective inductance $L_{J,\text{eff}}$ demonstrates quadratic dependence on the external flux Φ_{ext}. This occurs because the term $\frac{1}{\cos(x/2)}$ can be approximated by $1 + \frac{x^2}{8}$. Consequently, the modulation frequency ω_m becomes twice the pump frequency ω_p, where ω_p is equal to the resonator frequency ω_r. This phenomenon is identified as the four-wave mixing process, involving for each input photon at the signal frequency ω_s, a photon at the idler frequency ω_i, and two photon at the pump frequency ω_p.

It possible to tune the DC flux bias Φ_{dc} in order to appreciate, a significant contribution from linear terms of $L_{J,\text{eff}}$. In this scenario, the modulation frequency ω_m becomes equal to the pump frequency ω_p. However, in this case in order to have amplification we have to set the pump frequency ω_p to double the resonator frequency ω_r. This process called three-wave mixing, involves for each input photon at the signal frequency ω_s, a photon at the idler frequency ω_i, and one photon at the pump frequency ω_p.

6.5 Case Study: JPA Development at INFN

The development of the Josephson Parametric Amplifier at the Istituto Nazionale di Fisica Nucleare stands as a notable example of innovation in quantum measurement technology.

INFN's effort into the development of JPAs was motivated by the need for ultra-sensitive and low-noise amplifiers in quantum computing and fundamental physics experiments.

During my PhD, I played a direct role in the design of two JPAs. The first was designed with a 5 GHz resonator, and the second with an 8.5 GHz resonator. Both designs involved the coupling of a quarter-wave resonator with internal quality factor in the order of 10^6 to a DC-SQUID device grounded at one end. While the device design might appear straightforward, it is quite the contrary. In such designs, meticulous attention to every detail is crucial for the device's functionality. For these projects, I utilized Qiskit Metal primarily for defining chip layouts and setting up electromagnetic simulations, finding it more user-friendly and efficient than directly using Ansys software for these tasks.

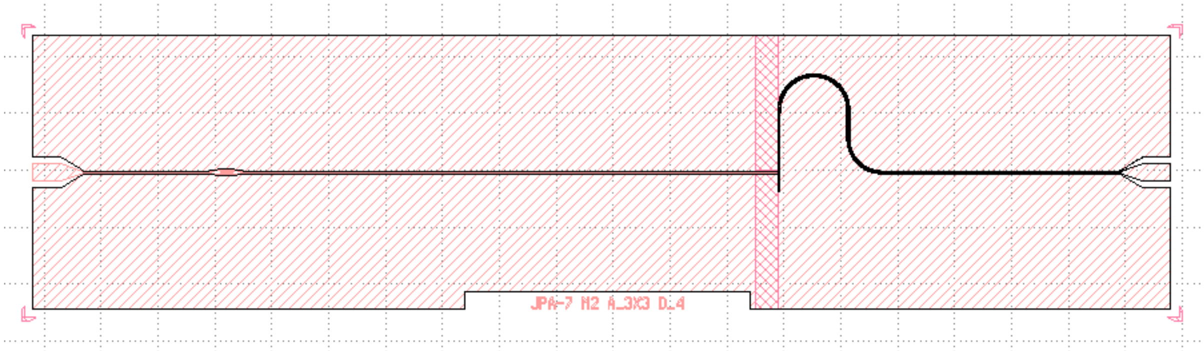

Figure 6.5: The image shows the layout of the JPA I designed. Both 5 and 8.5 GHz JPAs have the same structure; the only difference is the length, and thus, the resonance frequency of the resonator.

Both JPA configurations feature a coupling mechanism to a transmission line, which accommodates the input and the amplified output signals through a capacitance of 20 fF. The JPAs receive both the pump and bias signals via a single flux bias line, which is effectively a 50-ohm matched transmission line. This line is terminated near the DC-SQUID to ground in order to maximize the magnetic flux coupling.

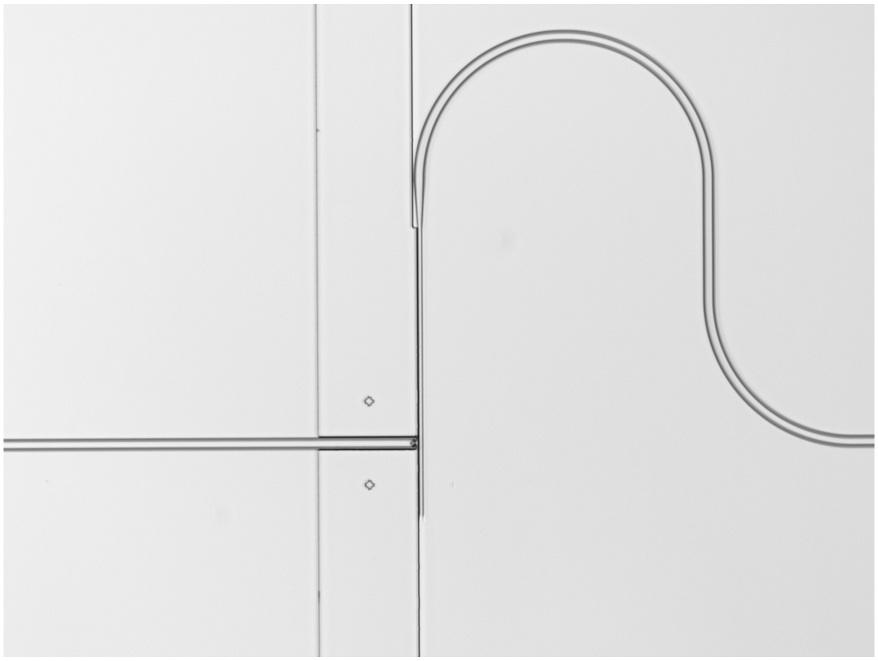

Figure 6.6: The image presents a microscopic view of the flux bias line and the resonator end grounded through the DC-SQUID.

Figure 6.7: The image presents a detailed microscopic view of the flux bias line and the DC-SQUID.

A particularly challenging aspect was the design of the flux bias line. In my design, this line serves a dual purpose: it is driven by both a DC current and an RF current. The DC current establishes the operating point of the JPA, while the RF current delivers the pump tone necessary for transferring energy to the signal being amplified. A significant portion of my time in the design process was dedicated to optimizing the coupling between the flux bias and the DC-SQUID.

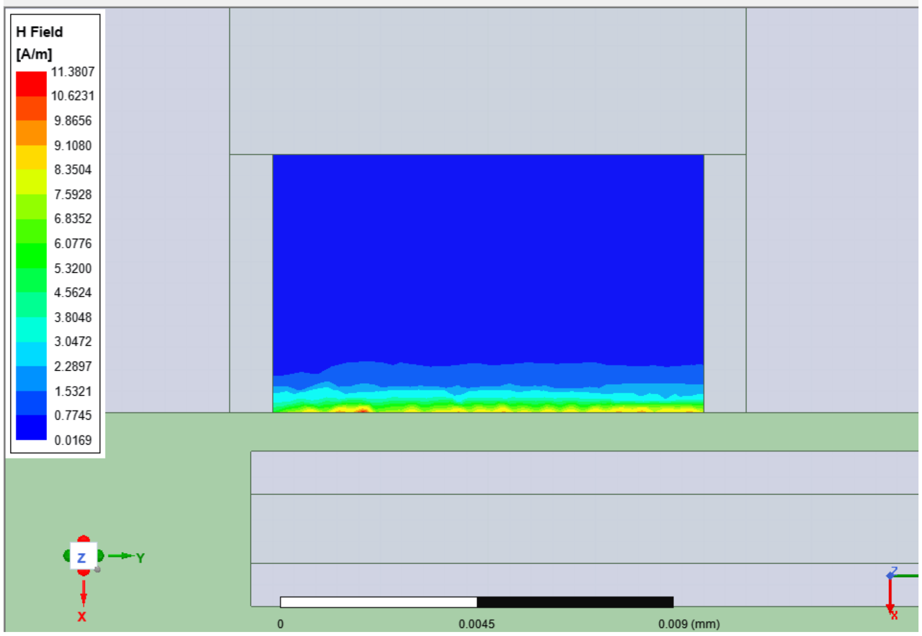

Figure 6.8: Magnetic field simulation in the DC-SQUID of the 5 GHz JPA: This image represents the simulation results with the pump signal power in the flux bias line set to -40 dBm.

Nonetheless, it is pertinent to note that one of the most difficult challenges encountered in the development of the JPA was the fabrication of the Josephson junctions. Crafting these junctions with the requisite properties and specific Josephson inductance values presented a considerable challenge. This difficulty was further compounded by the fact that FBK is in the process of refining its manufacturing techniques for such devices.

In the course of developing these devices, another significant challenge encountered was achieving the desired quality factor for the resonators. This difficulty mirrors the experiences at NIST with the fabrication of Transmon qubits, where ensuring a clean and defect-free fabrication process proved to be a challenging task. The complexity of fabricating resonators with a specific Q-factor underscores the criticality of precision and control in the manufacturing processes of quantum devices.

At the time of writing this thesis, the measurement of the characteristics of the JPA I designed has not been feasible. Unfortunately, the fabrication of these devices required more time than initially anticipated, largely due to the aforementioned fabrication complexities. Additionally, the requirement for characterizing these devices in a cryogenic environment introduces further challenges, significantly complicating the assembly of the necessary experimental setup for their characterization. These factors collectively contributed to the delay in obtaining empirical data on the designed JPA.

Chapter 7

Conclusion

This concluding chapter encapsulates the significant findings of the thesis and my PhD research, reflecting on the implications of these discoveries, and discussing potential avenues for future research in the rapidly evolving field of quantum computing.

7.1 Summary of Findings

This thesis represents a comprehensive journey through the expansive domain of quantum computing. Throughout the duration of my research, I had the fortunate opportunity to delve into various facets of this field, encompassing both theoretical and experimental aspects of hardware design and control. This multifaceted exploration has provided me with a holistic understanding of quantum devices, where insights gained in one area have significantly enhanced my proficiency in others, and vice versa. Such an integrative approach has been instrumental in developing a broad perspective on the complexities and interdependencies within the realm of quantum computing.

The endeavor of designing quantum hardware, with a specific focus on Transmon qubits and JPAs, has proven invaluable in evaluating both the design tools and fabrication processes utilized. Notably, despite encountering fabrication errors, the Transmon qubit to which I significantly contributed in terms of design, exhibited hardware parameters that closely aligned with the simulated predictions. This outcome served as a validation of the scalability of our design tools for constructing more complex quantum devices. Furthermore, it provided insights into which quantum simulations are most effective for predicting device parameters. While this initial success is promising, it is acknowledged that building complete trust in these tools necessitates further testing, as reliance on a single fabrication instance is insufficient. Nevertheless, this represents a solid foundation from which to advance.

My research stay at Chalmers University, primarily dedicated to the control of Transmon qubits, has been pivotal in assessing the efficacy of CRAB-like algorithms in the control of Transmon-based Quantum Processing Units. This subject initially began as a theoretical exploration in the first year of my PhD, culminating in the opportunity to apply these concepts to actual hardware towards the conclusion of my doctoral studies. The results from these applications demonstrated that the algorithm I designed could be effectively utilized for qubit control, achieving and even surpassing the performance of reference gate implementations, while also reducing the control duration. Despite the constraints of my research period, which limited the extent of my exploration into this field, I am confident that there is significant potential for further advancements. I am hopeful that my collaborators will continue to develop and refine the groundwork laid during my research.

7.2 Future Research Directions

The finding I exposed in this thesis work, are a good starting point, but have a lot of room to improve. Regarding the Transom qubit design, it would be beneficial to clearly define the source of error that compromised the device coherence times. This is mandatory in order to proceed to the next step, that is, the design of a two-qubit device. This represents the next logical advancement, laying the groundwork for testing a Universal Set of quantum operations on a hardware device designed by INFN. Although this task has already been achieved by multiple groups, accomplishing it would represent a significant milestone for the Italian research community in this field. It is crucial for narrowing the gap with state-of-the-art research in quantum computing.

In the realm of applying optimal control techniques to Transmon qubit control, the research presented in this thesis opens up several promising avenues. A primary focus could be directed towards further enhancing the precision of the quantum control methodologies developed during my research period at Chalmers University of Technology. Another intriguing prospect is the exploration of optimization techniques that are not dependent on Gaussian envelopes or DRAG-inspired structures. Such exploration could reveal new and potentially more efficient strategies for quantum control. Furthermore, the implementation of randomized benchmarking emerges as a robust method for evaluating the fidelity of quantum gates, thereby deepening our understanding of their performance. Additionally, while the current research has focused on non-gradient methods, exploring gradient-based optimizations could uncover more advanced and efficient optimization techniques.

Personally, I hope that the insights and potential path of exploration presented in this thesis will serve as a foundation for future research in this field. I am deeply appreciative of having had the opportunity to delve into this fascinating topic and collaborate with such exceptional research groups. Their collective expertise and guidance have been invaluable and have greatly enriched my research experience.

7.3 Acknowledgements

As this thesis comes to its conclusion, it is important to acknowledge the invaluable contributions of those who have supported and guided this research journey. Their assistance, insight, and encouragement have been pivotal to the completion of this work.

I dedicate this thesis work to my children, Ella and Joel Corti. Their presence in my life continually motivates me to become a better person, and inspires me to give my best in all endeavors.

I extend my deepest gratitude to my partner, Carolina D'Aquino. Without her support and sacrifices, embarking on this journey would not have been possible. I am also profoundly grateful to my parents, Nicola Corti and Thesere Chiepo Amonkou, my grandparents, Graziella Cellai and Fernando Corti, and to Carolina's parents, Cristina Zarcone and Salvatore D'Aquino, for their immense help and support. They have been instrumental in my life, providing me with the stability and encouragement necessary to focus on my research.

I am immensely grateful to my thesis advisors, Alessandro Cidronali and Leonardo Banchi. Their expertise, understanding, and patience have greatly enriched my knowledge base. I could not have imagined having better mentors for my PhD studies.

I am very thankful to my colleagues Danilo Labranca and Roberto Moretti for their effort and contribution to designing the first QubIT chip. Their expertise and skill have been crucial in its development. I'd also like to thank Claudio Gatti, Andrea Giachero, Federica Mantegazzini, Benno Margesin, and Paolo Falferi for the opportunity to be part of the QubIT project and for sharing their expertise and time with me.

I would like to extend my sincere thanks to Giovanna Tancredi, Liangyu Chen, and all the members of QTL at Chalmers University of Technology. Their assistance, expertise, and welcoming attitude have been fundamental to my personal and professional growth, for which I will always be grateful.

Special thanks are due to Monica Righini, Giovanni Collodi and all my colleagues and peers at the DINFO department of the University of Florence, whose camaraderie, discussions, and shared knowledge have been enriching. I am particularly grateful to Marco Passafiume, for his support, motivation, and for the many stimulating conversations and his invaluable advice.

I also express my appreciation to the staff at the University of Pisa and the University of Florence, especially Enzo Pasquale Scilingo, for their help in navigating the administrative and technical aspects of my research. Their assistance was invaluable in ensuring that my research could progress smoothly and efficiently.

Lastly, I would like to extend my thanks to the broader community of the quantum computing researchers. The conferences, seminars, and workshops I attended were not only informative but also offered opportunities to engage with and learn from leading experts in the field. These experiences have been invaluable to my professional and personal growth.

In closing, while the list of those to thank is extensive, each person has left a lasting impact on my journey, and for that, I am profoundly grateful. This thesis would not have been possible without their collective support and contributions.

Bibliography

[1] H. A. Corti, L. Banchi, A. Cidronali, Robustness of a universal gate set implementation in transmon systems via chopped random basis optimal control, Physics Letters A 438 (2022) 128119.

[2] D. Labranca, H. A. Corti, L. Banchi, A. Cidronali, S. Felicetti, C. Gatti, A. Giachero, A. Nucciotti, First design of a superconducting qubit for the qub-it experiment, Nuclear Instruments and Methods in Physics Research Section A: Accelerators, Spectrometers, Detectors and Associated Equipment 1046 (2023) 167716.

[3] R. Moretti, H. A. Corti, D. Labranca, F. Ahrens, G. Avallone, D. Babusci, L. Banchi, C. Barone, M. M. Beretta, M. Borghesi, et al., Design and simulation of a transmon qubit chip for axion detection, IEEE Transactions on Applied Superconductivity (2024).

[4] R. P. Feynman, Simulating physics with computers, in: Feynman and computation, CRC Press, 2018, pp. 133–153.

[5] M. A. Nielsen, I. L. Chuang, Quantum computation and quantum information, Cambridge university press, 2010.

[6] S. Kwon, A. Tomonaga, G. Lakshmi Bhai, S. J. Devitt, J.-S. Tsai, Gate-based superconducting quantum computing, Journal of Applied Physics 129 (4) (2021) 041102.

[7] P. Krantz, M. Kjaergaard, F. Yan, T. P. Orlando, S. Gustavsson, W. D. Oliver, A quantum engineer's guide to superconducting qubits, Applied physics reviews 6 (2) (2019).

[8] A. P. Place, L. V. Rodgers, P. Mundada, B. M. Smitham, M. Fitzpatrick, Z. Leng, A. Premkumar, J. Bryon, A. Vrajitoarea, S. Sussman, et al., New material platform for superconducting transmon qubits with coherence times exceeding 0.3 milliseconds, Nature communications 12 (1) (2021) 1779.

[9] Z. Chen, J. Kelly, C. Quintana, R. Barends, B. Campbell, Y. Chen, B. Chiaro, A. Dunsworth, A. Fowler, E. Lucero, et al., Measuring and suppressing quantum state leakage in a superconducting qubit, Physical review letters 116 (2) (2016) 020501.

[10] P. Zhao, K. Linghu, Z. Li, P. Xu, R. Wang, G. Xue, Y. Jin, H. Yu, Quantum crosstalk analysis for simultaneous gate operations on superconducting qubits, PRX quantum 3 (2) (2022) 020301.

[11] D. Alesini, C. Braggio, G. Carugno, N. Crescini, D. D'Agostino, D. Di Gioacchino, R. Di Vora, P. Falferi, U. Gambardella, C. Gatti, et al., Search for invisible axion dark matter of mass m a= 43 μ ev with the quax–a γ experiment, Physical Review D 103 (10) (2021) 102004.

[12] B. Johnson, M. Reed, A. A. Houck, D. Schuster, L. S. Bishop, E. Ginossar, J. Gambetta, L. DiCarlo, L. Frunzio, S. Girvin, et al., Quantum non-demolition detection of single microwave photons in a circuit, Nature Physics 6 (9) (2010) 663–667.

[13] D. P. DiVincenzo, The physical implementation of quantum computation, Fortschritte der Physik: Progress of Physics 48 (9-11) (2000) 771–783.

[14] G. Wendin, Quantum information processing with superconducting circuits: a review, Reports on Progress in Physics 80 (10) (2017) 106001.

[15] J. Bardeen, L. N. Cooper, J. R. Schrieffer, Microscopic theory of superconductivity, Physical Review 106 (1) (1957) 162.

[16] M. Göppl, A. Fragner, M. Baur, R. Bianchetti, S. Filipp, J. M. Fink, P. J. Leek, G. Puebla, L. Steffen, A. Wallraff, Coplanar waveguide resonators for circuit quantum electrodynamics, Journal of Applied Physics 104 (11) (2008).

[17] M. Reed, L. DiCarlo, B. Johnson, L. Sun, D. Schuster, L. Frunzio, R. Schoelkopf, High-fidelity readout in circuit quantum electrodynamics using¡? format?¿ the jaynes-cummings nonlinearity, Physical review letters 105 (17) (2010) 173601.

[18] B. D. Josephson, Possible new effects in superconductive tunnelling, Physics letters 1 (7) (1962) 251–253.

[19] F. Arute, K. Arya, R. Babbush, D. Bacon, J. C. Bardin, R. Barends, R. Biswas, S. Boixo, F. G. Brandao, D. A. Buell, et al., Quantum supremacy using a programmable superconducting processor, Nature 574 (7779) (2019) 505–510.

[20] J. Martinis, Design of a superconducting quantum computer, in: CLEO: Science and Innovations, Optica Publishing Group, 2012, pp. JW1I–1.

[21] J. Koch, M. Y. Terri, J. Gambetta, A. A. Houck, D. I. Schuster, J. Majer, A. Blais, M. H. Devoret, S. M. Girvin, R. J. Schoelkopf, Charge-insensitive qubit design derived from the cooper pair box, Physical Review A 76 (4) (2007) 042319.

[22] A. Palacios-Laloy, F. Nguyen, F. Mallet, P. Bertet, D. Vion, D. Esteve, Tunable resonators for quantum circuits, Journal of Low Temperature Physics 151 (2008) 1034–1042.

[23] J. Stehlik, D. Zajac, D. Underwood, T. Phung, J. Blair, S. Carnevale, D. Klaus, G. Keefe, A. Carniol, M. Kumph, et al., Tunable coupling architecture for fixed-frequency transmon superconducting qubits, Physical review letters 127 (8) (2021) 080505.

[24] A. Osman, J. Fernández-Pendás, C. Warren, S. Kosen, M. Scigliuzzo, A. Frisk Kockum, G. Tancredi, A. Fadavi Roudsari, J. Bylander, Mitigation of frequency collisions in superconducting quantum processors, Physical Review Research 5 (4) (2023) 043001.

[25] Qiskit metal, `https://qiskit.org/ecosystem/metal/`.

[26] M. Bal, A. A. Murthy, S. Zhu, F. Crisa, X. You, Z. Huang, T. Roy, J. Lee, D. v. Zanten, R. Pilipenko, et al., Systematic improvements in transmon qubit coherence enabled by niobium surface encapsulation, npj Quantum Information 10 (1) (2024) 43.

[27] A. A. Houck, J. Schreier, B. Johnson, J. Chow, J. Koch, J. Gambetta, D. Schuster, L. Frunzio, M. Devoret, S. Girvin, et al., Controlling the spontaneous emission of a superconducting transmon qubit, Physical review letters 101 (8) (2008) 080502.

[28] Z. K. Minev, Z. Leghtas, S. O. Mundhada, L. Christakis, I. M. Pop, M. H. Devoret, Energy-participation quantization of josephson circuits, npj Quantum Information 7 (1) (2021) 131.

[29] R. Chakrabarti, H. Rabitz, Quantum control landscapes, International Reviews in Physical Chemistry 26 (4) (2007) 671–735.

[30] R.-B. Wu, R. Long, J. Dominy, T.-S. Ho, H. Rabitz, Singularities of quantum control landscapes, Physical Review A 86 (1) (2012) 013405.

[31] Q. Xie, H. Zhong, M. T. Batchelor, C. Lee, The quantum rabi model: solution and dynamics, Journal of Physics A: Mathematical and Theoretical 50 (11) (2017) 113001.

[32] F. Motzoi, J. M. Gambetta, P. Rebentrost, F. K. Wilhelm, Simple pulses for elimination of leakage in weakly nonlinear qubits, Physical review letters 103 (11) (2009) 110501.

[33] C. P. Koch, U. Boscain, T. Calarco, G. Dirr, S. Filipp, S. J. Glaser, R. Kosloff, S. Montangero, T. Schulte-Herbrüggen, D. Sugny, et al., Quantum optimal control in quantum technologies. strategic report on current status, visions and goals for research in europe, EPJ Quantum Technology 9 (1) (2022) 19.

[34] T. Caneva, T. Calarco, S. Montangero, Chopped random-basis quantum optimization, Physical Review A 84 (2) (2011) 022326.

[35] N. Rach, M. M. Müller, T. Calarco, S. Montangero, Dressing the chopped-random-basis optimization: A bandwidth-limited access to the trap-free landscape, Physical Review A 92 (6) (2015) 062343.

[36] J. A. Nelder, R. Mead, A simplex method for function minimization, The computer journal 7 (4) (1965) 308–313.

[37] M. Y. Niu, S. Boixo, V. N. Smelyanskiy, H. Neven, Universal quantum control through deep reinforcement learning, npj Quantum Information 5 (1) (2019) 33.

[38] N. Margolus, L. B. Levitin, The maximum speed of dynamical evolution, Physica D: Nonlinear Phenomena 120 (1-2) (1998) 188–195.

[39] M. Reed, Entanglement and quantum error correction with superconducting qubits, Lulu. com, 2013.

[40] V. B. Braginsky, F. Y. Khalili, Quantum nondemolition measurements: the route from toys to tools, Reviews of Modern Physics 68 (1) (1996) 1.

[41] H. T. Friis, Noise figures of radio receivers, Proceedings of the IRE 32 (7) (1944) 419–422.

[42] T. Yamamoto, K. Inomata, M. Watanabe, K. Matsuba, T. Miyazaki, W. D. Oliver, Y. Nakamura, J. Tsai, Flux-driven josephson parametric amplifier, Applied Physics Letters 93 (4) (2008).

[43] J. Aumentado, Superconducting parametric amplifiers: The state of the art in josephson parametric amplifiers, IEEE Microwave magazine 21 (8) (2020) 45–59.

[44] C. Macklin, K. O'brien, D. Hover, M. Schwartz, V. Bolkhovsky, X. Zhang, W. Oliver, I. Siddiqi, A near–quantum-limited josephson traveling-wave parametric amplifier, Science 350 (6258) (2015) 307–310.

[45] A. Zorin, Flux-driven josephson traveling-wave parametric amplifier, Physical Review Applied 12 (4) (2019) 044051.